SEARCH FOR THE TOP QUARK IN LEPTON PLUS JETS EVENTS AT THE COLLIDER DETECTOR AT FERMILAB

A Thesis

Submitted to the Faculty

of

Purdue University

by

James Ian Tonnison

In Partial Fulfillment of the

Requirements for the Degree

of

Doctor of Philosophy

August 1994

ACKNOWLEDGMENTS

I would like to thank first and foremost my advisor, Virgil Barnes, for giving me the opportunity to work at CDF. His advise and support were invaluable during my graduate career. I wish to thank Bob Wagner, Morris Binkley, Aseet Mukherjee, J.C. Yun and others in the VTX group for their help and assistance during my first years at CDF. I am also grateful to my CDF colleagues, especially those in the Top group, for the suggestions and comments they provided for this analysis.

Finally, I want to thank my parents, James and Jessie. Without their guidance I would not be where I am today. This thesis is dedicated to them.

TABLE OF CONTENTS

LIST OF FIGURES

Figure Page

Figure Page

LIST OF TABLES

ABSTRACT

Tonnison, James Ian. Ph.D, Purdue University, August 1994. Search for the Top Quark in Lepton Plus Jets Events at the Collider Detector at Fermilab.
Major Professor: Virgil E. Barnes.

A search for the Standard Model top quark in the lepton plus jets channel in $p\bar{p}$ collisions at $\sqrt{s} = 1800$ GeV is described. The analysis was carried out on 19.3 pb^{-1} of data collected with the Collider Detector at Fermilab in the 1992–1993 run. Events were selected by requiring a high P_T electron or muon, missing transverse energy, three or more jets, and a large global sum of transverse energy. To further reduce background processes in the final event sample, at least one non-isolated lepton was required to act as a tag for the b-quarks.

The expected background rate in this analysis is 1.80 ± 0.17 events. 7 events survive all the cuts. The probability for the expected background fluctuating to ≥ 7 events is 0.29% or 2.76σ.

1. INTRODUCTION

The Standard Model (SM) of electroweak interactions has been wonderfully successful in predicting physics in the energy scales produced by the highest present day accelerators, and is in complete agreement with experimental data. Since the discovery of the τ neutrino, and later the bottom quark, there has been strong theoretical and experimental evidence that a bottom must have a top.

From March 1992 to June 1993 the Collider Detector at Fermilab collected 19.3 ± 0.7 pb^{-1} worth of data at a center of mass energy of 1.8 TeV [1]. This high luminosity and energy permitted searches for $t\bar{t}$ pair production with top masses up to ~ 180 GeV/c^2. In this thesis, the search for $t\bar{t}$ pairs was carried out in the lepton plus jets channel where one top quark decays into a b-jet a high P_T lepton and neutrino, and the other top decays into a b-jet and two high Pt jets. This thesis is organized as follows:

Chapter 1 deals with the evidence for and the limits on the mass to the top-quark. The QCD production mechanism, and decay signatures in $p\bar{p}$ colliders are examined.

Chapter 2 gives a detailed description of the Tevatron and the CDF detector systems used in this analysis.

Chapter 3 describes the high P_T inclusive electron and muon data sets. The variables used for cutting on these events and their efficiencies will be given. Also described is the calculation of the missing transverse energy and jet energy and some subsequent modifications made to the raw values.

Chapter 4 is a summation of the Monte Carlo event samples and how they were generated. The MC data samples are used to provide a better understanding of the top signal and background processes, as well as to provide an estimate of the number of signal and background events expected in 19.3 pb^{-1}. Additional jet and missing transverse energy corrections will be described.

Chapter 5 presents the soft lepton tagging (SLT) algorithms used to tag additional leptons in $t\bar{t}$ events. The cuts used to select these soft leptons are given, as well as the efficiencies and fake rates for the various tagging algorithms.

Chapter 6 establishes the kinematical cuts used to select events consistent with $t\bar{t}$ decays. The kinematic variables will be explained, and cut values given.

Chapter 7 calculates the expected number of events in 19.3 pb^{-1} from various background processes (W+jets, di-boson, Drell–Yan, $b\bar{b}$ and QCD, $Z \rightarrow \tau\tau$, and $W + c$), and from $t\bar{t}$.

Chapter 8 reviews the cuts used to tag $t\bar{t}$ events, and the results of applying these cuts to the data. The probability for the expected background fluctuating to that seen in the data is calculated.

Chapter 9 is a summary and conclusion to this analysis. A discussion and interpretation of the results is made.

1.1 Why a Top Quark?

Current experimental data strongly supports the existence of the top quark. Two of the following arguments—forward–backward asymmetries in $e^+e^- \rightarrow b\bar{b}$, and b-quark decays—provide compelling evidence that the top quark exists.

1.1.1 Forward–Backward Asymmetries in $e^+e^- \rightarrow b\bar{b}$

The reaction $e^+e^- \rightarrow b\bar{b}$ proceeds via the two diagrams shown in Figure 1.1. The angular distribution of the individual channels is symmetric about 90°. However,

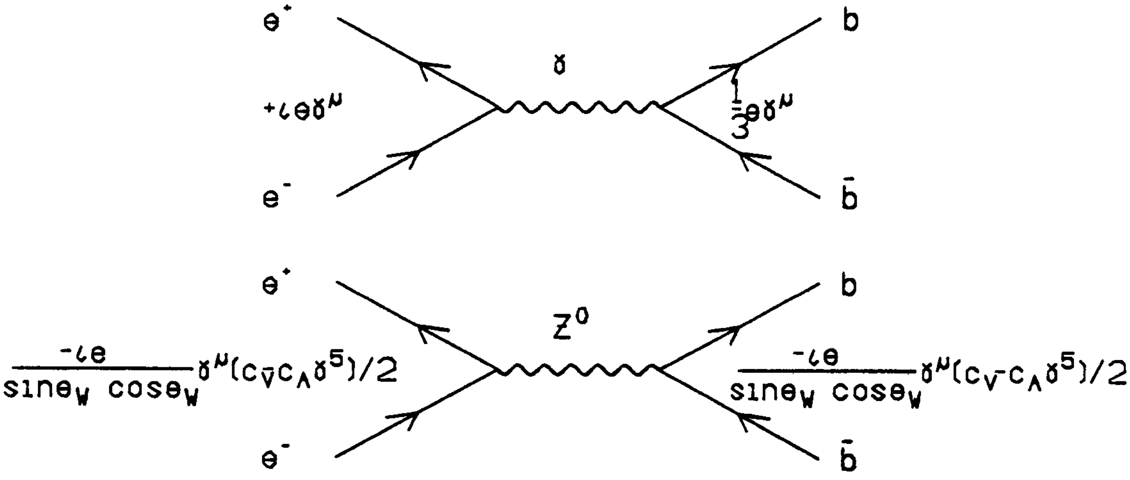

Figure 1.1

Feynman diagrams for the process $e^+e^- \rightarrow b\bar{b}$. Vertex factors included.

when both channels are present, an asymmetry results from the axial-vector coupling of the b-quark to the Z^0 and the vector coupling of the b-quark to both the Z^0 and the γ. The forward–backward asymmetry in $e^+e^- \rightarrow b\bar{b}$ is defined as:

$$A_{FB} = (N_b^F - N_b^B)/(N_b^F + N_b^B), \tag{1.1}$$

where N_b^F is the number of b-quarks produced in the forward (electron) direction, and N_b^B is the number of b-quarks produced in the backward (positron) direction. The most accurate measurement of A_{FB} is $(-22.8\pm2.5)\%$ [2]. This fixes c_A^b in figure 1.1 at $-0.57 \pm 0.15 \pm 0.09$. If the b-quark is a member of a $SU(2)$ doublet, the SM predicts $c_A^b = -\frac{1}{2}$, if b is a singlet then $c_A^b = 0$. This quite nicely shows that the b-quark is a member of a doublet, and its partner is defined to be the top quark.

1.1.2 Absence of FCNC Decays of the b-Quark

It is an experimental fact that the b-quark decays. If the b were a singlet then it

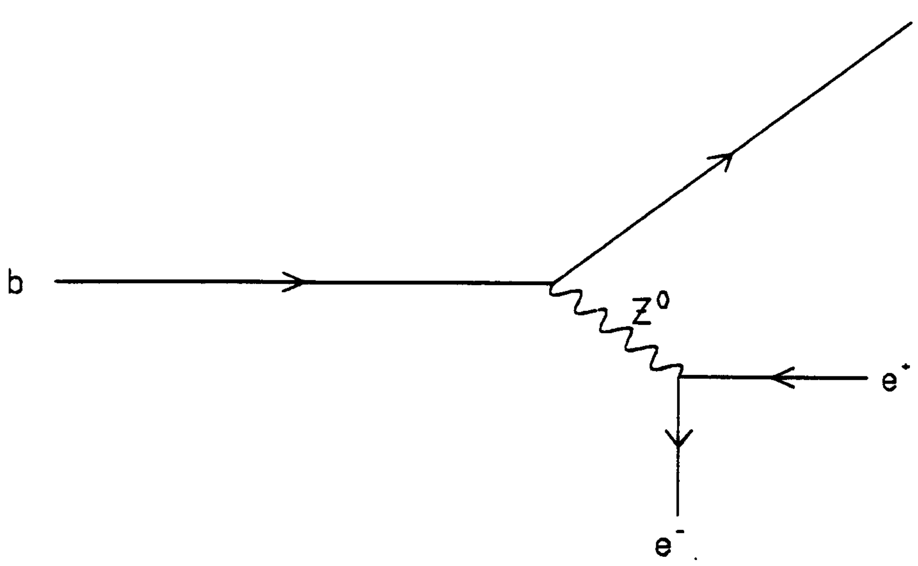

Figure 1.2

An example of a hypothetical *b*–*s* mixing event.

would not couple to the W. (In the SM Lagrangian the W does not couple to $SU(2)$ singlets.) Also, the b cannot decay into lighter quarks via the Z^0 due to the GIM mechanism. The only decay route left is through flavor changing neutral currents (FCNC). Shown in Figure 1.2 is an example of a *b*–*s* mixing event.

These types of events have not been detected. If the *b*-quark is a singlet then the ratio $\Gamma(b \rightarrow l^+l^-X)/\Gamma(b \rightarrow l^-\nu X) \approx 0.11$ should be observed, it is not. The unusual l^+l^- pairs from Υ decays have not been seen proving the *b*-quark is not a singlet.

1.1.3 $B^0\overline{B^0}$ Mixing

The B^0 meson can transform itself into its own anti-particle, $\overline{B^0}$, and vise versa. One quark in the B^0 meson is a *b*-quark while the other can be either be a *d* or *s* quark. Before decaying, the B meson can undergo mixing via the 'box diagrams' shown in

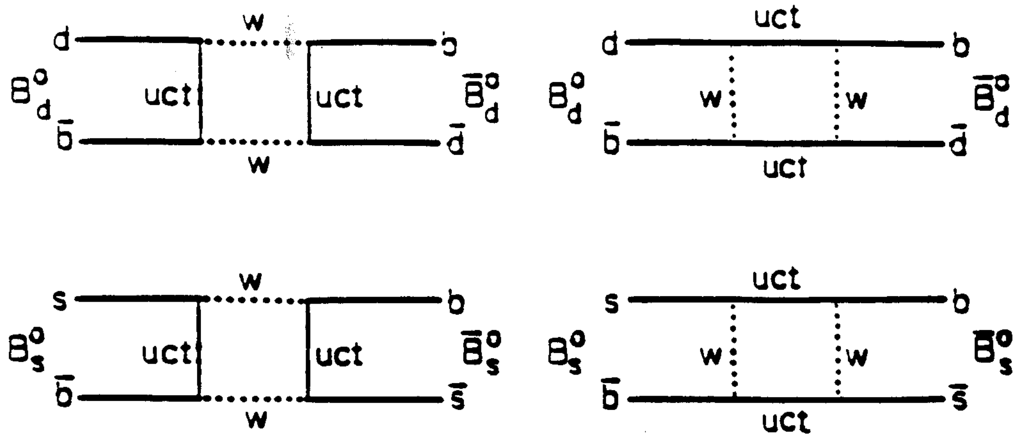

Figure 1.3

Box diagrams for B^0–$\overline{B^0}$ mixing.

Figure 1.3. $B^0\overline{B^0}$ pairs have been produced at ARGUS and CLEO. $B^0\overline{B^0}$ mixing can be detected by searching for an excess of like sign leptons from the semileptonic decays of B^0B^0 and $\overline{B^0B^0}$.

The ratio $r = [N(B^0B^0) + N(\overline{B^0B^0})]/N(B^0\overline{B^0})$ has an explicit m_t^2 dependence. Recent measurements of this ratio provide a lower limit of $m_t > 50$ GeV/c^2 [3].

1.1.4 Top Quark Mass Constraints

The standard electroweak theory is described by a small set of quantities: α, G_F, $m_{f\neq t}$, m_Z, m_t, m_H. (In non-minimal extensions of the SM there is more than one Higgs particle, but this will not be considered here.) Such things as m_W and $\sin\theta_W$ can be derived from these quantities and vise versa. The inclusion of m_t allows one to set limits on the top mass using the other variables. As the first example, m_W can

be inferred from

$$\left(1-\frac{m_W^2}{m_Z^2}(1-\Delta)\right)\frac{m_W^2}{m_Z^2}=\frac{\pi\alpha(m_Z)}{\sqrt{2}G_F m_Z^2}, \tag{1.2}$$

where $\alpha(M_Z)=\frac{1}{129.8\pm0.1}$ and $\Delta=\frac{3G_F m_t^2}{8\pi^2\sqrt{2}}$. Using the ratio $\frac{m_W}{m_Z}$, m_t can be inferred to be 150± 50 GeV/c^2 [4]. The Higgs does have some contribution to the top mass, but enters as a logarithmic term so its effects are minimized. A plot of m_t as a function of m_W and m_H is displayed in Figure 1.4 [5].

There are several other calculated electroweak radiative corrections in addition to the one given in the previous equation. Feynman diagrams for some of these radiative corrections are shown in Figure 1.5. A global fit of precision electroweak measurements to these radiative corrections yields a favored mass of $m_t = 174^{+11+17}_{-12-19}$ GeV/c^2 [6]. In addition to the above SM favored mass, measurements of the W and Z widths require $m_t > 62$ GeV/c^2 at the 95% CL. This lower mass limit is independent of the decay mode of the top quark [7].

1.2 Top Quark Production

In the QCD parton model, the cross section of two hadrons colliding to form a pair of heavy quarks $A+B\rightarrow Q+\overline{Q}+X$ is given by:

$$\sigma(s)=\sum_{ij}\int dx_1 dx_2\hat{\sigma}_{ij}(x_1,x_2,s,m^2,\mu^2)F_i^A(x_1,\mu)F_j^B(x_2,\mu), \tag{1.3}$$

where the structure functions F_i^A are the probabilities of finding a parton i in hadron A with momentum fraction between x_1 and x_1+dx_1, m is the heavy quark mass, $\sqrt{s}$ is the center of mass energy, μ is an arbitrary renormalization scale related to the energy scale of the interaction, and $\hat{\sigma}_{ij}$ are the partonic cross sections for the process $ij\rightarrow Q\overline{Q}X$.

The structure functions give the probability of finding a quark carrying momentum fraction x. Using the assumption that the proton consists of three quarks, one might naively guess that each quark carries $\frac{1}{3}$ of the momentum $(f(x) \sim \delta(\frac{1}{3} - x))$. However, the proton is more complicated than this. The gluons carry about 50% of the total momentum of the proton. In addition to the three "valence" quarks, there is a "sea" of quark-antiquark pairs radiated from the valence quarks. These sea quarks become important in deep inelastic scattering where $x \ll 1$. Here these heavy quarks can be scattered out of the sea in flavor-excitation processes. Structure functions are not accurately predicted by theory, so they must pieced together from data. The determination of these functions for gluons and various sea and valence quarks is crucial in calculating expected heavy quark production cross sections. Figures 1.6 [8] and 1.7 [8] show the fraction of momentum carried for various quarks and gluons in a proton for different values of x and Q^2 (-invariant momentum transfer squared). The light quark structure functions are determined from deep inelastic scattering experiments where $x > 0.01$ and $\mu < 15$ GeV/c^2. The gluon distributions are not measured directly since the gluon does not couple to electroweak probes. As a result, these are less well measured. Luckily at higher top masses the contribution from gluon fusion decreases as shown in Figure 1.8 [9].

The partonic cross sections, $\hat{\sigma}_{ij}$, are computed from QCD. To lowest order, α_s^2, the processes responsible for $Q\overline{Q}$ production are gluon–gluon fusion and quark–antiquark annihilation. The Feynman diagrams for these processes are shown in Figures 1.9 [10]. Next to leading order (α_s^3) processes such as gluon splitting and flavor excitation (Figure 1.10 [10]) enhance $Q\overline{Q}$ production and are also included in the cross section. Splitting $(g \rightarrow Q\overline{Q})$ only occurs a small fraction of the time, however, the large cross section of $gg \rightarrow gg$ can be competitive with α_s^2 processes. The evolution scale of the interaction, μ, is on the order of the top quark mass.

Figure 1.11 [11] shows the expected top quark production cross section to α_s^3. The band in this plot is mainly due to uncertainties in the structure functions, renormalization scale, and to a lesser extent, higher order contributions. Table 1.1 lists various top masses and their cross sections and uncertainties.

1.3 Top Quark Decay

After the heavy quark is produced it "fragments" or "hadronizes" into a hadron containing the heavy quark and hadrons containing lighter flavor quarks. A heavy quark and a lighter quark will most likely combine to form a meson, H_Q, if they have about the same velocity. If no such light quarks are present, the heavy quark will use a small fraction of its energy to pull matching velocity $q\bar{q}$ pairs out of the vacuum. The heavy quark must "dress" itself as a hadron since all particles must be color-neutral. As the hadron H_Q leaves the interaction region it will carry some fraction, $z = P_H/P_Q$, of the original heavy quark's momentum. A phenomelogical model based on experiment (Peterson parameterization) that describes the probability that hadron H_Q carries away momentum fraction z is given by [12]:

$$D_Q^H = \frac{N}{z\left[1 - \frac{1}{z} - \frac{\epsilon_Q}{1-z}\right]^2}, \tag{1.4}$$

where N is the normalization constant ($\int_0^1 D_Q^H(z)dz = 1$), and ϵ_Q is proportional to $1/M_Q^2$. The Peterson parameterization adequately describes existing b and c quark data as can be seen in Figure 1.12 [13]. Figure 1.13 [14] shows D_Q^H with a top of mass 40 GeV/c^2. As m_Q increases, D_Q^H approaches a δ-function centered at $z = 1$.

It is interesting to note that if the top quark is heavy enough no hadron containing a top quark will be produced because the top will decay too quickly. If $m_t > m_W + m_b$ then the top will decay into a b and a real W (decay into a light charged Higgs is not considered here). Since $m_t \gg m_b$, the partial width of the top decay is:

$$\Gamma = \frac{G_F M_Q^3}{8\pi\sqrt{2}}|V_{Qq}|^2\left(1 - \frac{m_W^2}{m_Q^2}\right)^2\left(1 + \frac{2m_W^2}{m_Q^2}\right). \tag{1.5}$$

This is much larger than the width of $t \rightarrow W^*b$, where W^* is an off shell W. (Quarks decaying via virtual W's have $\Gamma \propto G_F^2 m_Q^5$.) Figure 1.14 [15] shows Γ as a function of m_Q. If the top is sufficiently heavy ($m_t > 150$ GeV/c^2), its lifetime ($\tau = \hbar/\Gamma$) will be less than 10^{-24} s or $c\tau \approx 1$ fermi. The color force between quarks "turns on" at a distance of about 1 fermi. At distances less than this, the quark can be considered to be "asymptotically free", and no new quarks need be created to cancel the color charge.

Keeping to SM top decays, the top will decay in the following modes: $t \rightarrow W + b$, $t \rightarrow W + s$, and $t \rightarrow W + u$. However, approximately 99.75% will be in the b-quark mode since the mixing matrix favors decays to the higher mass b than the lighter s or u. With $m_t > 91$ GeV/c^2 [16], the W will be real and on shell, so the decay modes will be $t \rightarrow W + b$ where the W decays into the three lepton doublets ($e\nu_e$, $\mu\nu_\nu$, and $\tau\nu_\tau$) and the $2N_c$ light quark doublets (ud, cs). N_c is the number of colors, which is three. Table 1.2 lists the SM decay modes of $t\bar{t}$ pairs and their branching fractions.

A bonus of heavy quark production is lepton isolation. In the three body decay $t \rightarrow bW$, $W \rightarrow l\bar{\nu}_l$, the angle between the lepton and b must satisfy

$$\sin\theta_{lb} < \frac{m_t^2 - m_b^2}{2P_l m_b}. \tag{1.6}$$

For a large m_t the resulting lepton can be well removed from the b-quark jet. Jet-lepton isolation is a powerful filter used to distinguish $t\bar{t}$ decays from that of lighter quark pair decay ($b\bar{b}$, $c\bar{c}$). The leptons from lighter quarks are not as isolated as can be seen by adjusting the subscripts in equation 1.6.

1.4 $t\bar{t} \rightarrow$ Lepton+Jets Signature at CDF

$t\bar{t}$ pairs decay in one of ten channels as shown in Table 1.2. These channels can be divided into three decay modes: dilepton, l^+l^-+ 2 jets + $\not{E}_T$ ($\not{E}_T$ is shorthand for missing transverse energy); lepton+jets, l + $\not{E}_T$ + 4 jets; hadronic, 6 jets. Each mode has its advantages and shortcomings in a $t\bar{t}$ search. In the dilepton mode, the background is limited to WW, $Z^0 \rightarrow \tau\tau$ + jets, and $c\bar{c}$ and $b\bar{b}$ pairs. After appropriate cuts, these backgrounds can be greatly reduced, leaving mostly signal. However the disadvantage of this mode is that the branching ratio is only a few percent of an already small signal, and requires lots of integrated luminosity to produce enough signal events. The all hadronic mode's most pleasing attribute is that 44% of $t\bar{t}$ pairs decay in this fashion, but the QCD background is so severe it is almost impossible to detect $t\bar{t}$ production using this channel. The remaining mode is the lepton + jets mode, which is the channel this thesis will focus on. This mode has about one third the total branching ratio without the massive background associated with the all hadronic mode. The background rate in this channel is on the order of the signal and is mostly due to W boson production accompanied by jets, $c\bar{c}$ and $b\bar{b}$ pairs, and some minor background from Z^0+ jets and QCD.

Searching for the top the lepton + jets mode dictates the use of several topological cuts. Since one of the tops will decay leptonically, it will produce a lepton, a neutrino, and a b-jet. Owing to the high mass of the top, the lepton and neutrino will have a rather hard P_T spectrum with the lepton being isolated from the b-jet (Equation 1.6). So, selecting events with isolated electrons or muons with $P_T > 20$ GeV/c and $\not{E}_T >$ 20 GeV is the first step. Unfortunately most of the signal from $t\bar{t} \rightarrow \tau + \not{E}_T$ + jets will be lost after applying the $P_T > 20$ GeV/c cut since the τ only decays to $e\nu_e\nu_\tau$ or $\mu\nu_\mu\nu_\tau$ 35% of the time. The two neutrinos from the decay of the τ rob most of the momentum from the τ, resulting in the subsequent e or μ failing the P_T cut.

In principle four jets will be produced in the final state: one b-jet from the top decaying leptonically, and a b-jet plus two other jets from the other top decaying hadronically. However, due to detector effects, jet E_T and η cuts, gluon radiation, etc., the number of observed final state jets can vary in one extreme from zero to eight or more in the other. Luckily, most of the events are produced with three or more observed jets in the central and plug calorimeters with $E_T > 25$ GeV. Therefore, the jet cuts should be made to take advantage of these features.

The above cuts, as will be discussed later in this thesis, select out roughly one fifth of the $t\bar{t} \rightarrow (e, \mu)$ + jets events while greatly reducing the background rate. To reduce the background even more, a b-tag will be made by tagging low P_T electrons and muons from b-quark decays.

Table 1.1

Cross section for $t\bar{t}$ pair production.

M_t	$\sigma(\bar{p}p \rightarrow \bar{t}t + X)$ (pb)		
(GeV)	σ	+error	-error
100	**102**	**+39.0**	**-15.7**
110	**61.6**	**+18.8**	**-8.9**
120	**38.9**	**+10.8**	**-5.2**
130	**25.4**	**+6.2**	**-3.1**
140	**16.9**	**+3.6**	**-1.8**
150	**11.7**	**+2.1**	**-1.2**
160	**8.26**	**+1.37**	**-0.75**
170	**5.83**	**+0.85**	**-0.51**
180	**4.21**	**+0.57**	**-0.35**

Table 1.2

Standard Model decay modes of $t\bar{t}$ pairs. The symbol q denotes a light quark: u, d, s or c.

Decay Mode	Branching Ratio
$t\bar{t} \rightarrow q\bar{q}b\; q\bar{q}\bar{b}$	36/81
$t\bar{t} \rightarrow q\bar{q}b\; e\nu_e\bar{b}$	12/81
$t\bar{t} \rightarrow q\bar{q}b\; \mu\nu_\mu\bar{b}$	12/81
$t\bar{t} \rightarrow q\bar{q}b\; \tau\nu_\tau\bar{b}$	12/81
$t\bar{t} \rightarrow e\nu_e b\; \mu\nu_\mu\bar{b}$	2/81
$t\bar{t} \rightarrow e\nu_e b\; \tau\nu_\tau\bar{b}$	2/81
$t\bar{t} \rightarrow \mu\nu_\mu b\; \tau\nu_\tau\bar{b}$	2/81
$t\bar{t} \rightarrow e\nu_e b\; e\nu_e\bar{b}$	1/81
$t\bar{t} \rightarrow \mu\nu_\mu b\; \mu\nu_\mu\bar{b}$	1/81
$t\bar{t} \rightarrow \tau\nu_\tau b\; \tau\nu_\tau\bar{b}$	1/81

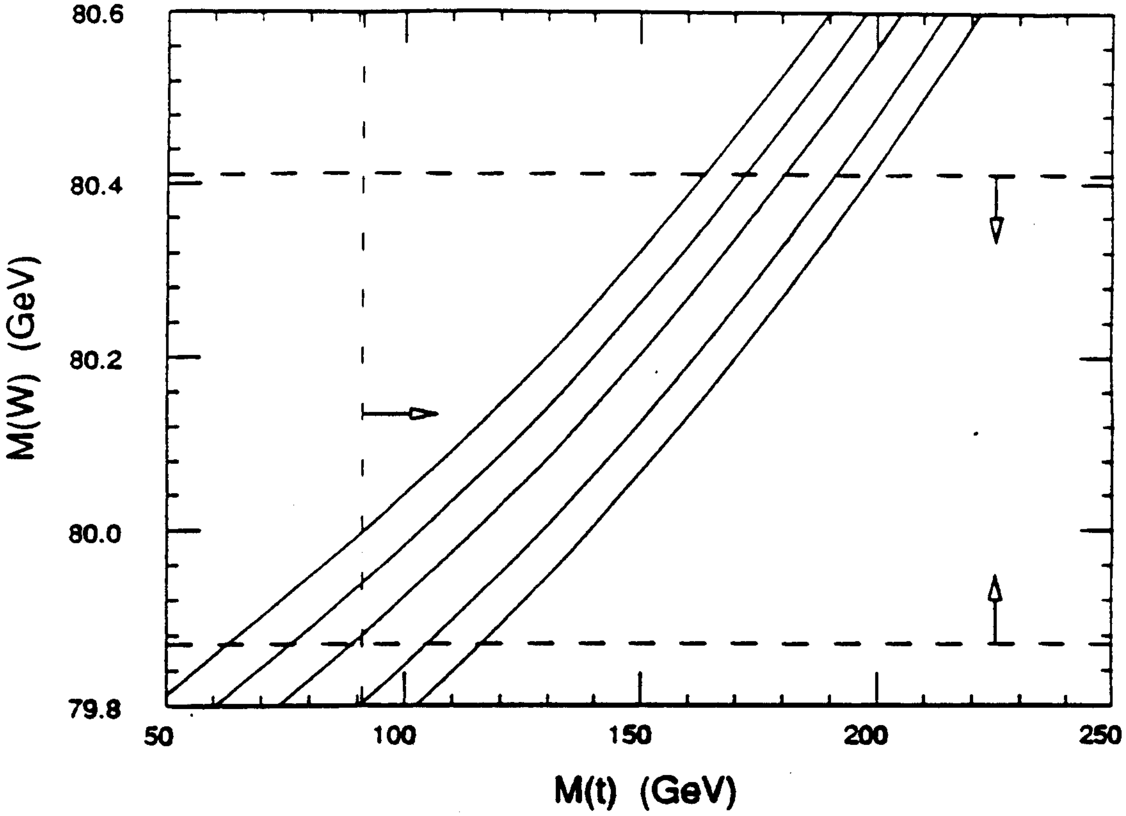

Figure 1.4

Top mass as a function of m_W and m_H. The families of curves are predicted in standard electroweak theory with one Higgs doublet for the dependence of m_W on m_t. From left to right the curves correspond to m_H = 50, 100, 200, 500, and 1000 GeV. The vertical dashed line corresponds to the 95% CL lower limit on the top quark mass, while the horizontal dashed lines correspond to 1σ on m_W.

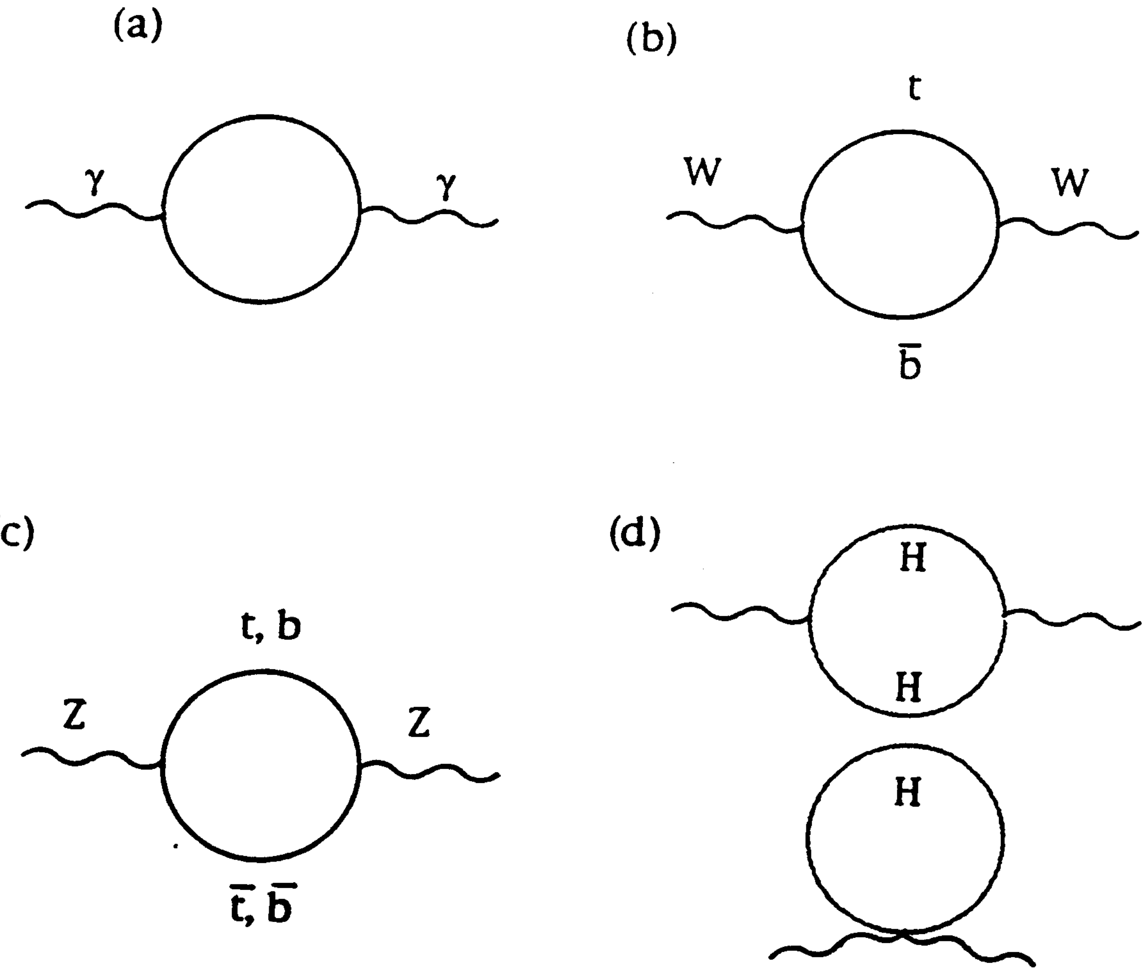

Figure 1.5

Vacuum polarization for gauge bosons. (a) Photon vacuum polarization; (b) W producing a $t\bar{b}$ pair; (c) Z producing $t\bar{t}$ and $b\bar{b}$ pairs; (d) W and Z involving Higgs bosons.

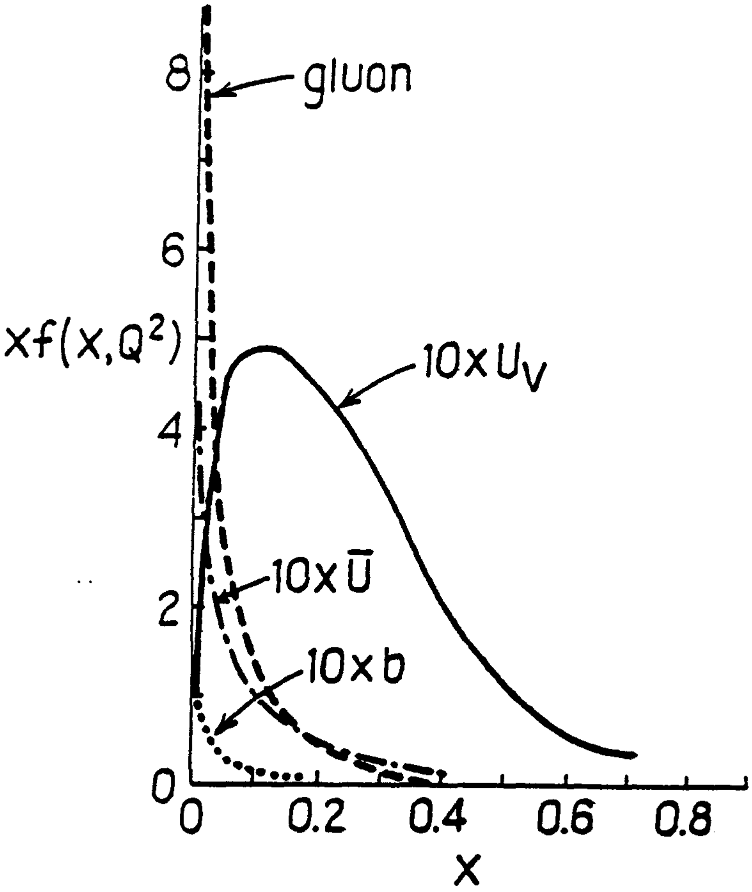

Figure 1.6

Structure function dependence on x and Q^2 at $Q^2 = -q^2 = 10^4$ GeV^2.

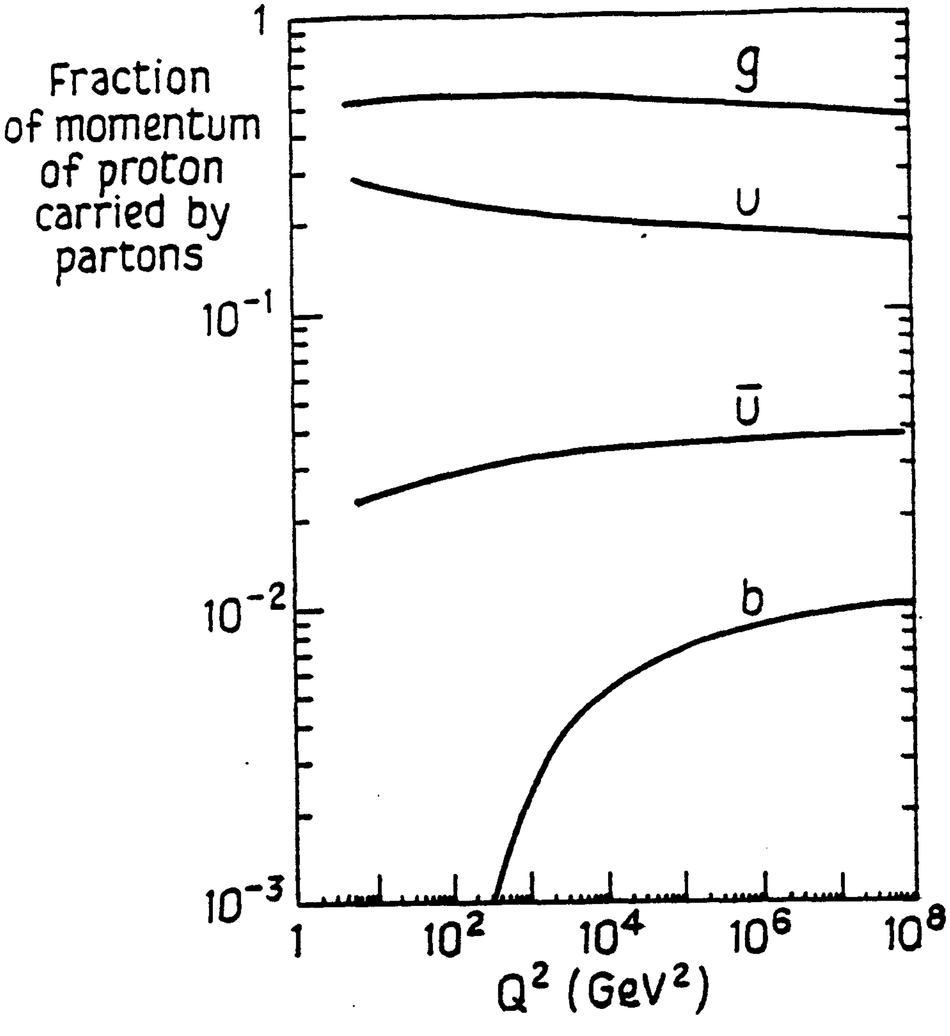

Figure 1.7

Momentum fraction carried by various partons in a proton. The momentum fraction is shown as a function of $Q^2 = -q^2$, integrated over x.

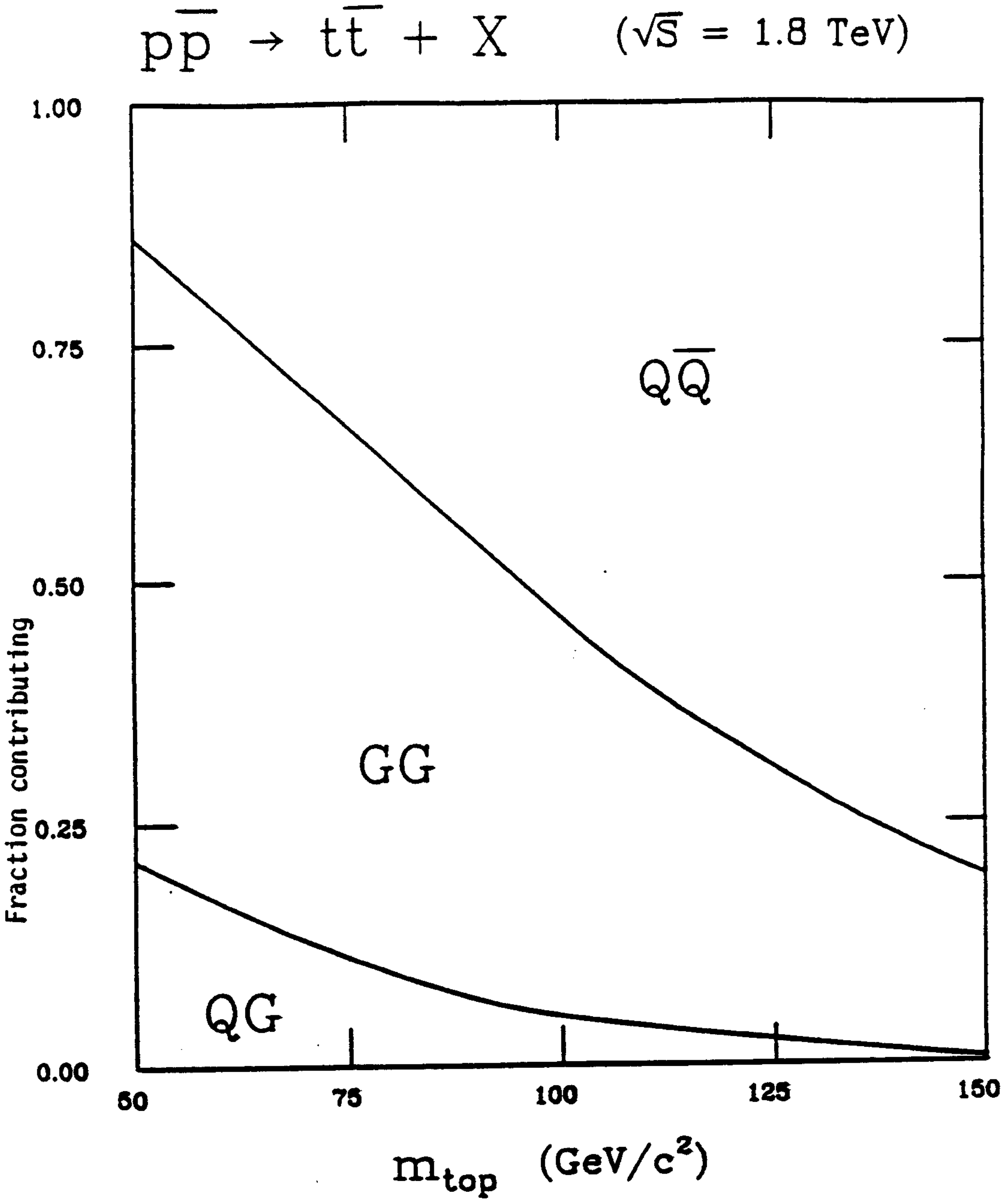

Figure 1.8

Subprocess contributions to $t\bar{t}$ production.

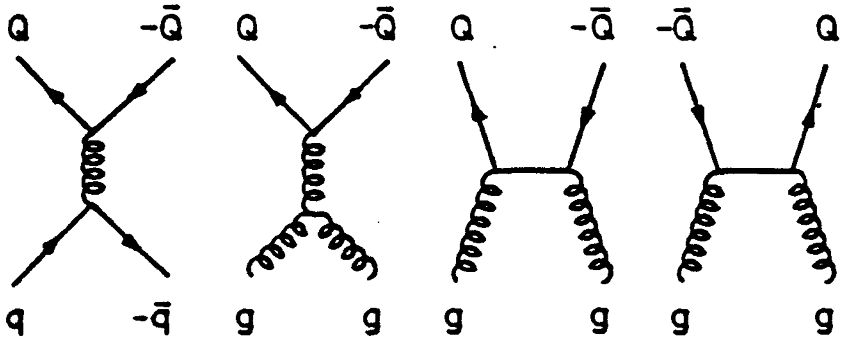

Figure 1.9

Lowest order Feynman diagrams for heavy quark production.

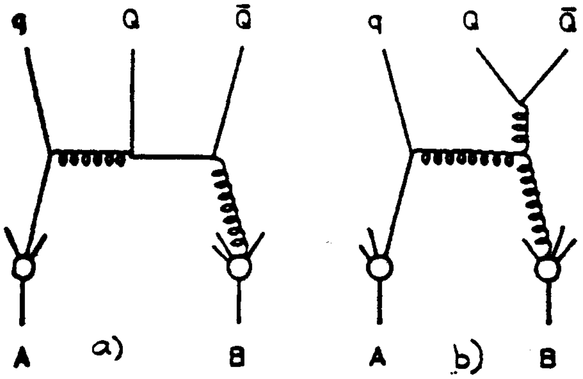

Figure 1.10

Examples of 2 → 3 parton processes producing $Q\overline{Q}$ heavy quark pairs. Two production mechanisms are shown: (a) flavor excitation of the sea, (b) gluon fragmentation.

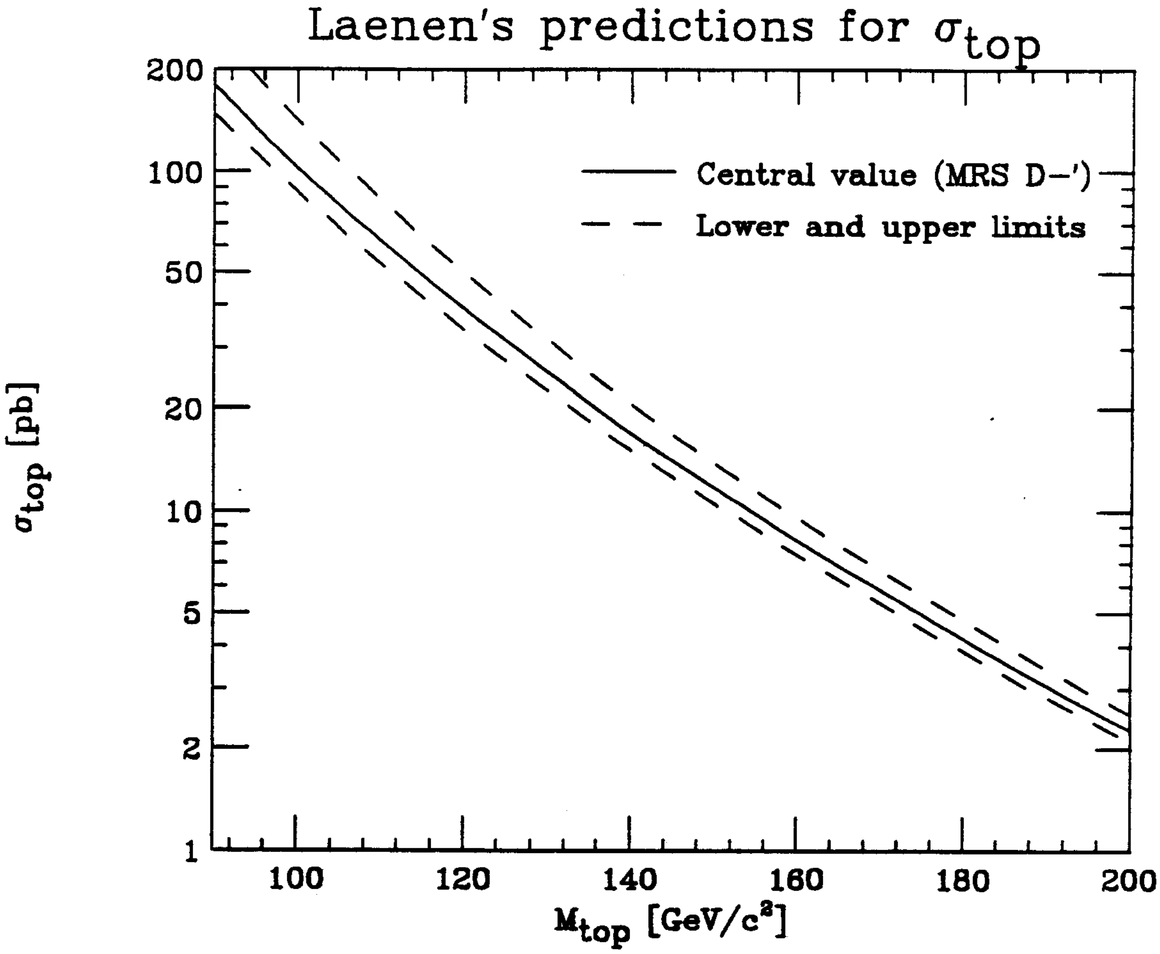

Figure 1.11

NLO $t\bar{t}$ cross section.

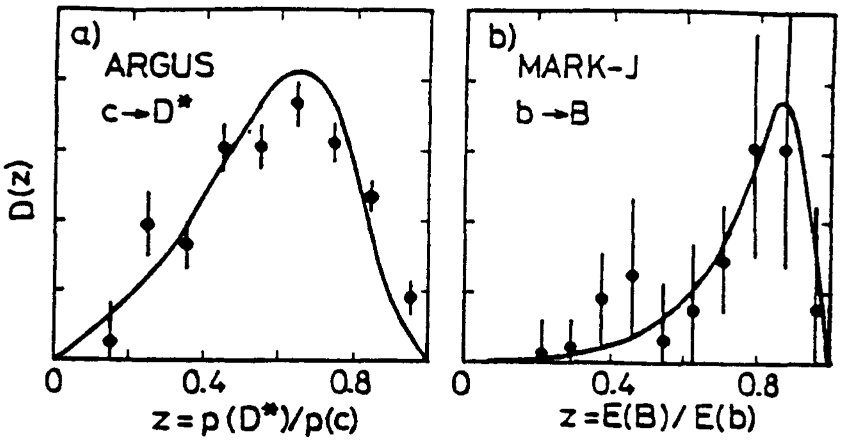

Figure 1.12

$c \to D^*$ and $b \to B$ fragmentation functions. The data is from the Argus and Mark-J experiments (Bari Conference 1985), and is compared to Peterson model calculations (solid lines).

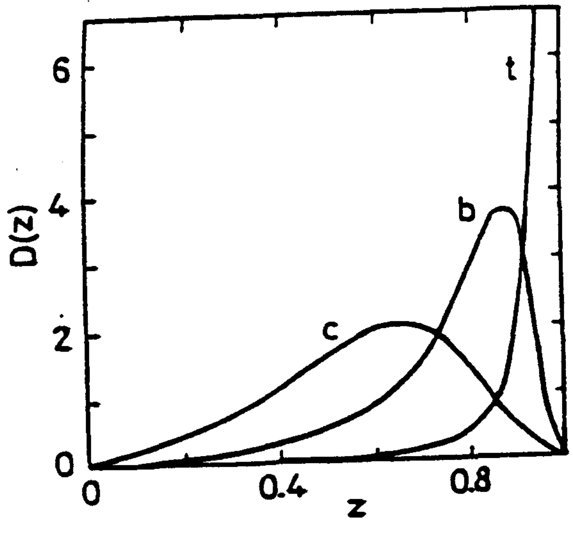

Figure 1.13

Comparison of Peterson model predictions for $Q = c, b, t$ quarks. ϵ=0.40 GeV/c^2/m_Q^2 with m_t=40 GeV/c^2.

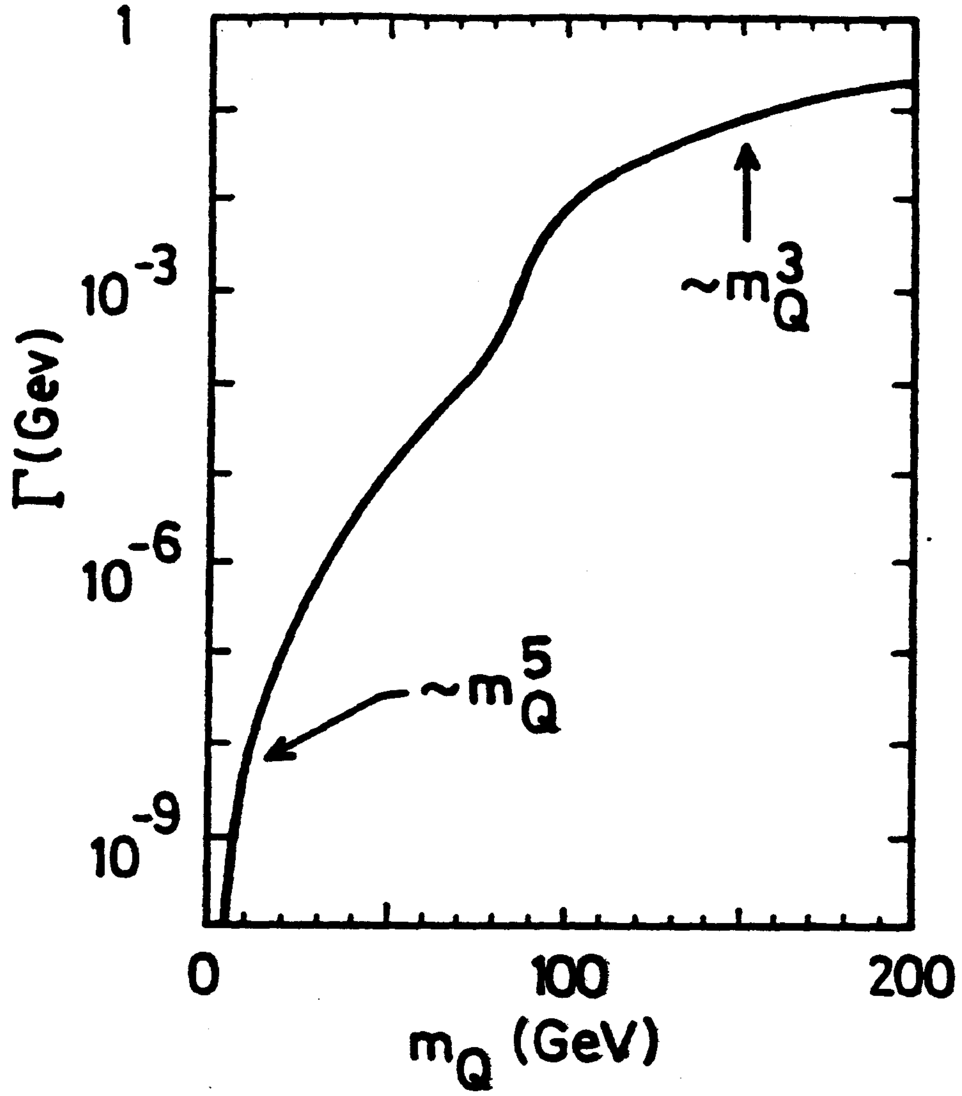

Figure 1.14

Dependence of the partial width for $Q \rightarrow qe\nu$ on m_Q.

2. APPARATUS

2.1 The Tevatron

The Collider Detector at Fermilab (CDF) was the first general purpose detector built at Fermilab to utilize the Tevatron. The Tevatron, a major upgrade to the original accelerator completed in 1982, is the worlds highest energy accelerator, which is currently operating at a beam energy of 900 GeV for a total center of mass energy of 1.8 TeV. The layout of the Fermilab accelerator is displayed in Figure 2.1.

The proton beam has its humble beginnings as a 750 KeV H^- ion beam produced from a Cockcroft-Walton electrostatic accelerator located in the Linac building. Immediately following this is a linear accelerator (Linac) which boosts the energy of the ions to 200 MeV. At the end of the linac, the H^- ions impinge on a thin foil which strips the two electrons to produce a bare proton for injection into the Booster ring. The Booster is a rapid cycling (15 Hz) alternate gradient synchrotron that increases the proton energy to 8 GeV. The typical number of protons per bunch in the Booster is 10^{10}. After circulating in the Booster, the protons are ready to be injected into the Main Ring. Before the construction of the Tevatron, the final accelerator at the Fermilab complex was the Main Ring. It is a 1 km in radius string of water cooled bending magnets and RF accelerator cavities located in a tunnel under several feet of earth. The Main ring accelerates the proton bunch to an energy of 150 GeV. At this point the protons are ready for their final transfer to the Tevatron where they are accelerated to their highest energy of 900 GeV. The Tevatron is located under the Main Ring in the same underground tunnel. Its bending magnets are superconducting and quite energy efficient.

Needless to say, antiprotons are required to conduct a $p\overline{p}$ colliding beam experiment. Antiprotons are produced by diverting 150 GeV protons in the main ring to a target in the antiproton source. This source consists of two concentric somewhat triangular accelerators rings: the Debuncher and the Accumulator. The Debuncher "cools" the initial antiprotons to reduce their momentum spread, and then stores them in the Accumulator. The typical stack rate is $4 \times 10^{10}\overline{p}$ hr^{-1}. Antiprotons are injected into the Main Ring in several bunches, coalesced, and injected into the Tevatron

This process is repeated six times to produce six counter revolving bunches each of protons and antiprotons in the Tevatron. A process known as "cogging" then takes place to position the collision point of the bunches at the center of CDF.

The luminosity of a store is around $6 \times 10^{30} cm^{-2} \cdot sec^{-1}$, with a lifetime (barring mishaps) of 12–24 hours. The slated integrated luminosity for the 92–93 collider run was 25 pb^{-1}, and 19.3 ± 0.7 pb^{-1} was delivered [1].

2.2 The CDF Detector

The CDF detector is a 5000 ton magnetic detector built to study $p\overline{p}$ collisions at a center of mass energy of 2 TeV. Perspective and cutaway views of CDF are shown in figures 2.2 and 2.3 respectively.

The coordinate system is displayed in figure 2.2. The z-axis points in the direction of the proton beam. The y-axis points skyward, and the x-axis points radially outward from the Main Ring. The azimuthal angle, ϕ, is 0° along the positive x-axis and increases to positive y. The polar angle, θ, is measured from the positive z direction. At CDF, θ is not used frequently, instead pseudo-rapidity, η, is employed. Where $\eta = -\ln(\tan\theta/2)$.

The construction of the detector is analogous to that of an onion with one set of detectors being encased by another. The first layers are utilized for tracking. The first tracking layer is a silicon detector (SVX) which provides precision tracking for tagging displaced secondary vertexes, next is a series vertex time projection chambers for locating the z-position of the primary interaction vertex, and finally a large central tracking chamber. All these detectors are surrounded by a superconducting cylindrical magnet with a field strength of 1.4 Tesla. Following the tracking chambers are the electromagnetic and hadronic calorimeters. The outer most layers are muon chambers.

2.3 Tracking

2.3.1 Silicon Strip Vertex Detector

The 1992–93 run saw the addition of a silicon strip detector (SVX) at CDF. The SVX provides high precision tracking which allows the resolution of secondary vertices from the decay of heavy-flavored particles with decay lifetimes in the range of 10^{-13}–10^{-12} seconds. This will allow, amongst other things, the tagging of b-quarks in $t\bar{t}$ events.

The SVX surrounds the interaction region and is located radially just outside the beryllium beam pipe. The length of the SVX is 50 cm, and is divided into two halves (barrels). The length is sufficient to cover most of the gaussian distribution ($\sigma \approx 30$ cm) of the collision region. Each barrel is divided into 12 30° wedges. (Figure 2.4.) Each wedge consists of four layers of silicon detectors or "ladders". All ladders are attached to a beryllium bulkhead with the inner layer having a radius of 2.99 cm and the outer layer having a radius of 7.85 cm. A placement accuracy of 10 μm for each of the detectors, coupled with a 5 μm barrel alignment will measure tracks with displacements $c\tau > 300\mu$m [17].

The SVX has a total of 46080 readout channels. This high channel density makes conventional readout methods utilizing a single cable per channel a daunting prospect indeed. A VLSI circuit was developed that contains 128 charge sensitive amplifiers per chip. During operation, incoming data are compared to a preset threshold and a latch is set for channels above threshold. When the chip is read out, digital circuits are switched sequentially to latched channels. For each latched channel, the analog voltage corresponding to the charge deposited on a strip is connected to a single analog bus and the channel address connected to a digital bus. This feature greatly reduces read out time since only active channels are read out.

Tracking is carried out in the R–ϕ plane only. No z information is provided due to the fact that the SVX is read out in long strips parallel to the beam axis. Complex offline FORTRAN routines produce tracks from information in each layer. A primary vertex is found first and secondary vertices are then found searching for three or more tracks close together and displaced several sigma from the primary vertex.

2.3.2 Vertex Time Projection Chamber

Surrounding the SVX and beam pipe are 28 vertex time projection chambers (VTX). The most important function of the VTX is to locate primary and secondary (i.e. "min bias" event) vertices along the beam axis. The z-distribution of the vertices follows a gaussian with a sigma of 30 cm. The VTX is divided into two halves. Each half has 14 modules, one of which is shown in Figure 2.5. Each module is divided into two 4.55 cm drift regions. Each region is then further divided into eight octants with either 16 or 24 sense wires per octant. The five furthest modules on either end have 24 wires to provide high eta coverage and extend from a radius of 6.53 cm to 21.11 cm. The inner nine modules on each side have 16 wires which extend from 10.96 cm to 21.11 cm. The larger inner radii for the inner nine modules is necessitated due to the presence of the SVX. The effective eta coverage of the VTX is ±3.5, and covers a length of 121 cm on each side with a 1.1 cm crack in the center.

Charged particles passing through the VTX knock electrons off the Argon/Ethane gas in the detector. The electrons migrate through an electric field with a drift velocity of 51 cm/nsec to the sense wires. The arrival times are converted into TDC counts. Utilizing the drift velocity, hit times on each wire, and the z-position of each wire, two–dimensional track segments in the R–Z view can be constructed. These track segments are then used to locate the z-position of the event vertex. Typical vertex z-resolution is a few millimeters. In some cases two two–dimensional segments can be combined to produce a full 3D fit with ϕ and curvature information, though the later is quite crude.

Another important function of the VTX is to identify photon conversions between the VTX and CTC. Conversion electron identification will be discussed in section 3.1.6.

2.3.3 Central Tracking Chamber

The Central Tracking Chamber (CTC) is a large 1.38 m in radius detector which occupies most of the bore in the 1.4 Tesla magnet. The most important function of the CTC is to provide precision momentum measurements of tracks with $|\eta| < 1.0$, and less accurately out to $|\eta| < 2$. The CTC surrounds the VTX and is 3.2 m long.

The tracking chamber has 84 layers of sense wires divided into nine superlayers. Wires in five of these superlayers are all parallel to the beam line. The other four superlayers have alternating layers of parallel and stereo wires, with the stereo wires offset by ±3° from the parallel wires. The offset wires allow two dimensional reconstruction in the R–Z plane, while parallel wires provide 2D R–ϕ information. Together, three dimensional tracks can be reconstructed with P_T, ϕ, η, impact parameter, and z-intercept information. The maximum drift time to any wire is 800 ns, which is less than the $p\bar{p}$ crossing rate of 3.5μs. Each superlayer is divided into 660 cells tilted 45° with respect to the radial direction. An electric field is setup perpendicular to the cell direction. The 45° tilt compensates for the Lorentz force resulting from $\vec{E} \times \vec{B}$ effects.

The performance of the CTC is very good. Unconstrained track P_T resolution is $\Delta P_T/P_T^2 = (0.0017 \text{ GeV/c})^{-1}$ for $|\eta| < 1.0$. The accuracy can be improved to $(0.0011 \text{ GeV/c})^{-1}$ by determining the displacement of the beam from the nominal position of $x = y = 0$ [18]. (This displacement is no more than a few hundred microns.) Beyond $|\eta| = 1.0$ the resolution degrades and stereo information is lost. The z-resolution for each layer less than 200μm, and the error in the z-position of the track is under one mm.

2.4 Calorimetry

Outside the tracking chambers, the electromagnetic (EM) and hadronic (HAD) calorimeters of CDF extend down to $|\eta| = 4.2$ or 1.7°. The calorimetry is segmented into uniform $\eta \times \phi$ towers that project back to the interaction region and provide fine grain resolution. The CDF calorimetry is divided into three major components: central/endwall ($|\eta| < 1.1$), plug ($1.1 < |\eta| < 2.4$), and forward ($2.4 < |\eta| < 4.2$). The properties of these detectors are summed up in Table 2.1, and the pseudo-rapidity coverage shown in Figure 2.7. The central EM calorimetry consists of alternating layers of lead and scintillating plastic, while the central HAD consists of steel and scintillator. The plug and forward regions utilize gas proportional chambers instead of scintillator, with lead layers in the EM and steel in the HAD compartments.

The purpose of calorimetry in the top search is to locate and measure jets and electrons. Missing transverse energy due to neutrinos can be determined by measuring energy imbalances in the calorimeters.

2.4.1 Central Region

The central calorimeter is divided into 24 fifteen degree wedges on the $+z$ and $-z$ sides of the detector for a total of 48 wedges, arranged in a barrel configuration. Each wedge is divided into 10 projective towers of $\Delta\eta \times \Delta\phi = 0.11 \times 15^\circ$ that point back to the center of the detector. The coverage is $\eta < |1.1|$, and a full 2π in azimuth.

The central EM (CEM) is closer to the CTC than the hadronic portion, and has an inner radius of 172 cm. The CEM is a lead-scintillator calorimeter and consists of 31 layers of 5 mm thick polystyrene scintillator interleaved with 30 layers of 0.125 inch thick lead clad with 0.015 in of aluminum. This produces a calorimeter with 18 radiation lengths of material. Light from each tower is piped to two phototubes via wavelength shifters. The energy resolution for the CEM is $\Delta E/E = 13.5\%/\sqrt{E_T} \oplus 2.0\%$ [19], where the two terms are added in quadrature [20]. The total weight per wedge is two tons. See Figure 2.8 for details.

Imbedded at a depth of 5.9 radiation lengths in the CEM, at shower maximum, are the proportional wire chambers (CES). These wire chambers determine shower position at shower maximum by measuring charge deposited on orthogonal strips and wires. The CES is a multiwire gas detector with anode wires oriented parallel to the beam axis and cathode strips oriented perpendicular to the beam axis. The transverse profile of a shower is constructed from the wire and strip information. A χ^2—which estimates a goodness of fit to electron shower profiles measured in a testbeam—is produced from the profile information. This χ^2 provides good pion and photon rejection.

The central hadronic calorimeter is divided into two major sections: The true central part (CHA) that lies outside of the CEM, and the endwall section (WHA) which extends the central hadronic eta coverage to match that of the CEM. The CHA and WHA have the same η–ϕ segmentation as the CEM. 48 one inch thick steel-scintillator layers make up the CHA, while the WHA has 32 two inch thick layers. The energy resolution is approximately $\Delta E/E = 80\%/\sqrt{E_T}$ [20]. The CHA/WHA TDC's provide timing information that is used to reject cosmic rays, Main Ring particles or other out-of-time backgrounds.

Following the magnet and preceeding the CEM, central preradiator chambers (CPR) were added for the 1992–93 collider run. The CPR consists of 96 chambers filled with Argon/Ethane. Each chamber is 15.1 inches wide by 95 inches long by 0.310 inches thick. 32 sense and 31 field wires are strung in each CPR module parallel to the beam pipe and are sandwiched between two 1.6 mm thick sheets of copper clad G10. Charged particles and showers passing through the CPR deposit charge on the sense wires. The electron pulse height distribution in the CPR will be broader than that for charged pions since electrons are more likely to preshower in the coil than hadrons. This additional information will be used to reduce pion backgrounds which will allow more accurate identification of electrons from $b \rightarrow e + X$ in $t\bar{t}$ decays.

2.4.2 Plug and Forward Calorimeters

The plug and forward calorimeters round out the η coverage. Energy sampling is carried out using argon/ethane gas proportional chambers interspaced between lead or steel. Cathode read out pads and wires allow a fine grain projective tower size of $\Delta\eta \times \Delta\phi = 0.09 \times 5^\circ$. The resolution of these detectors is approximately $\Delta E/E = 30\%/\sqrt{E_T}$ for electrons and $\Delta E/E = 120\%/\sqrt{E_T}$ for jets [20].

2.5 Muon Detectors

Prior to the 1992-93 collider run, there existed two muon detection systems: the central muon system (CMU) and a forward/backward muon system (FMU). The CMU covers $|\eta| < 0.63$ or down to 56°. 24 phi cracks reduced the azimuthal coverage to 84%. Covering $1.96 < |\eta| < 3.64$ or 3° to 16°, the FMU provides coverage at small angles. It consists of two magnetized steel toroids with drift chambers and scintillation counters placed in front of, in the middle, and in back of the toroids. The FMU was not used in this analysis and will not be discussed further.

The current run saw the addition of two more muon detectors: the central muon upgrade (CMP), and the central muon extension (CMX). The CMP provides additional absorption lengths of material and enhanced ϕ coverage in the region covered by the CMU, while the CMX extends the η coverage ($0.65 < |\eta| < 1.0$ or 42° to 55°) with about 75% azimuthal acceptance.

2.5.1 Central Muon System

Muons that penetrate the 4.9 absorption lengths of material in the central calorimeters will pass through the CMU chambers where their position and momentum are measured. The CMU begins at a radial distance of 3470 mm from the beam axis. The muon detectors subtend 12.6° of each 15° calorimeter wedge and are made up of three modules mounted side by side. A drawing showing the location of the CMU is displayed in Figure 2.9. Each detector cell has a length of 2261 mm and a width of 63.5 mm, with a 50 μm charge collecting wire running down the length of each cell. Four cells stacked vertically constitute a module. (See Figure 2.10.) Charge division allows determination of the z-position along the wire.

When a particle traverses the cells it passes four wires. The ϕ angle is determined by timing information from each of the four wires. Two of the wires in alternating cells are offset by 2 mm from the other two wires. By determining which pair of sense wires were hit first the ϕ ambiguity (i.e., which side of a wire the particle passed) can be determined. The angle α between the track and sense wires is calculated by measuring the difference in arrival times of the drift electrons. The P_T of the particle can be estimated using the formula:

$$\sin\alpha = \frac{eL^2B}{2DP_T}. \tag{2.1}$$

Where e is the charge of the electron, L = 1440 mm is the radius of the solenoidal magnetic field, B = 1.412 Tesla, D = 3470 mm is the radial distance to the muon chambers, and P_T is the transverse momentum of the particle. The resolution, taking into account multiple scattering, is

$$\frac{\sigma(P_T)}{P_T} = \frac{\sigma(\alpha)}{\alpha} = 67\%. \tag{2.2}$$

2.5.2 Central Muon Upgrade

Muon detection in the central region is very important since leptons from top decay are produced at low $|\eta|$. The CMU has 5.4 pion interaction lengths of material, hence about 0.5% of hadrons will penetrate to the CMU detectors. With increased luminosity, it is important to reduce the rate of "fake" muons resulting from hadronic punch though. The CMP adds 3.0 pion interaction lengths to reduce the punch through rate to 0.022%.

The CMP consists of a set of muon chambers constructed behind a 60 cm thick × 640 cm long × 470 cm high steel wall with a weight of 315 tons. There are two of these walls, one on the north side and one on the south side of the detector at a distance of 535 cm from the beam pipe. This configuration is shown in Figure 2.11. The drift chambers are secured behind the steel walls. Each chamber is 2.54 cm × 15.24 cm on a side and 640 cm long. They operate in a similar fashion to the CMU chambers with four cells stacked horizontally with offset wires. The z-position is found using charge division. The pseudo-rapidity coverage is $|\eta| < 0.7$.

In addition to the chambers located behind the steel wall, extra muon chambers were placed on the top and bottom of the iron return yoke for further coverage. These extra muon chambers will help fill in some of the ϕ gaps present in the CMU.

2.5.3 Central Muon Extension

In order to extend the coverage further, a system of drift cells with supporting structures needed to be constructed. The CMX coverage in eta is $0.65 < |\eta| < 1.0$, so there is a slight overlap between the CMU and CMP. Unlike the CMP, no additional steel was added between the calorimeters and the CMX muon chambers; the amount of material traversed is greater at higher $|\eta|$ than that encountered in the CMU. Twelve 15° sectors make up the CMX on the east and west side of the detector. Each drift chamber is 180 cm long by 15 cm wide by 3 cm thick. Chambers are stacked four thick. (ϕ, η) of the track is found using the same principles as used by the CMU.

2.6 Trigger

The $p\bar{p}$ interaction rate at CDF is approximately 350 KHz at a luminosity of 7×10^{30} cm^{-2} sec^{-1}. The output rate to 8 mm magnetic tape is limited to three to four Hertz. In order to reduce the huge input rate, a series of filters or triggers is required. These triggers must be designed to reject "uninteresting" events while passing events worthy of further study, as well as events that might indicate new physics processes. The CDF trigger system consists of four stages which are expanded upon below.

The lowest level trigger is the Level–0 trigger which selects inelastic $p\bar{p}$ collisions. Two sets of beam–beam scintillation counters (BBC) are located between the plug and forward calorimeters on both the east and west sides of the detector. (See Figure 2.2 for the location, and Figure 2.12 for a diagram of a BBC plane.) Each plane consists of 16 time-of-flight counters covering $3.24 < |\eta| < 5.9$.

The next two levels are the Level–1 and Level–2 triggers. The Level–1 trigger decision is made in the 3.5 μs between crossings. During this time electromagnetic, hadronic, and total transverse energy is summed from towers registering energies above 0.1 GeV. The missing transverse energy is computed from this information. Electron clusters are identified by a hardware cluster finder that searches the EM towers forming clusters around seed towers with $E_T > 4$ GeV. These clusters are matched to high momentum tracks reconstructed from a fast two-dimensional hardware track finder (CFT). A Level–1 electron trigger is considered final if cluster $E_T^{EM} > 12$ GeV, and the ratio of hadronic E_T to electromagnetic E_T in the cluster is less than 0.125. The Level–1 muon trigger registers candidates by identifying muon stubs in the muon chambers. Their direction and P_T are estimated as outlined in section 2.5.1.

Level–1 triggers at a rate of a few KHz. If an event passes the Level–1 trigger, it is passed to the Level–2 trigger which takes 10μs to make a decision. This is enough time to acquire features of the transverse energy deposition, such as energy distribution in clusters, cluster invariant mass, and tracks associated with clusters. This information is analyzed by Level–2 hardware processors to further identify or reject high E_T electron and muon candidates, photons, jets, taus, high missing E_T events, and so on. Electrons in Level–2 require a match in ϕ with a track, along with other track quality and calorimeter cuts. Level–2 muons are flagged by matching stubs to tracks produced from the CFT with $P_T > 5$ GeV/c. If Level–2 accepts an event, the whole detector is digitized and read out over a period of 1 ms. The output rate to the Level–3 trigger is around 10 Hz.

The final online trigger system is Level–3. Unlike the previous three triggers, Level–3 is not hardware trigger, but a software trigger running on a farm of microprocessor computers that utilizes algorithms written in FORTRAN to select events.

The digitized output from Level–2 is processed through an Event Builder which converts the data into a standard CDF format. Level–3 utilizes better clustering algorithms, and includes detector response maps, superior tracking ability, etc., that are not available with the hardware filters. Roughly half the events survive this trigger, and those are written to tape for offline analysis.

Table 2.1

A summary of the calorimeter properties by system.

	Central		Endwall	Endplug		Forward	
	EM	Hadron	Hadron	EM	Hadron	EM	Hadron
$\lvert\eta\rvert$ coverage	0–1.1	0–0.9	0.7–1.3	1.1–2.4	1.3–2.4	2.2–4.2	2.3–4.2
Tower size, $\Delta\eta \times \Delta\phi$	$-0.1\times15^\circ$	$-0.1\times15^\circ$	$-0.1\times15^\circ$	$0.09\times5^\circ$	$0.09\times5^\circ$	$0.1\times5^\circ$	$0.1\times5^\circ$
Longitudinal samples in tower	1 [a]	1	1	3	1	2	1
Active medium	polystyrene scintillator	acrylic scintillator	acrylic scintillator	Proportional tube chambers with cathode pad readout		Proportional tube chambers with cathode pad readout	
Scintillator thickness or proportional tube size	0.5 cm	1.0 cm	1.0 cm	0.7×0.7 cm^2	1.4×0.8 cm^2	1.0×0.7 cm^2	1.5×1.0 cm^2
Number of layers	31	32	15	34	20	30	27
Absorber	Pb	Fe	Fe	Pb	Fe	94%Pb, 6% Sb	Fe
Absorber thickness [cm]	0.32	2.5	5.1	0.27	5.1	0.48	5.1
Typical phototube or wire high voltage [V]	−1100	−1500	−1100	+1700	+2120	+1900	+2200
Typical phototube or wire gain	1.2×10^5	6×10^5	10^6	2×10^3	2×10^4	5×10^3	10^4
Typical tower signal [pC/GeV]	−4	−4	−4	+1.25	+1.3	+2	+0.7
Energy (σ/E) resolution at 50 GeV [%]	2	11	14	4	20	4	20
Typical position resolution at 50 GeV [cm^2]	0.2×0.2 [a]	10×5	10×5	0.2×0.2	2×2	0.2×0.2	3×3
Characteristic width of azimuthal boundary region [cm]	3.5	4.1	3.8, 8.9 alternating	0.9	0.8	0.7; 3.2 [b]	1.3; 3.2 [b]

[a] An imbedded proportional tube chamber at shower maximum gives some additional information. The quoted position resolution is measured with this chamber.

[b] The first number is for the vertical boundary, the second for the horizontal.

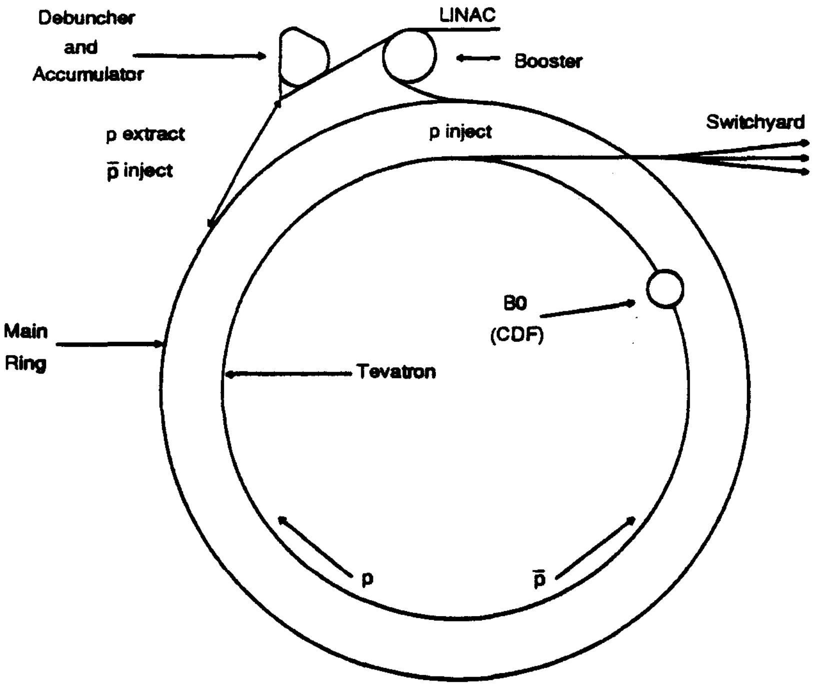

Figure 2.1

The Tevatron Accelerator. The Main Ring and the Tevatron ring have the same radius, but are drawn differently for clarity.

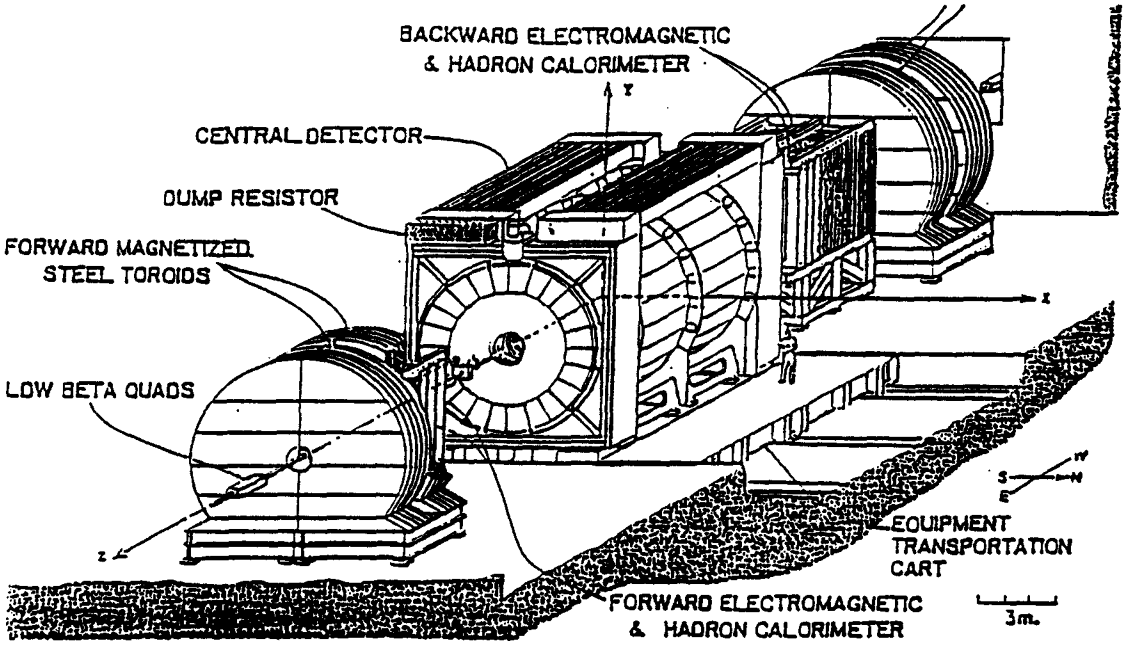

Figure 2.2

A perspective view of the CDF detector. The central detector and the forward and backward detectors are shown.

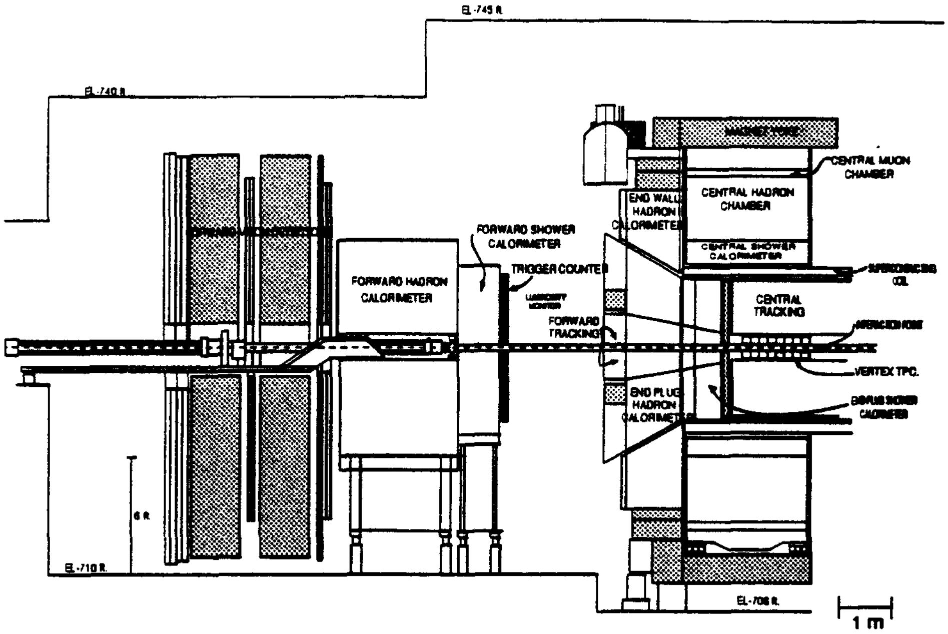

Figure 2.3

A cut-away view through the forward half of CDF. The detector is forward-backward symmetric about the interaction point.

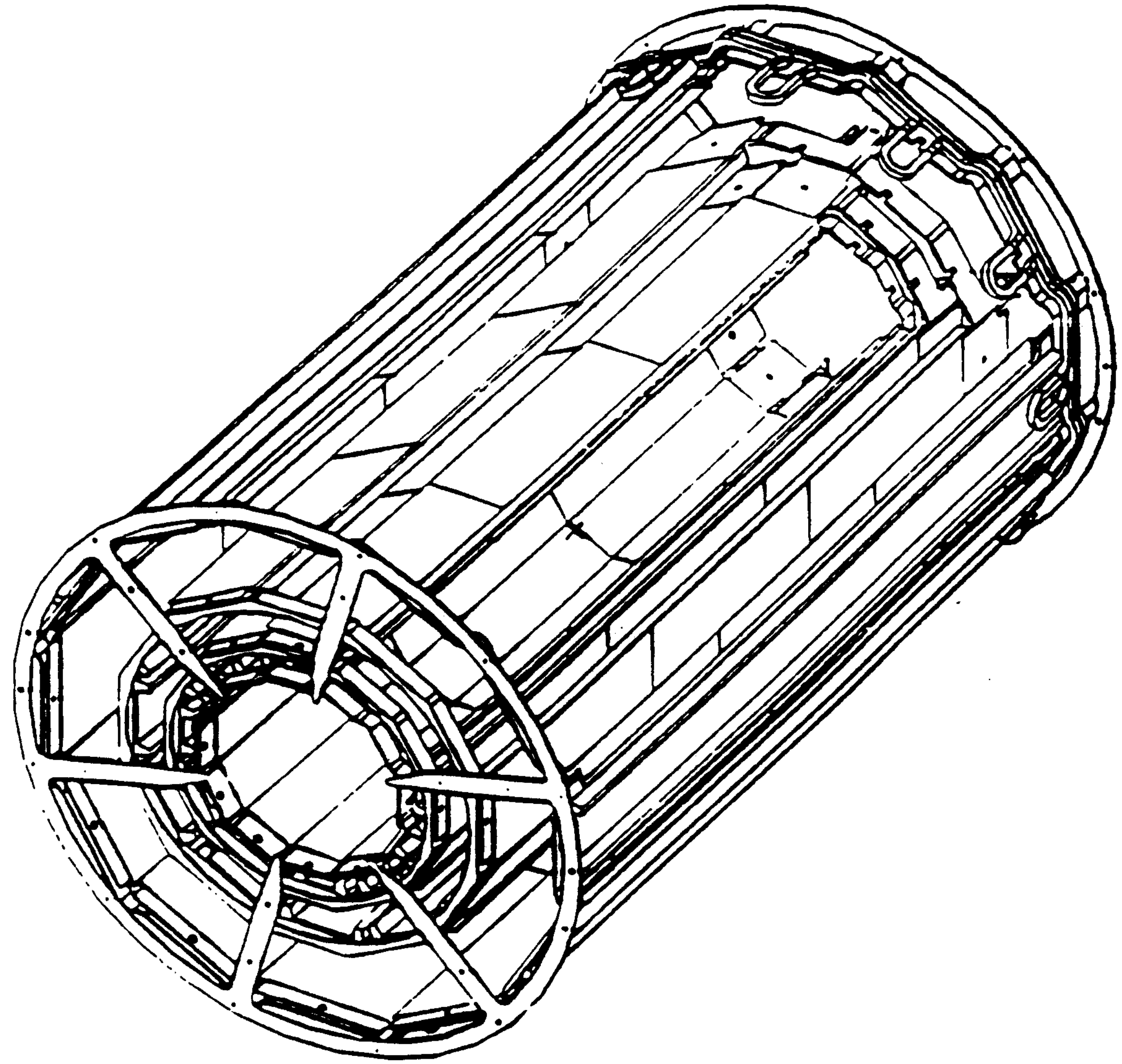

Figure 2.4

Schematic view of one SVX barrel showing the internal geometry.

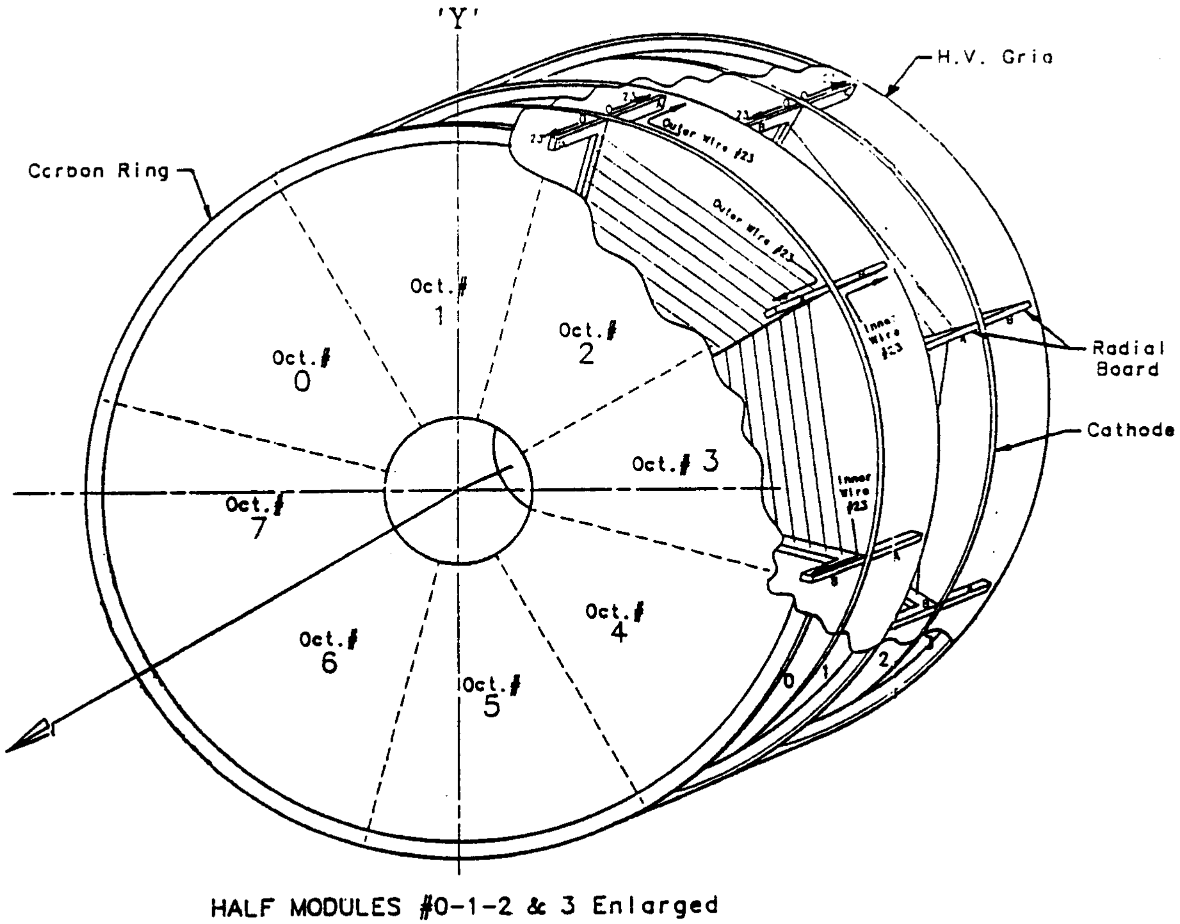

Figure 2.5

An isometric view of one VTX module.

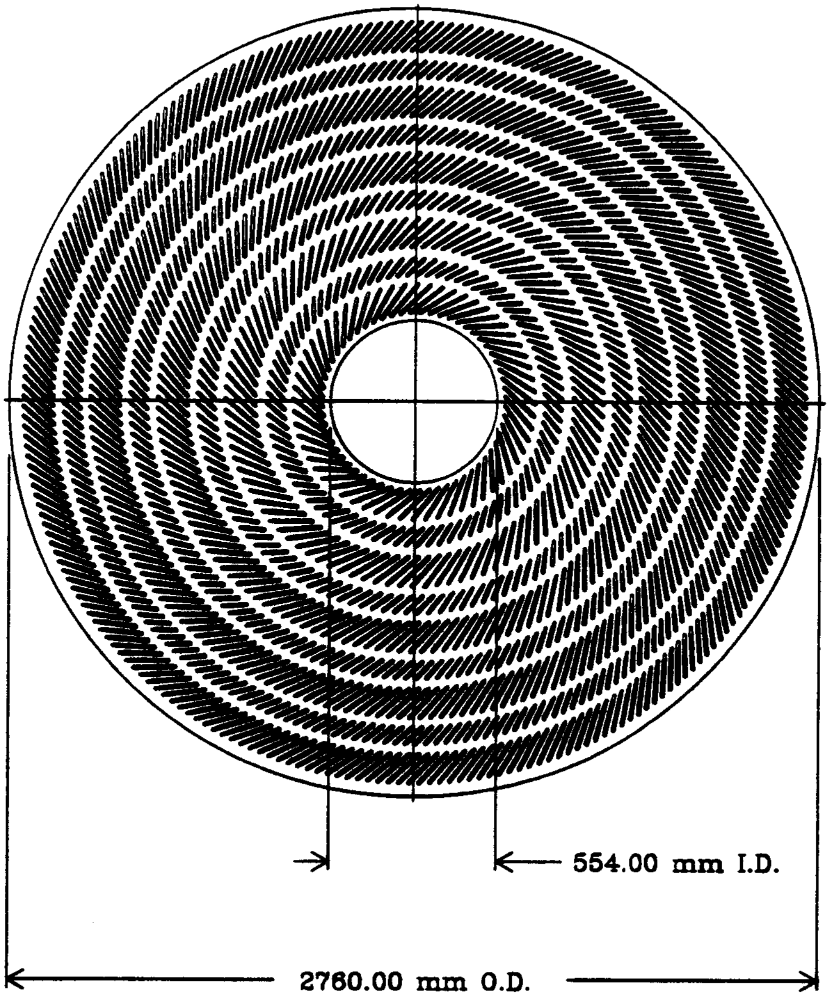

Figure 2.6

End view of the Central Tracking Chamber. The location of the slots in the aluminum endplates for the wires are shown.

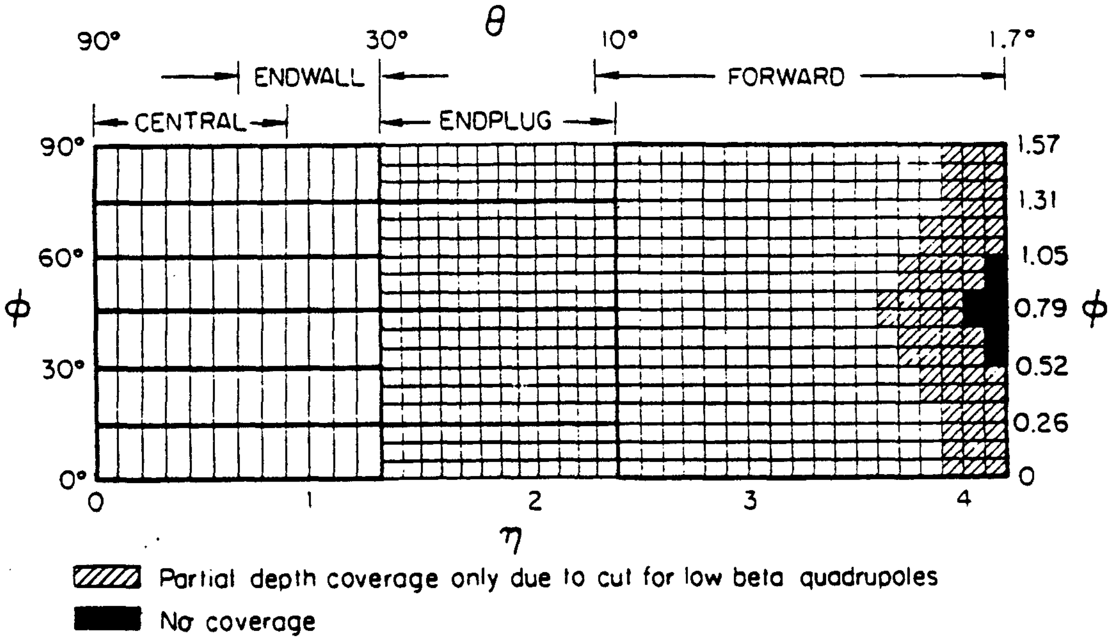

Figure 2.7

η coverage of the calorimetry.

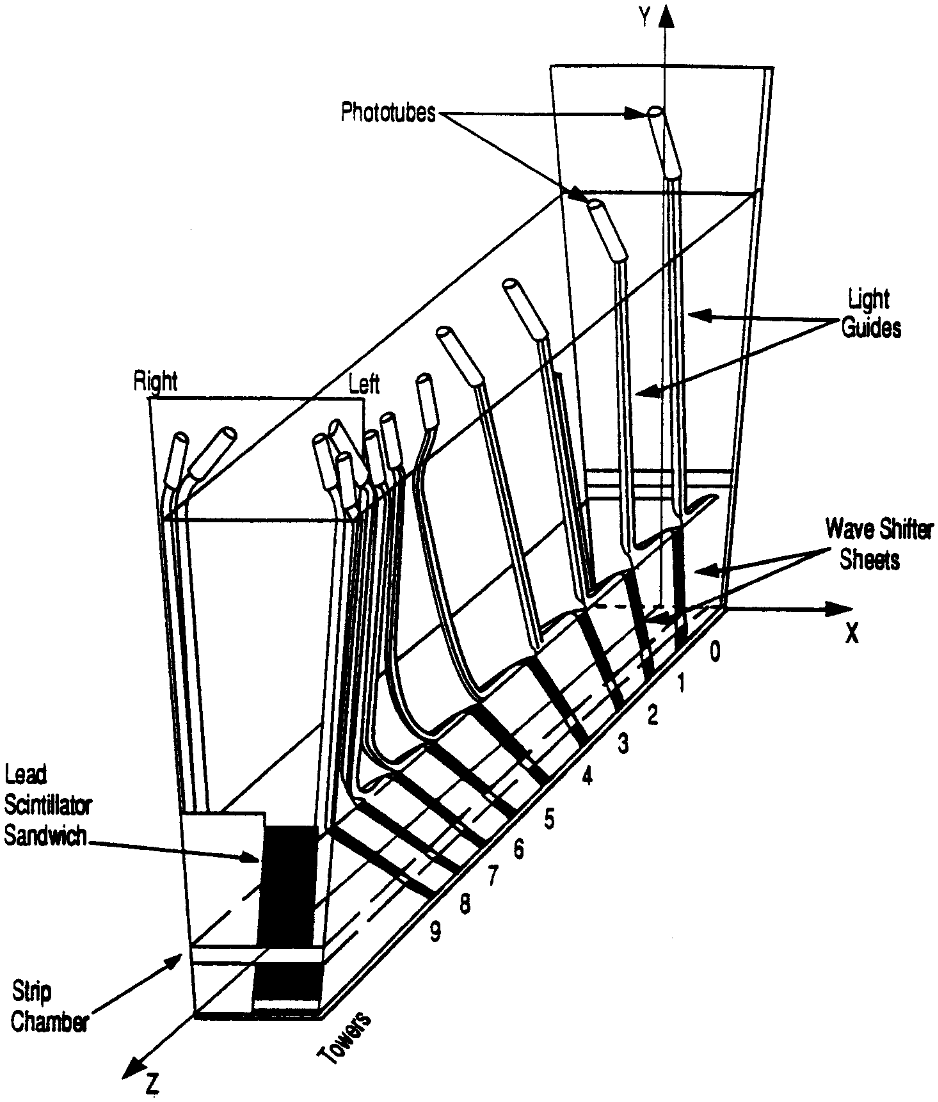

Figure 2.8

X-ray view of the CEM. The layout of the light-gathering system and strip chamber location for the CEM is revealed. The light guides run past the CHA compartment in the upper 2/3 of the wedge.

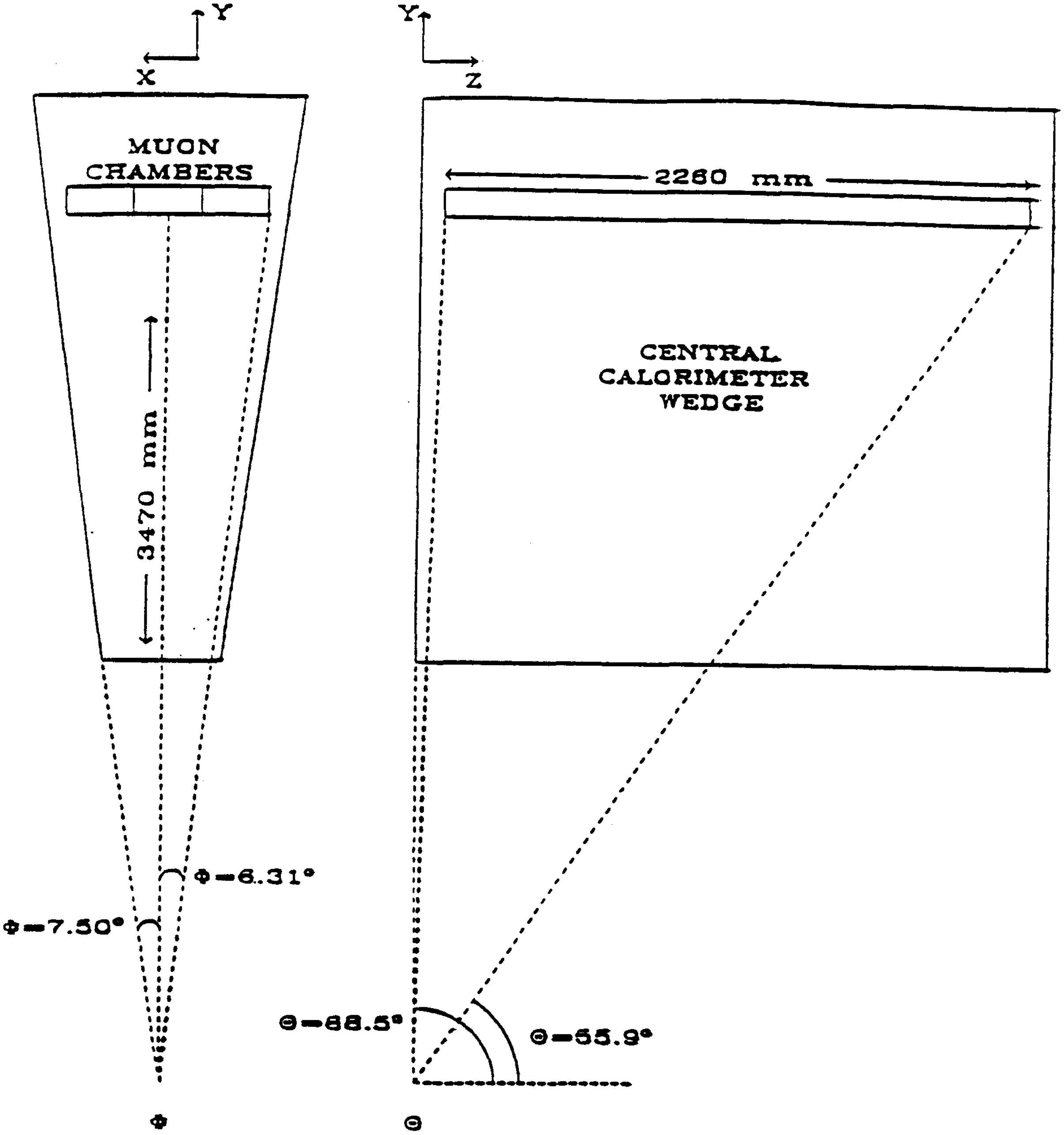

Figure 2.9

Location of the central muon chambers within the central calorimeter.

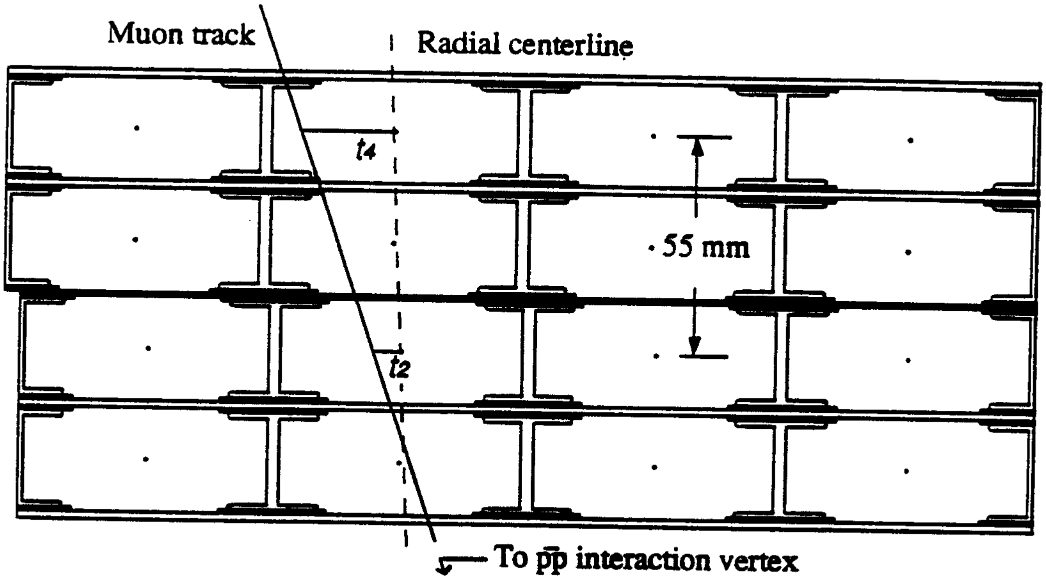

Central muon drift chambers showing the location of drift wires.

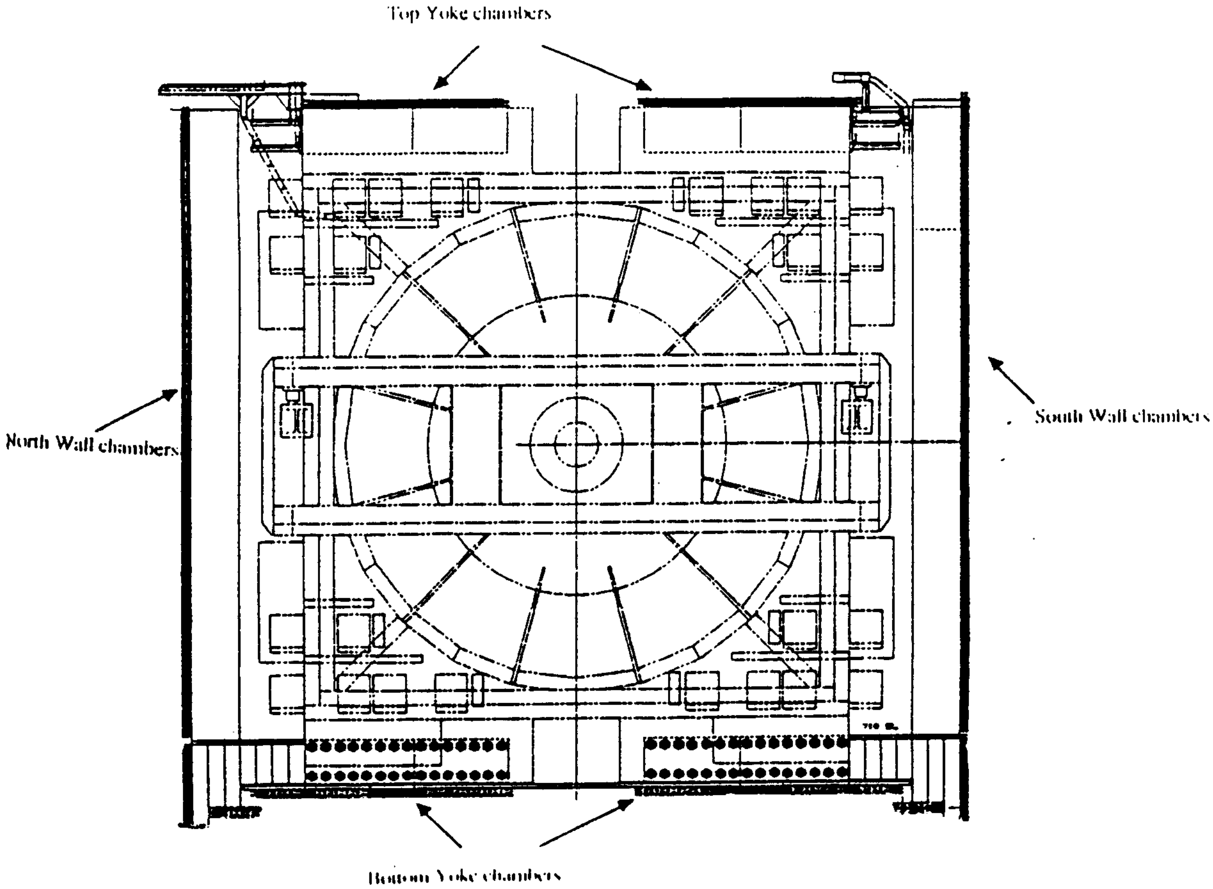

Figure 2.11

Schmatic view of the components of the central muon upgrade.

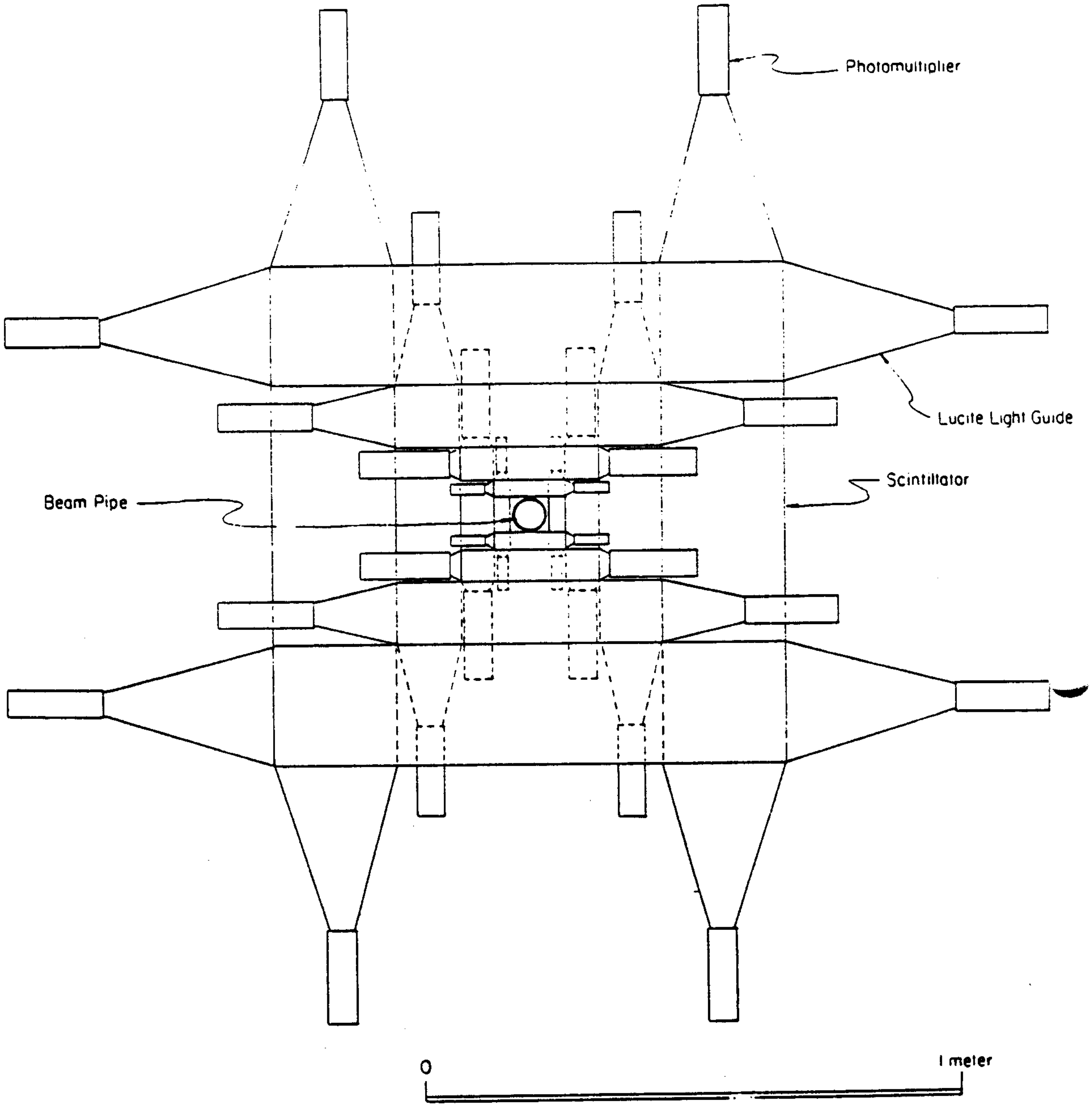

Figure 2.12

A beam's-eye view of one set of beam-beam counter planes.

3. EVENT SELECTION

This chapter is devoted to the discussion of the electron and muon data sets used in this analysis. The inclusive electron and muon triggers are described as well as the parameter cuts used to further refine the samples. The efficiency of these cuts is then calculated. A discussion of jet clustering and the missing transverse energy rounds out this chapter.

3.1 Inclusive Electron Selection

3.1.1 Inclusive Electron Trigger

The Level–1 electron trigger uses information from the calorimeters, which at the trigger level are available with a $\Delta\eta \times \Delta\phi = 0.2 \times 15^\circ$ segmentation. The central electron trigger requires at least one EM tower with $E_T > 3$ GeV. The efficiency of the Level–1 trigger is $99.18 \pm 0.08\%$ [21].

The Level–2 central electron trigger requires the existence of a CFT track (section 2.6) with $P_T > 9.2$ GeV/c that points to a CEM cluster of $E_T^{EM} > 9$ GeV. This Level–2 EM cluster was constructed by selecting a "seed" tower with $E_T^{EM} > 4$ GeV and adding the E_T^{EM} of adjacent towers with $E_T^{EM} > 3.6$ GeV. If any neighboring towers to the just mentioned adjacent towers have $E_T^{EM} > 3.6$ GeV then they too are added to the cluster. This process continues until no new towers are added. The ratio of hadronic to electromagnetic energy for this cluster must be less than 12.5%. Level–1 and 2 calculate E_T at $z = 0$ cm, not at the event vertex. The efficiency of the Level–2 CEM trigger has been determined from studying W and Z^0 events, and is 92.8 ± 0.3% [21] for electrons with $E_T > 20$ GeV.

At Level–3, a streamlined version of the offline reconstruction code is run on the Level–2 output. The clustering is redone, but with a finer calorimeter segmentation. The E_T calculated at Level–3 must be above 18 GeV. A CTC track with $P_T >$ 13 GeV/c must also be present and must extrapolate to within 3.0 cm of the center of the CEM cluster in the x–view and 10.0 cm in the ϕ–view. Furthermore, the CEM cluster must have a strip $\chi^2 < 10.0$, and a $L_{shr} < 0.2$. These variables will be described later in this chapter.

3.1.2 Electron Selection Criteria

After an event has passed the above electron triggers, it is written to tape for later offline analysis. Electron candidates are required to have a CTC track associated with an electromagnetic cluster. The superb resolution of the CTC and the central strip chambers allow track–EM cluster matching in the z and ϕ views to within a few cm. Electron showers are small and are usually contained within one or two towers. The border between the CEM towers in the ϕ direction contains approximately one cm of inactive material which effectively prevents showers from crossing ϕ boundaries. With this constraint, CEM clusters are allowed to be contained in three or fewer towers in the same wedge. The E_T of the electron is calculated as $E \sin\theta$, where E is the energy of the tower, and θ is the polar angle of the EM cluster from the track vertex.

3.1.3 Central Electron Parameters

In this section the variables used to select electrons will be defined, as well as the values of the cuts used. An analysis of $Z^0 \rightarrow e^+e^-$ decays will yield the efficiencies of these cuts.

3.1.3.1 Fiducial Region

Electron candidates are required to be within a fiducial volume to ensure that the electron is well measured. The definition of the CEM fiducial region is as follows:

- The CES x–position must be no farther than 21.0 cm from the tower center.
- $|z| > 9.0$ cm. (Avoids 90° crack.)
- Cluster resides in towers 0-8 or $|z| < 230$ cm.
- Tower 7 of the "chimney module" is excluded.

3.1.3.2 Energy

The energy is obtained from the EM and hadronic compartments of the electron tower(s). This raw energy is then corrected for four effects: First, a CEM mapping correction is applied as a function of shower position as determined by the strip chambers in each tower. This correction is based on testbeam data. Next a tower-to-tower correction is enacted which normalizes the energy to the track momentum based an a large sample of high-E_T electrons. Then, the energy is corrected for time and temperature variations. Finally, a global energy correction is made based on the E/P distribution of W electrons to that of a W Monte Carlo.

3.1.3.3 Momentum

The track assigned to the CEM cluster is the one with the best track-CES match. (If a CEM cluster is produced by a photon there may be no track attached to the cluster.) The initial momentum measurement is then recalculated by "beam constraining" the track. Beam constraining is performed by minimizing a χ^2 that describes the helical parameterization of the track, while requiring the track to pass through the VTX located vertex. The initial position of the track is found using the CTC. The beam constrained resolution is $\Delta P_T/P_T^2 = (0.0017\ \text{GeV/c})^{-1}$, which is worse then the energy resolution of the calorimeter, but the CTC track possesses a more accurate direction vector than the CEM.

3.1.3.4 Transverse Energy

The transverse energy is defined as $E_T = E \sin\theta$, where E is the corrected energy, and θ is the polar angle of the associated track.

3.1.3.5 Hadronic to Electromagnetic Ratio

The ratio of hadronic to electromagnetic energy (Had/EM) in the EM cluster allows discrimination between hadrons and electrons. Hadronic showers generally do not start until the CHA calorimetry, and deposit much more energy there then the small leakage into the CHA typical of EM showers. This distribution can be seen in Figure 3.1 for $Z^0 \rightarrow e^+e^-$ events.

3.1.3.6 Lateral Shower Profile

The Lateral Shower Profile, L_{shr}, is used to identify electrons by comparing the lateral shower profile to test beam data and is defined as

$$L_{shr} = 0.14 * \sum_i \frac{E_i^{Adj} - E_i^{Prob}}{\sqrt{0.14^2 * E + (\Delta E_i^{Prob})^2}}. \tag{3.1}$$

Where E_i^{Adj} is the measured energy in the tower adjacent to the seed tower; E_i^{Prob} is the expected energy in the adjacent tower inferred from the seed tower energy of the EM cluster, the position from the strip chamber, and the event vertex using a test beam shower profile parameterization; E is the EM energy; and ΔE_i^{Prob} is the expected error in E_i^{Prob} assuming a 1 cm error in the strip chamber position. The sum is over towers in the cluster adjacent to the seed tower in the same ϕ wedge. Due to the fact that L_{shr} is derived from measurements of electrons, there will be large differences in the lateral profile between a jet and an electron. This arises because electron showers tend to be much narrower then showers due to jets. A plot of L_{shr} from Z^0 events is shown in Fig 3.2.

3.1.3.7 Strip Chamber Profile

Section 2.4.1 describes a gas proportional chamber, CES, that is located at shower maximum in the central EM calorimeter. The shape of the strip chamber shower profile is compared to the transverse profile of an electron shower measured in the testbeam. Two χ^2's—χ^2_z and χ^2_ϕ—which estimate the goodness of fit to the electron hypothesis are constructed. χ^2_z is defined as

$$\chi^2 = \frac{1}{4}\left(\frac{E_{CEM}}{10}\right)^{0.747} \cdot \sum_{i=1}^{n} \frac{q_i^{obs} - q_i^{pred}(z)}{(\sigma_i(z))^2}, \tag{3.2}$$

where i in this analysis runs from 1 to 11. Here q_i^{obs} is the measured strip pulse height normalized to the total charge of the 11 channels; $q_i^{pred}(z)$ is the predicted normalized pulse height at a position z based on test beam data; E_{CEM} is the energy of the cluster; and $\sigma_i(z)$ is defined as

$$\sigma_i^2(z) = (0.026)^2 + (0.096)^2 q_i^{pred}(z). \tag{3.3}$$

The factor in front of the sum in equation 3.2 is introduced to obtain an energy independent χ^2. χ^2 is computed in the z and ϕ directions.

These variables are used to discriminate against events where more than one particle hits the calorimeter, as is in the case where a charged track overlaps a neutral pion showering in the CEM. Unfortunately, above approximately 20 GeV, $\pi^0 \rightarrow \gamma\gamma$ have their photons so closely spaced they behave as a single photon, and thus have a small χ^2 consistent with that of an electron. However, using the E/P ratio (see section 3.1.3.9), these events will be rejected. Figure 3.3 shows χ^2_z in the strip or z view.

3.1.3.8 Strip-Track Matching

The CES provides another valuable service: the accurate location of shower max in the x and z views. The location of the shower in z is found by the minimizing the following function:

$$X^2(z,E) = \sum_{i=1}^{n} \frac{(E_i^{obs} - Eq_i^{pred}(z))^2}{\sigma_i^2(z)}. \tag{3.4}$$

Where E_i^{obs} is the measured energy in each of the 11 channels; the other variables are defined above. The x location is found in a likewise fashion.

In order to match the CTC track to the strip position, the track is extrapolated to the radius of the CES, and the differences in positions in the x and z view computed. This provides further protection against charged tracks overlapping neutral pions or photons showering in the CEM. The ΔX and ΔZ distributions for isolated Z^0 events are plotted in figures 3.4 and 3.5 respectively.

3.1.3.9 Energy-Momentum Ratio

The ratio of the corrected EM cluster energy to the beam constrained track momentum ($E/P = E_T/P_T$) is used to ensure that the energy of the cluster matches the momentum of the particle that is presumed to have caused the shower. This cut selects out events where a neutral pion overlaps some charged particle. It is also useful in removing events where a high E_T photon overlaps a charged track as the E/P ratio for this type of event should be much larger than 1. The E/P ratio for electron events should be slightly larger than 1 because the calorimeter accepts energy from any other particles that radiate in it. See fig 3.6 for the relevent histogram.

3.1.3.10 Vertex-Track Separation

The difference between the track vertex and primary vertex found by the VTX should be small, as the resolution of the VTX and CTC are under one cm. Any tracks separated by more than a few centimeters from the primary vertex did not come from it, and such electron candidates should be dropped. See figure 3.7 for this distribution.

3.1.3.11 Impact Parameter

The impact parameter, $d0$, of a CTC track is defined as the minimum radial distance between the track and the beam line. Interactions from $p\bar{p}$ collisions are produced within 1 mm of the beamline, so any tracks produced with an impact parameter greater than this are most likely to be decays in flight or poorly reconstructed tracks. Figure 3.8 plots the impact parameter for Z^0 events.

3.1.3.12 Border Energy

The border energy, BE, is defined as the total energy in the corner and side towers surrounding the tower(s) in the electron cluster. This is a measure of the electrons isolation. And as was discussed in section 1.3, leptons from top decays should be well isolated. Figure 3.9 is a histogram of the BE for electrons in Z^0 events.

3.1.3.13 Isolation

Another method of measuring the isolation an electron is by summing all the transverse energy in a cone around the electron cluster. The "radius" of the cone is defined as $R = \sqrt{(\Delta\phi)^2 + (\Delta\eta)^2}$. The typical cone radius chosen is $R = 0.4$. The isolation is then defined as $Iso(R) = E_T^R - E_T^{cluster}$, where E_T^R is the transverse energy in the cone of radius R, and $E_T^{cluster}$ is the transverse energy of the cluster.

3.1.4 The Central Electron Cuts

Listed below is the summary of the quality cuts imposed on the inclusive central electron dataset:

1. The CES measured shower location must be within the fiducial volume.
2. $Had/EM < 0.05$
3. $L_{shr} < 0.2$
4. $\chi^2_{strip} < 10$. No cut on χ^2_{wire} is made because the wire profile is more distorted by bremsstrahlung photons from high energy electrons than in the strip shower profile.
5. $|\Delta X^{track-strip}| < 1.5$ cm
6. $|\Delta Z^{track-strip}| < 3.0$ cm
7. $E/P < 1.5$
8. $|Z_{track} - Z_{vertex}| < 5.0$ cm
9. $d0 < 0.2$ cm

These variables have been plotted in figures 3.1 to 3.8. The vertical arrows delimit where the cuts are made. The efficiency of these cuts is cuts is described in the next section.

3.1.5 Electron Selection Efficiency

3.1.5.1 The Method

Determining the efficiency of the central electron cuts begins by selecting a sample of $Z^0 \rightarrow e^+e^-$ events where at least one leg must pass all the selection cuts. Then, the invariant mass of the two legs must fall within a window around the Z^0 mass. To calculate the efficiency, assume N_Z is the number of Z^0's in the sample and N_2 is the number of second electrons that pass the cuts, the total efficiency of the cuts is given by

$$\epsilon = \frac{2N_2}{N_Z + N_2}. \tag{3.5}$$

The efficiency for an individual cut is given by

$$\epsilon_c = \frac{\epsilon}{2}\left(1 - \frac{N_c}{N_Z}\right) + \frac{N_c}{N_Z}, \tag{3.6}$$

where ϵ is given above, and N_c is the number of second electrons that pass cut c. Employing binomial statistics, the statistical errors for ϵ and ϵ_c are found to be

$$\sigma_\epsilon = \sqrt{\frac{\epsilon \cdot (1-\epsilon) \cdot (2-\epsilon)}{N_Z + N_2}} \tag{3.7}$$

and

$$\sigma_{\epsilon_c} = \sqrt{\frac{\epsilon_c \cdot (1-\epsilon_c) \cdot (1 + \epsilon/\epsilon_c - \epsilon)}{N_Z + N_2}} \tag{3.8}$$

respectively.

3.1.5.2 The $Z^0 \rightarrow e^+e^-$ Sample

$Z^0 \rightarrow e^+e^-$ events were selected by requiring the first electron candidate to have $E_T > 20$ GeV, $Iso(R = 0.4)/E_T < 0.1$, and to pass all the selection cuts listed in section 3.1.4. The second cluster must be between the fiducial volume and is required to have $E_T > 20$ GeV, a track of different charge than the first leg with $P_T > 10$ GeV/c, $Had/EM < 0.125$, and $Iso(R = 0.4)/E_T < 0.1$. The invariant mass of the pair must lie within 81 GeV/c^2 and 101 GeV/c^2. 494 events pass these cut. Figure 3.10 is a histogram of the dielectron invariant mass.

3.1.5.3 Results

The efficiency of the high E_T central electron cuts are summarized in table 3.2.

3.1.6 Conversion Electron Removal

Many non-primary high E_T electrons are the result of Dalitz decays of π^0's ($\pi^0 \rightarrow \gamma e^+e^-$) and photons that interact with the material before the CTC to produce an

e^+e^- pair. These electrons are referred to as "conversions". These are real electrons that are fully able to pass the high E_T electron cuts. Photons converting before entering the VTX are called inner conversions. Those that convert in the material between the CTC and VTX are called outer conversions. Outer conversions will not leave a track in the VTX. These can be identified by constructing a parameter called f_{VTX}, which is the number of hits found in the VTX divided by the number of expected hits along a path connecting the event vertex to the electron cluster. Another variable used is m_{ee}, which is the lowest e^+e^- invariant mass formed with any oppositely charged track within 30° in ϕ of the electron candidate track. Electrons are considered conversions if they pass any of the following two cuts:

$$f_{VTX} < 0.2 \tag{3.9}$$

$$m_{ee} < 0.5\ \mathrm{GeV/c^2} \text{ and } R < 50\ \mathrm{cm} \tag{3.10}$$

Here R is the radius of conversion for the two tracks used in calculating m_{ee}. The CTC/VTX material ends at a radius of approximately 35 cm. so any conversion past this is unlikely. Inner conversions leave a track in the VTX, therefore they can only be flagged by cut 3.10.

The efficiency of the f_{VTX} cut is excellent, and is shown in figure 3.11. Less than 0.5% of prompt electrons fail this cut. This distribution was produced from the Z^0 events described in section 3.1.5. The spiky appearance results from f_{VTX} being the ratio of two integers, where each never exceed 24.

The fraction of electrons removed by the m_{ee} and R cuts, f_{prompt}, can be determined by forming the ratio

$$f_{prompt} = \frac{n_{ls}}{n_{ele}}, \tag{3.11}$$

where n_{ele} is the total number of events with $f_{VTX} > 0.2$; n_{ls} is the number of electron candidates that have $f_{VTX} > 0.2$, $m_{ee} < 0.5$ GeV/c^2, and $R < 50$ cm using LIKE-sign tracks.

The efficiency for the mass and radius cut is calculated by taking the ratio of the number of outer conversions ($f_{VTX} < 0.2$) that fail the m_{ee} and R cuts to the total number of outer conversions. There are 1380 events in the inclusive electron data set that are flagged as outer conversions, and of that, 1093 also fail the m_{ee} and R cuts. The efficiency of the mass cut is then $\epsilon_{mass} = \frac{1093}{1380} = 0.792 \pm 0.011$, where the error is statistical only.

The overall conversion detection efficiency, ϵ_{conv}, and the estimate of the fraction of unidentified conversion electrons remaining in the sample, f_{bg}, remains to be determined. To determine these numbers, the following notation is introduced: $n_{f\overline{m}}$ and n_{fm} are the number of electrons that fail cut (3.9) and respectively fail and pass cut (3.10); n_f and $n_{\overline{f}}$ are the number of candidates that respectively fail and pass cut (3.9); n_{prompt} are the number of prompt electrons; and n_{inner} are the number of inner conversions. n_{prompt} and n_{inner} can be solved from the following two equations:

$$n_{f\overline{m}} = f_{prompt} n_{prompt} + \epsilon_{mass} n_{inner} \tag{3.12}$$

$$n_f = n_{prompt} + n_{inner} \tag{3.13}$$

The fraction of unidentified conversion electrons is then given by:

$$f_{bg} = \frac{(1 - \epsilon_{mass}) \times n_{inner}}{n_{fm}} \tag{3.14}$$

The overall conversion detection efficiency is then:

$$\epsilon_{conv} = \frac{n_{\overline{f}} + \epsilon_{mass} n_{inner}}{n_{\overline{f}} + n_{inner}} \tag{3.15}$$

The efficiencies and background rates were determined by selecting electron candidates which pass all the requirements listed in section 3.1.4, as well as having $E_T >$ 20 GeV/c^2 and BE < 2 GeV. The results are displayed in table 3.3

3.2 Inclusive Muon Selection

3.2.1 Inclusive Muon Trigger

The Level–1 muon trigger is a hardware trigger. The trigger requires that hits from a track propagating through the muon chambers form a coincidence in two of the four alternating chamber layers within a time window determined by a P_T threshold. The Level–1 P_T threshold is 6 GeV/c for stubs in the CMU and CMP region, and 10 GeV/c for stubs in the CMX region. The CMU/CMP trigger only fires in areas covered by the CMU alone or areas covered by the overlap of the CMU and CMP (with a few minor exceptions). So in essence, there is no CMP–only Level–1 trigger. The Level–1 CMX trigger has an additional requirement on single trigger-tower thresholds. (i.e., the event must have at least one calorimeter tower with an energy above a minimum value.) The minimum thresholds are 6 GeV for the CEM, 8 GeV in the CHA, PEM, and FEM. The PHA/FHA varied between 12, 15, and 51 GeV during the course of the run. Though the Level–1 CMX PHA/FHA threshold varied, the acceptance for $t\bar{t} \rightarrow \mu$+jets is almost unaffected.

The Level–2 CMU/CMP trigger requires a track found by the Central Fast Tracker, CFT, to match in ϕ with a central muon stub within a 5 degree window. The CFT track is required to have a $P_T > 9.2$ GeV/c. The level–2 CMU/CMP trigger efficiency is $(86.8 \pm 1.9)\%$ [22].

The Level–2 CMX trigger requires a CFT track with $P_T > 9.2$ GeV/c to propagate into the same hemisphere where a Level–1 CMX stub is located. The CFT track must pass through superlayer 8 in the CTC in order for the CFT track to be reconstructed. Due to problems associated with any new detector system, the Level–2 CMX trigger efficiency was only $(54^{+5}_{-6})\%$ [23]. During the run, there were nine different Level–2 CMX triggers. Two of these triggers were pre-requisited on a rate-limited CMX trigger. These two triggers were unusable because no trigger efficiency can be found for them. These two triggers accounted for 24% of the run.

The Level–3 inclusive muon trigger requires a match between muon stub and a CTC track with $P_T > 18$ GeV/c. For muon candidates with stubs in the CMU or CMU/CMP region, the track is required to match the CMU stub to within 5 cm in the ϕ–direction. For CMX candidates, no match in ϕ is required. The efficiency at Level–3 is nearly 100%.

3.2.2 Muon Selection Parameters

Muon identification employs calorimeter information as well as tracking information from the CTC and muon detectors. Described below are the relevant parameters used in muon reconstruction.

3.2.2.1 Fiducial Region

High P_T muon candidates are required to be within the fiducial volume of the muon detector(s). A FORTRAN routine called CMUSWM propagates a track to the radius of the muon chambers and returns the expected distance the track should be from the edge of the appropriate muon chamber in the x and z–views, as well as returning the expected scattering in both views due to multiple scattering and dE/dX effects. (Both of which are small at high P_T.) The track associated with the inclusive muon candidate that has a stub in the CMU, CMP or CMX, must extrapolate no farther than 5 cm from the outside edge of that muon chamber. The extra 5 cm allows for multiple scattering. If the track extrapolates outside this 5 cm limit, the candidate is rejected.

In addition to the above fiducial requirements, CMU–only muons are also required to satisfy the following requirements:

- $|Z| > 9.0$ cm. Where Z is the extrapolated position of the track at the muon chamber radius. (This avoids the 90° crack where there is no CMU coverage.)

- The track must not propagate to within 1.5° in ϕ the ϕ boundary of any wedge. There is no muon coverage here.
- The track must not propagate into the "chimney" tower, which has reduced calorimeter coverage to allow access to the CDF superconducting solenoid.

3.2.2.2 Calorimeter Energy

A muon is a minimum ionizing (MI) particle. In order to suppress non-muon backgrounds, the energy deposited in the tower the muon track passes through must be consistent with that of a MI particle. Testbeam muons deposit on average 0.3 GeV in the EM and 2.0 GeV in the HAD calorimeters [24]. In the lepton+jets analysis, there will be extra energy deposited from other particles propagating into the muon tower, so the maximum EM and HAD calorimeter energy is set to 2 GeV and 6 GeV respectively. Figures 3.12 and 3.13 display the EM and HAD deposited energies for $Z^0 \rightarrow \mu\mu$ events.

Though the muon is a minimum ionizing particle, it should deposit some energy in the calorimeters. In order to guard against bogus track-stub matches, a minimum EM + HAD energy cut of 0.1 GeV is imposed. See figure 3.14 for this distribution.

3.2.2.3 Momentum

The track associated with the muon stub is the CTC track that has the best P_T and spatial match to the muon stub. The initial momentum measurement is then recalculated by "beam constraining" the track as described in section 3.1.3.3.

3.2.2.4 Impact Parameter

The impact parameter is defined as the minimum radial distance between the track and beam line. Cosmic rays and hadron decays in flight usually have larger impact parameters than promptly produced particles. Figure 3.16 is a histogram of this distribution.

3.2.2.5 Vertex-Track Separation

The difference along the z–axis between the track vertex and primary vertex found by the VTX should be under a few cm. Cosmic rays can cross the beam line at any z position, so this variable can be used to further reduce cosmics and junk tracks. See figure 3.16.

3.2.2.6 Track Matching

The azimuthal, ϕ, separation between the muon stub and track extrapolated to the muon chamber radius can be measured in all three muon detectors. Multiple scattering of muons in the detector material produces a one sigma spread of 1 cm for muons with P_T = 15 GeV/c. With such a small spread, and the high tracking accuracy of the CTC, a rather tight cut can be made on track-stub matching. Distributions of the azimuthal matching of muons from Z^0 decays that propagate through the CMU, CMP, and CMX are plotted in figures 3.17 through 3.19 respectively.

In addition to stub and track matching in the ϕ view, the CMU and CMX are capable of matching in the z view as well. Due to the better resolution of the CTC in the azimuthal plane, coupled with the somewhat poor z resolution of the muon chambers, no cut is made on this variable for high P_T muons.

3.2.2.7 Muon Isolation

The definition of muon border energy (BE) differs slightly from the electron border energy definition (section 3.1.3.12) in that the muon will only penetrate one tower while the electron shower may encompass several towers. A plot of this distribution is made in figure 3.20.

As in the case of electrons, the muon isolation is defined as $Iso(R) = E_T^R - E_T^{tower}$ where E_T^R is the transverse energy in a cone of radius R measured about the muon track, and E_T^{tower} is the energy in the tower penetrated by the muon track.

3.2.3 Muon Identification Cuts

Listed below is the summary of the quality cuts imposed on muon candidates:

1. Track must extrapolate into the fiducial region(s).
2. Hadronic energy in muon tower < 6 GeV
3. Electromagnetic energy in muon tower < 2 GeV
4. Hadronic + Electromagnetic energy in muon tower > 0.1 GeV
5. If CMU stub present, $\Delta X(CMU) < 2$ cm
6. If CMP stub present, $\Delta X(CMP) < 5$ cm
7. If CMX stub present, $\Delta X(CMX) < 5$ cm
8. $|Z_{track} - Z_{vertex}| < 5$ cm
9. $d0 < 0.2$ cm
10. $|Z_{vertex}| < 60$ cm

3.2.4 Muon Selection Efficiency

The efficiency of the muon cuts is determined in a simular fashion as calculated for electrons in section 3.1.5.

3.2.4.1 The $Z^0 \rightarrow \mu^+\mu^-$ Sample

$Z^0 \rightarrow \mu^+\mu^-$ events were selected by requiring the first muon candidate to pass all the cuts listed in section 3.2.3. In addition to these cuts, the first leg was required to have $P_T > 20$ GeV/c, $BE < 2$ GeV and $Iso(R = 0.4)/P_T < 0.1$. The second oppositely charged leg was required to have $P_T > 20$ GeV/c, $d0 < 0.2$ cm, and propagate into the fiducial region. If the invariant mass of the two tracks lies between 75 GeV/c^2 and 105 GeV/c^2 the event is kept. A plot of this distribution is shown in figure 3.21.

3.2.4.2 Results

The efficiencies of the high P_T muon cuts are summarized in table 3.4 [22].

3.3 Jets

Four quark jets are expected in $t\bar{t}$ events when one of the top quarks decays hadronically and the other decays semileptonically. Requiring the presence of several jets will significantly reduce backgrounds from W events which have less associated jet activity. In this section the jet clustering algorithm will be discussed as well as a technique to correct the energy of jets that fall into eta cracks and are mismeasured. A description of jet parameters will also be given.

3.3.1 Jet Clustering

Jets are detected as clusters of energy in the calorimeter using a fixed cone algorithm. The algorithm starts by flagging all towers with $E_T = E_T^{EM} + E_T^{HAD} > 1$ GeV. These towers are called seed towers. If seed towers are adjacent to another, either by side or corner, they are combined into a precluster. These preclusters are formed in such a fashion that tower E_T always decreases from the highest E_T tower to towers on the edge of the precluster. Since jets tend to assume a "circular" shape in (η, ϕ) space with "radius" $R = \sqrt{\eta^2 + \phi^2}$, clusters are then formed from preclusters by summing all towers within a cone of radius R in η, ϕ space centered about the highest E_T tower.

(In this analysis, $R = 0.4$.) The E_T weighted average is calculated, and the center of the cone is repositioned on this new centroid. The clustering algorithm is performed again centered around this new (η, ϕ) position. This procedure is continued across the whole calorimeter until no towers are lost or gained from any cluster.

If a smaller cluster is completely contained in a larger cluster, the smaller one is included in the larger cluster. Two clusters that partially overlap may be merged if the E_T in the overlap region divided by the E_T of the lesser E_T cluster is greater than 0.75. Otherwise, the towers in the overlap region are partitioned according to the closeness of each tower to the centroid of each of the clusters. This procedure is continued until a stable configuration is achieved.

3.3.2 Jet Parameters

Each tower in the calorimeter registers an electromagnetic or hadronic energy, E^i_{em} and E^i_{had}, at an azimuthal angle ϕ^i. Each EM and HAD tower has an associated polar angle, θ^i_{em} and θ^i_{had}, formed between the center of each EM and HAD tower and the event vertex. A momentum vector for each cluster is formed, as well the energy for that cluster using the following definitions:

$$P_x = \sum_i (E^i_{em} \sin\theta^i_{em} + E^i_{had} \sin\theta^i_{had}) \cos\phi^i \tag{3.16}$$

$$P_y = \sum_i (E^i_{em} \sin\theta^i_{em} + E^i_{had} \sin\theta^i_{had}) \sin\phi^i \tag{3.17}$$

$$P_z = \sum_i (E^i_{em} \cos\theta^i_{em} + E^i_{had} \cos\theta^i_{had}) \tag{3.18}$$

$$E = \sum_i (E^i_{em} + E^i_{had}) \tag{3.19}$$

The sum runs over all the towers in a cluster. The cluster "momentum" is approximately equal to the energy in the cone from the original parton. The above definitions are then used to define the jet momentum and transverse momentum:

$$P_T = \sqrt{P_x^2 + P_y^2} \tag{3.20}$$

$$P = \sqrt{P_x^2 + P_y^2 + P_z^2} \tag{3.21}$$

Finally, the E_T is defined thusly:

$$E_T \overset{\text{def}}{=} E\frac{P_T}{P}. \tag{3.22}$$

The η of the jet (or anything else) was defined in section 2.2. There is an associated variable called detector eta, η_{det}, where the rapidity is calculated at $z = 0$ cm, not at the event vertex.

3.3.3 Relative Jet Correction

Jets may be mismeasured in the calorimeter due to differences in gain between various detector components, non-linearalities in the calorimetry or because they fall into the various eta cracks. Some correction must be constructed to remove these effects. This correction is called the relative jet correction. (There are other corrections that are applied to jets after the relative correction to convert these energies back to the energy of the parton that originated the jet. These will be discussed after the Monte Carlo data sets are introduced.)

The goal of the relative jet correction is to convert a jet at any η_{det} back to an equivalent jet in the region $0.2 < |\eta_{det}| < 0.7$. This central region is far away from any cracks, is well understood, and uniform. The method used to construct this correction is called jet balancing, and is described below.

In a perfect detector, QCD produced di–jet events will balance back-to-back in P_T. (Effects due a third softer jet are neglected here.) Using this information, a procedure can be developed which will balance the P_T of a jet in the above mentioned central region with the P_T of any jet outside this region. The di–jets used in the balancing are taken from four single jet triggers which go by the names JET20, JET50, JET70, JET100. A JET20 trigger, for example, has one or more jets with P_T above 20 GeV/c.

There are no overlaps between these jet triggers. In order for an event to be considered a di–jet event, it must pass the following cuts:

- At least one jet in the region $0.2 < |\eta_{det}| < 0.7$
- Two jets with $P_T > 15$ GeV/c
- No other jets with $P_T > 15$ GeV/c
- One primary vertex
- $|Z_{vertex}| < 60$ cm
- $\Delta\phi_{jet1-jet2} > 2.7$ radians
- Event passes COSFLT (a cosmic ray filter)
- Calorimeter data considered good according to BADRUN.

In order to avoid any trigger bias toward jets that fall into cracks, a $\sum P_T$ cut is used that is twice the trigger P_T plus 10 GeV/c. Table 3.1 lists the $\sum P_T$ cut for each of the four jet triggers and other information for three different cone sizes. The variable $\sum P_T$ is simply the sum of the P_T of the two di–jets.

Now the method used to produce the correction will be described, but first a few definitions are required: In the di–jet sample, the jet that resides in the region $0.2 < |\eta_{det}| < 0.7$ is called the "trigger" jet. The second jet, termed the "probe" jet, can be at any η_{det}. If both are in the trigger jet region, the trigger and probe designations are assigned randomly. $\vec{\not{E}}_{\rm T}$ is the missing E_T vector, which is simply the negative of the vector sum of the transverse energies in all the calorimeter towers. The missing E_T projection fraction (MPF) is formed from these quantities and is defined as:

$$MPF = \frac{2 \cdot \vec{\not{E}}_{\rm T} \cdot \hat{p}_T^{probe}}{P_T^{trigger} + P_T^{probe}}, \tag{3.23}$$

where the factor 2 is the result of dividing by the average P_T. This is a measure of jet imbalance. Utilizing the $\not{E}_{\rm T}$ summed over all towers makes the correction less dependent on soft third jets. The $\not{E}_{\rm T}$ is projected along the probe jet axis to minimize

Table 3.1

Sum P_T ranges for each trigger used in relative jet scale.

Trigger	$\sum P_T$ (GeV)	$\int \mathcal{L}dt$ (pb^{-1})	Number of events that pass cuts		
			$\Delta R = 0.4$	$\Delta R = 0.7$	$\Delta R = 1.0$
JET20	50 → 110	18.21	12161	18604	23098
JET50	110 → 150	15.26	5433	7435	8957
JET70	150 → 210	17.85	4253	5793	7058
JET100	> 210	18.21	4330	5874	7214

effects of any K_t kick due to third softer jets which tend to be perpendicular to the probe-trigger axis. In other words

$$\vec{\not{E}}_T \cdot \hat{p}_T^{probe} = P_T^{trigger} - P_T^{probe}. \tag{3.24}$$

This equation can be substituted into equation 3.23 which yields

$$MPF = \frac{2 \cdot (P_T^{trigger} - P_T^{probe})}{P_T^{trigger} + P_T^{probe}}. \tag{3.25}$$

Now define

$$\beta = \frac{P_T^{trigger}}{P_T^{probe}}. \tag{3.26}$$

Using β, and the definition of MPF from equation 3.25, we finally obtain

$$\beta = \frac{2 + MPF}{2 - MPF} \tag{3.27}$$

This quantity β is constructed such that $P_T^{probe} \times \beta = P_T^{trigger}$ or β transforms a jet at any η_{det} back to an equivalent central jet, which is the goal of this exercise. β

needs to be a function of η_{det} and P_T. This is done by fitting β to a continuous curve and parameterizing the P_T dependence. This is then used to produce a cubic spline, so given a P_T and η_{det}, β can be interpolated.

Figure 3.22 displays the spline fit for a jet clustering cone size of $R = 0.4$ for each of the four jet triggers. JET20 is at the bottom, JET100 at the top. Fit Pt is twice the average P_T. Relative scale is the value of the relative jet correction at a given η_{det}. The correction rises above one at approximately $|\eta_{det}| = 0.0$, 1.1, and 2.4. These positions correspond to cracks where the jet energy is undermeasured due to lack of calorimeter coverage. The JET20 and JET50 relative correction extends out to $|\eta_{det}|$ of 3.5, but is averaged from 2.55 to 3.5 due to the lack of statistics at high eta. The JET70 and JET100 only extend to $|\eta_{det}| = 2.0$, since almost no dijet events exist beyond this η_{det}. The errors in this plot are statistical only.

This exercise was repeated for Monte Carlo generated di–jet events passed through the QFL detector simulation package (section 4.5.1) in order to determine the relative correction for MC simulated jets.

3.4 Raw Missing Transverse Energy

The raw. missing transverse energy, $\vec{\not{E}}_T^{\,raw}$, is defined to be the negative of the vector sum of the transverse energy in all the calorimeter towers with $|\eta| < 3.5$. The z–vertex used in the calculation is the primary vertex z–position as found by the VTX. The raw $\not{E}_T$ can be written as:

$$\vec{\not{E}}_T^{\,raw} = - \sum_{|\eta|<3.5} \vec{E}_T^{tower}. \tag{3.28}$$

The eta range is limited because the the final focusing magnets of the tevatron obscure parts of the FHA, and ultimately by the beam pipe. For a tower to be included in the above sum, it must exceed a transverse energy threshold. The threshold is 0.1 GeV in the central calorimeter, 0.3 GeV in the plug EM, 0.5 GeV in the plug Had calorimeter, 0.5 GeV in the forward EM calorimeter, and 0.8 GeV in the FHA.

This raw missing E_T calculation can be improved to yield a better estimate of the true $\not{E}_{\mathrm{T}}$. For electron+jets events, the energy of the electron candidate is corrected as described in section 3.1.3. The $\not{E}_{\mathrm{T}}$ is then modified as follows:

$$\vec{\not{E}}_{\mathrm{T}}^{\,e} = \vec{\not{E}}_{\mathrm{T}}^{\,raw} + (\vec{E}_T^{e,raw} - \vec{E}_T^{e,cor}). \tag{3.29}$$

Where $\not{E}_{\mathrm{T}}^{\,e}$ is the corrected missing transverse energy, $E_T^{e,raw}$ is the uncorrected electron transverse energy, and $E_T^{e,cor}$ is the corrected electron E_T.

In events where a muon(s) is tagged, the $\not{E}_{\mathrm{T}}$ can be incorrect by a considerable amount since muons are minimum ionizing particles and leave little energy in the calorimeter. In this case, the $\not{E}_{\mathrm{T}}$ is modified accordingly:

$$\vec{\not{E}}_{\mathrm{T}}^{\,\mu} = \vec{\not{E}}_{\mathrm{T}}^{\,raw} + \sum(\vec{E}_T^{\mu} - \vec{p}_T^{\mu}), \tag{3.30}$$

where the sum is over all the muons in the event; $\vec{P}_T^{\mu}$ is the beam constrained muon transverse momentum. In the case of high P_T isolated muons, $\vec{E}_T^{\mu}$ is defined to be the sum of the EM and HAD energy in the calorimeter tower the muon passes through. For non-isolated muons found with the soft muon tagging algorithm (section 5.1), $\vec{E}_T^{\mu}$ is defined to be $2.0 \times \cos\phi$ GeV in the x-direction, and $2.0 \times \sin\phi$ GeV in the y-direction, where the 2.0 represents 2.0 GeV worth of E_T a muon typically deposits in the calorimeter.

There are other corrections that can be applied to $\not{E}_{\mathrm{T}}$, but a description of them will be postponed until the Monte Carlo data sets are introduced in chapter 4.

Table 3.2

Central electron cut efficiencies from $Z^0 \rightarrow e^+e^-$. All electrons are isolated and located in the fiducial region of the calorimeter.

Cut	N_c	Efficiency (%)
$Had/EM < 0.05$	477	98.0 ± 0.5
$E/P < 1.5$	421	91.3 ± 1.0
$\|Z_{VTX} - Z_{CTC}\| < 5.0$ cm	492	99.8 ± 0.2
$d0 < 0.2$ cm	479	98.2 ± 0.5
$L_{shr} < 0.2$	478	98.1 ± 0.5
$\chi^2_{strip} < 10$	456	95.5 ± 0.7
$\|X\| < 1.5$ cm	447	94.4 ± 0.8
$\|Z\| < 3.0$ cm	478	98.1 ± 0.5
All Cuts	349	82.8 ± 1.6

Table 3.3

Summary of conversion analysis for inclusive electrons.

Number of electron candidates:	$n_e = 23731$
with $f_{VTX} > 0.2$:	$n_f = 22351$
with $f_{VTX} > 0.2$ and $m_{ee} > 0.5$ GeV:	$n_{fm} = 17965$
with $f_{VTX} > 0.2$ and $m_{ee} < 0.5$ GeV and $R < 50$ cm:	$n_{f\overline{m}} = 4386$
with $f_{VTX} < 0.2$:	$n_{\overline{f}} = 1380$
Fraction of prompt electrons removed:	$f_{prompt} = 0.05 \pm 0.03$
Efficiency of mass cut:	$\epsilon_{mass} = 0.79 \pm 0.01$
Number of prompt electrons in sample	$n_{prompt} = 16867 \pm 395$
Number of inner conversions in sample:	$n_{inner} = 5484 \pm 365$
Conversion as fraction of final sample:	$f_{bg} = 0.06 \pm 0.02$
Conversion removal efficiency:	$\epsilon_{conv} = 0.83 \pm 0.04$

Table 3.4

Single cut efficiencies for high P_T muons.

Cut	Efficiency (%)
HAD < 6 GeV	$98.9^{+0.4}_{-0.5}$
EM < 2 GeV	$96.9^{+0.6}_{-0.7}$
BE < 2 GeV	$95.7^{+0.8}_{-0.9}$
Isolation < 0.1	$98.1^{+0.5}_{-0.6}$
ΔX(CMU) < 2 cm	$97.3^{+0.7}_{-0.9}$
ΔX(CMP) < 5 cm	$99.8^{+0.2}_{-0.5}$
ΔX(CMX) < 5 cm	$98.0^{+1.0}_{-1.6}$

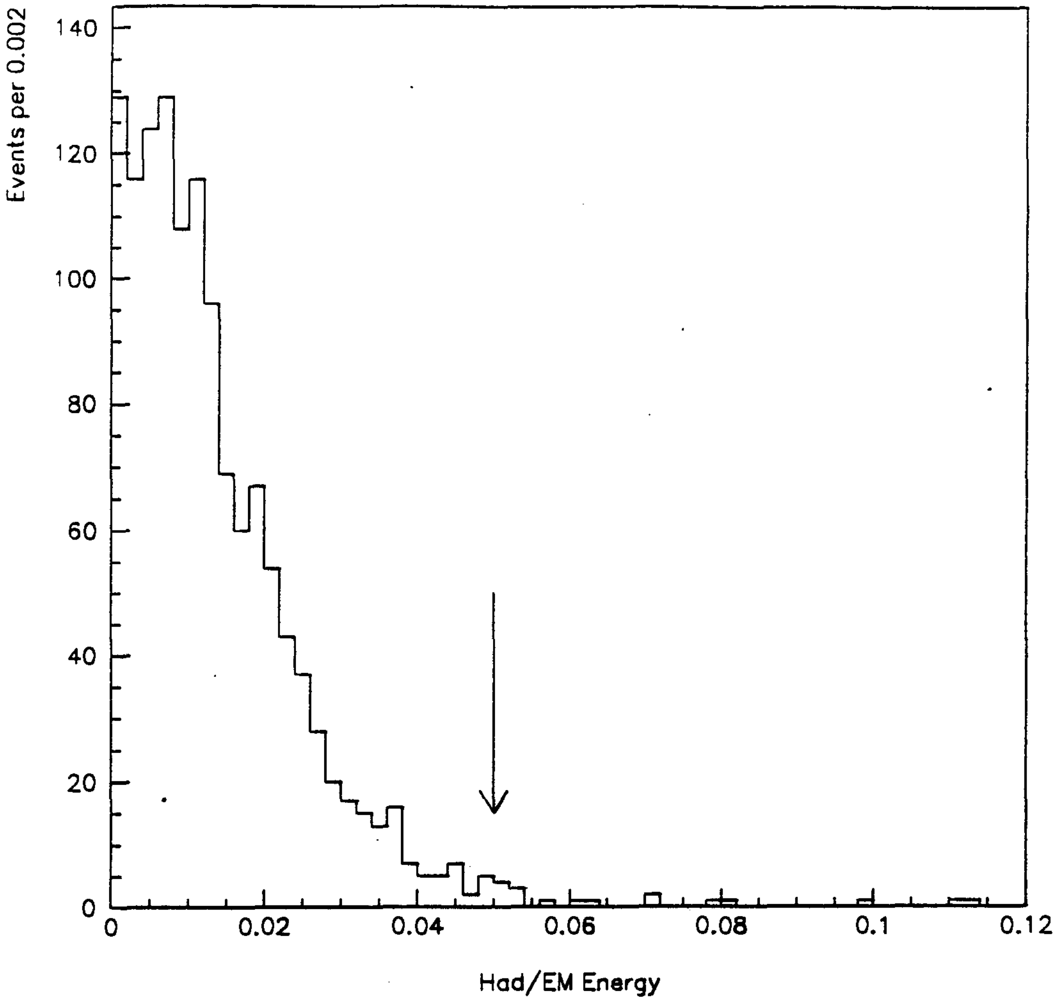

Figure 3.1

The *Had/EM* distribution for $Z^0 \rightarrow e^+e^-$ events.

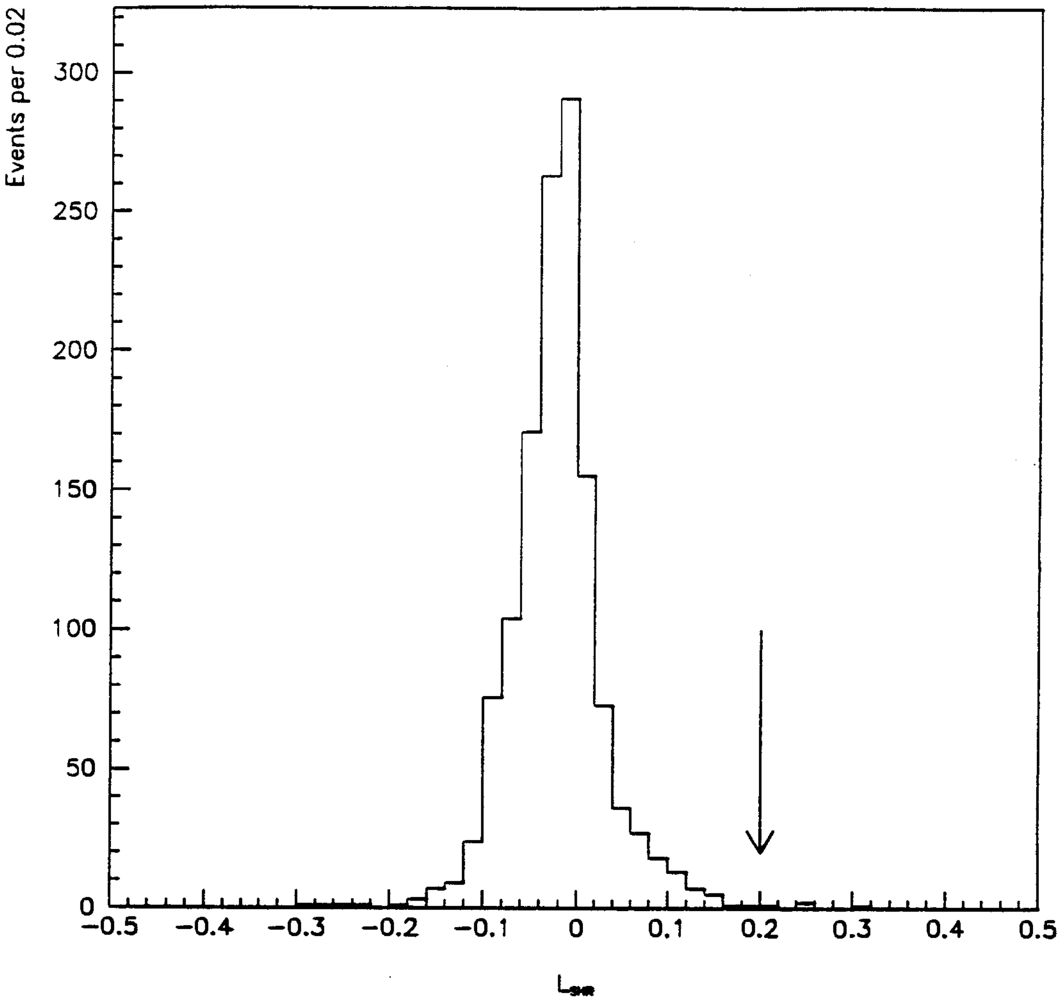

Figure 3.2

The L_{shr} distribution for $Z^0 \rightarrow e^+e^-$ events.

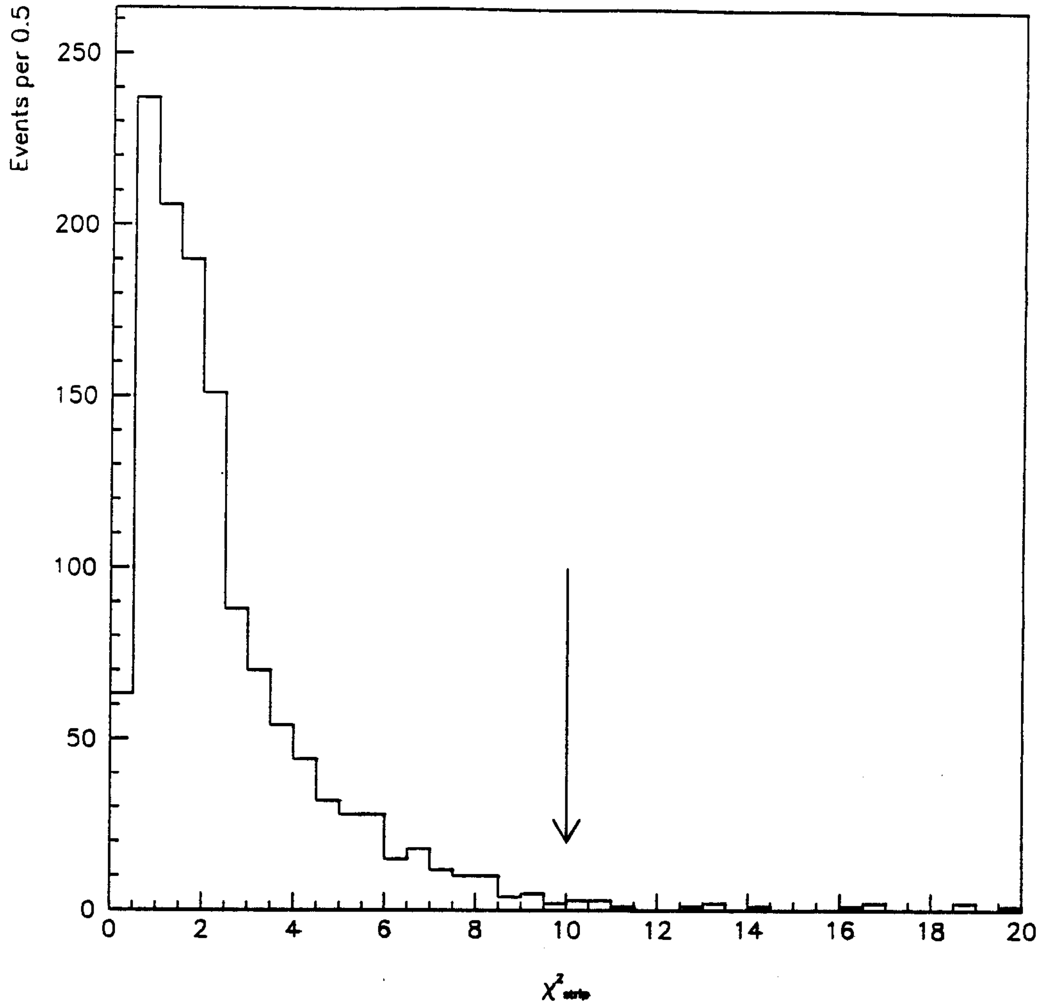

Figure 3.3

The χ^2_z distribution for $Z^0 \rightarrow e^+e^-$ events.

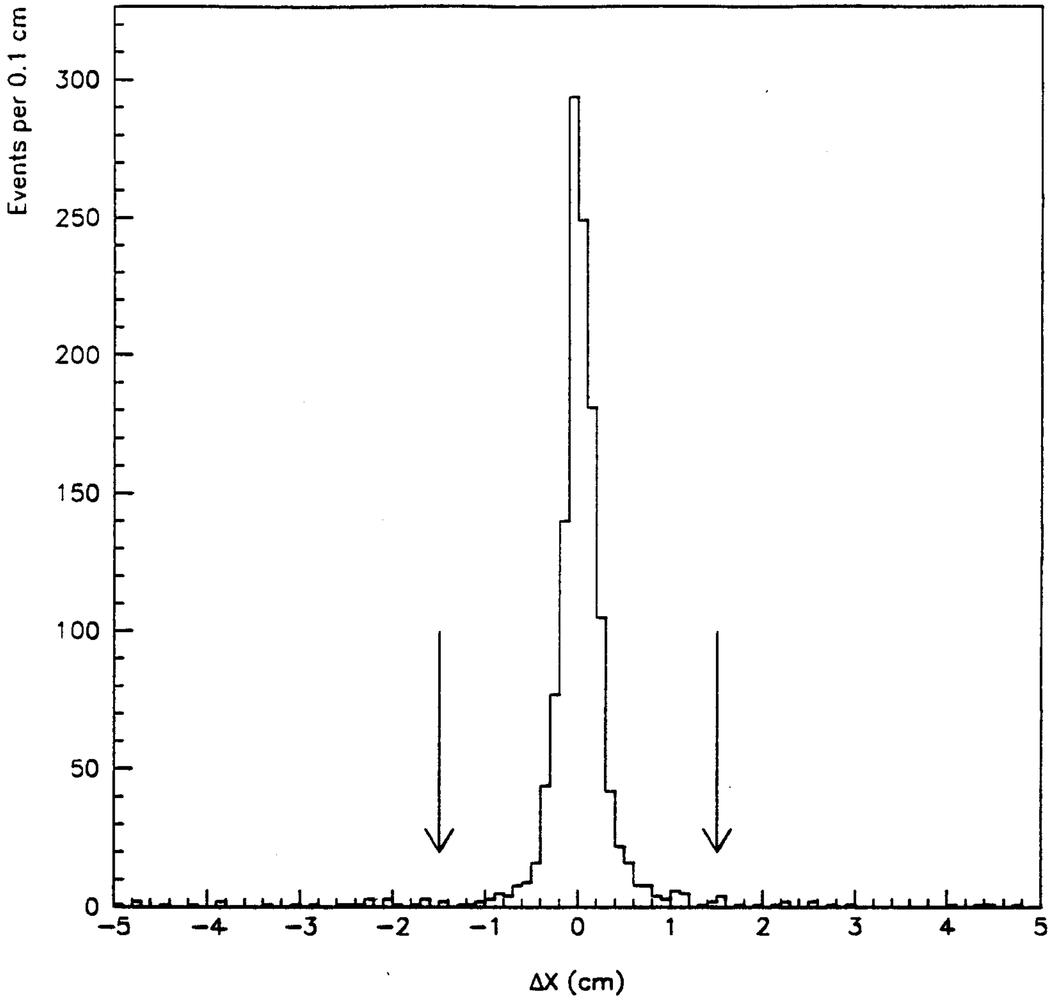

Figure 3.4

The ΔX distribution for $Z^0 \rightarrow e^+e^-$ events.

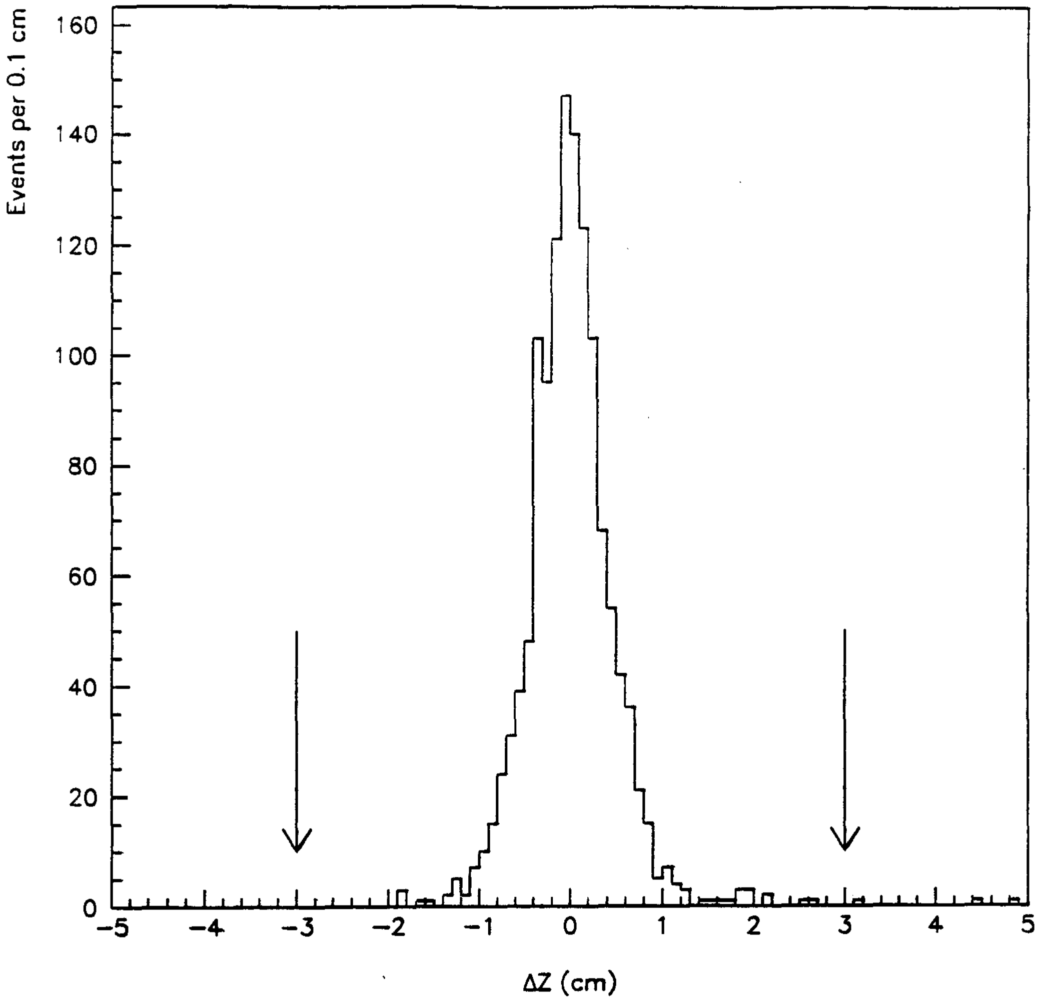

Figure 3.5

The ΔZ distribution for $Z^0 \rightarrow e^+e^-$ events.

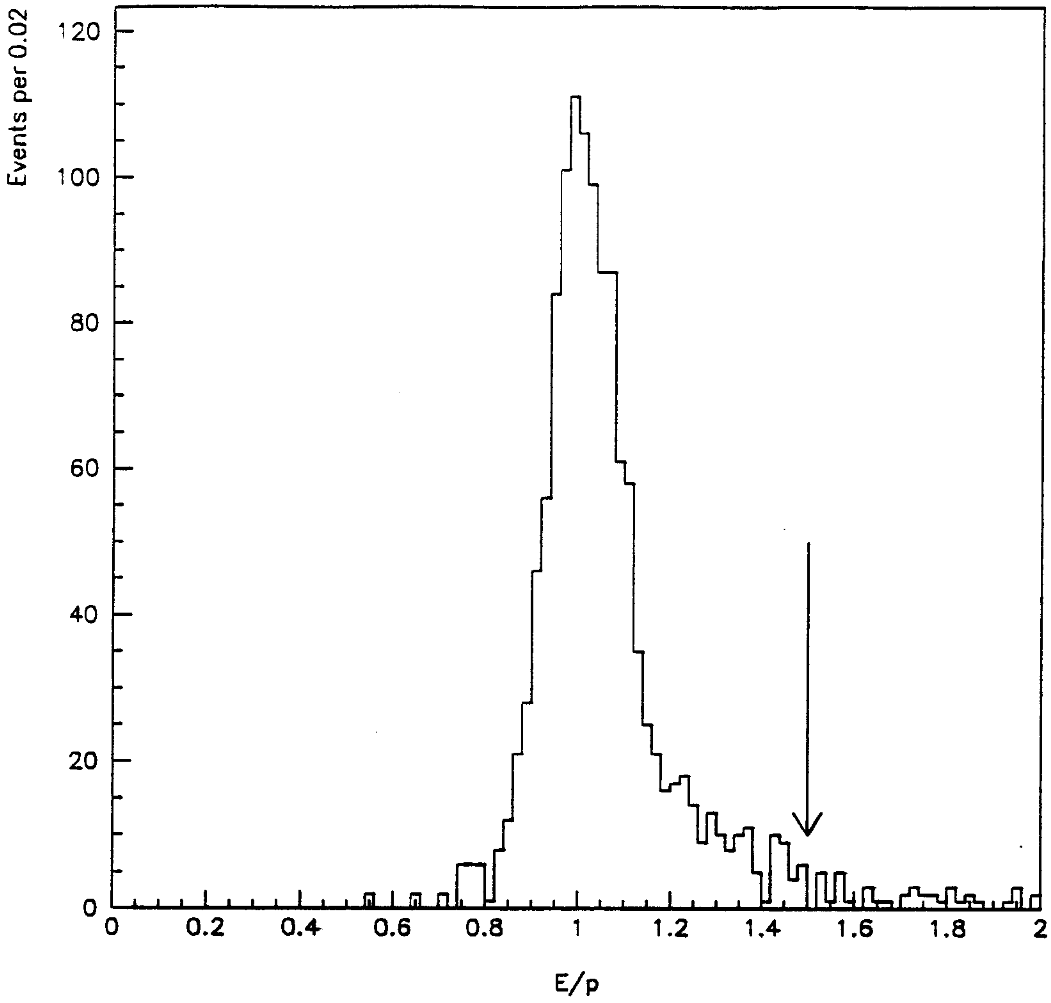

Figure 3.6

The E/P distribution for $Z^0 \rightarrow e^+e^-$ events.

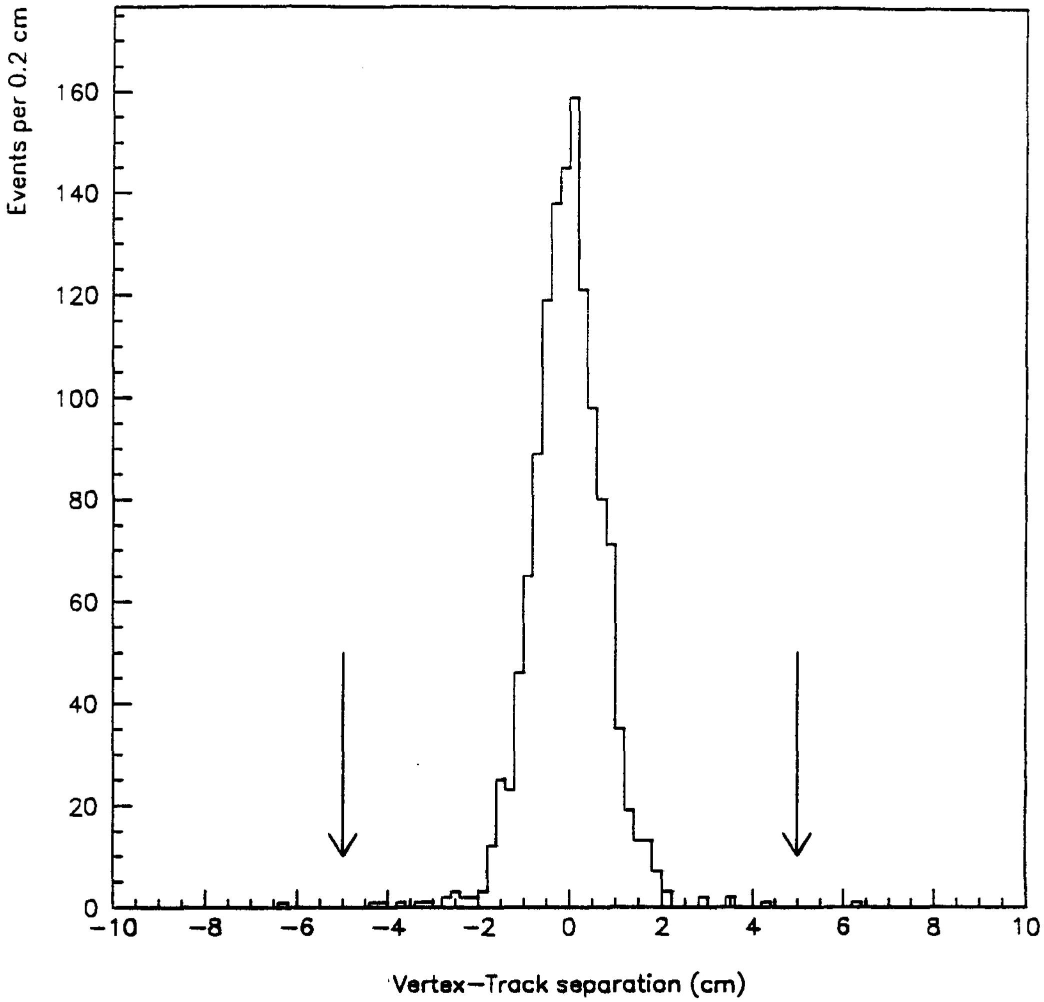

Figure 3.7

Vertex-track z separation for $Z^0 \rightarrow e^+e^-$ events.

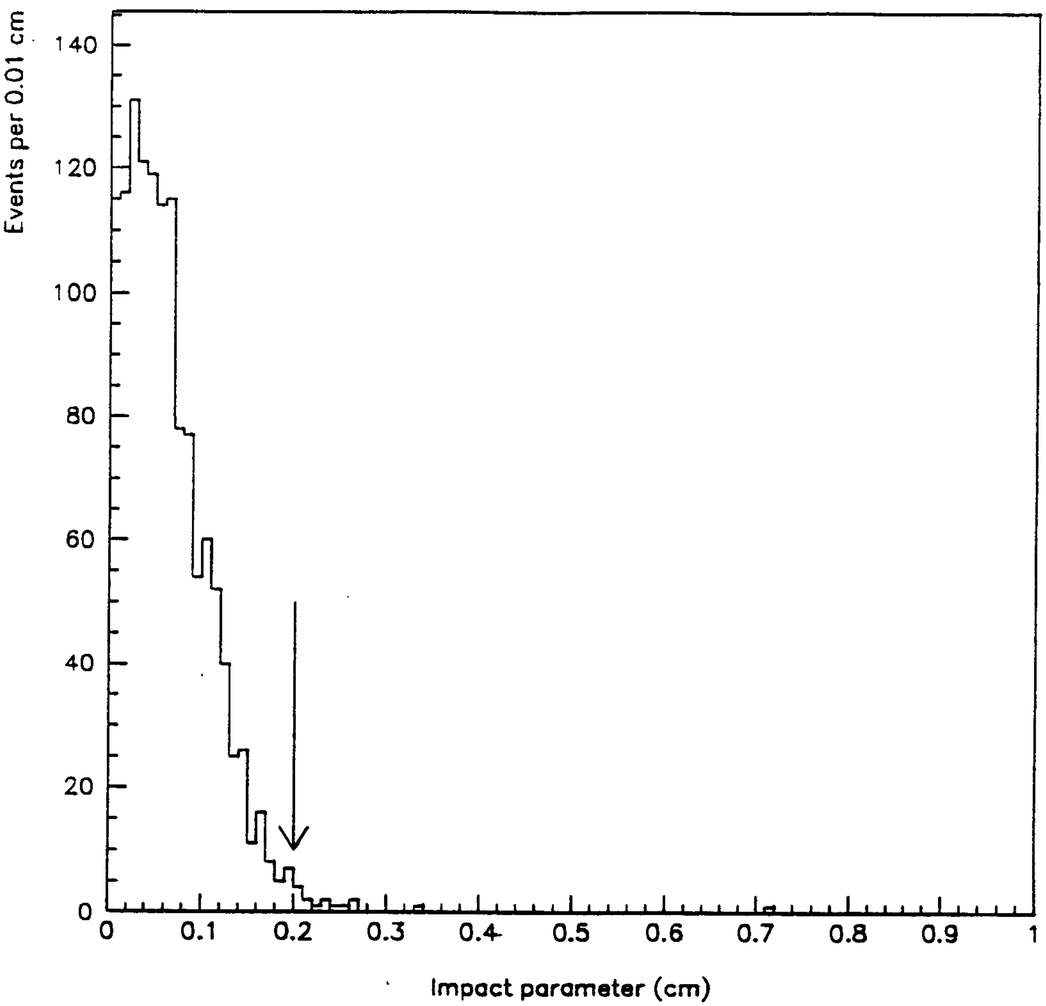

Figure 3.8

Impact parameter for $Z^0 \rightarrow e^+e^-$ events.

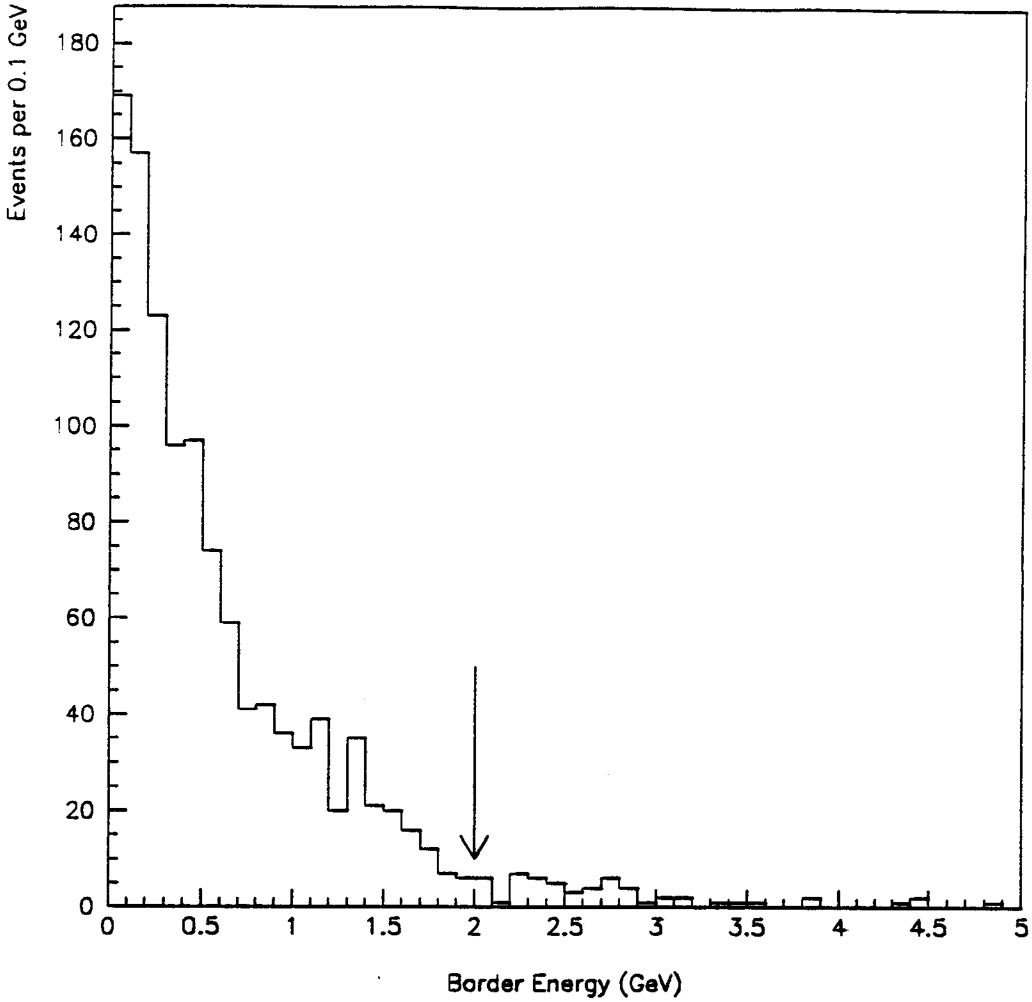

Figure 3.9

Border Energy $Z^0 \rightarrow e^+e^-$ events.

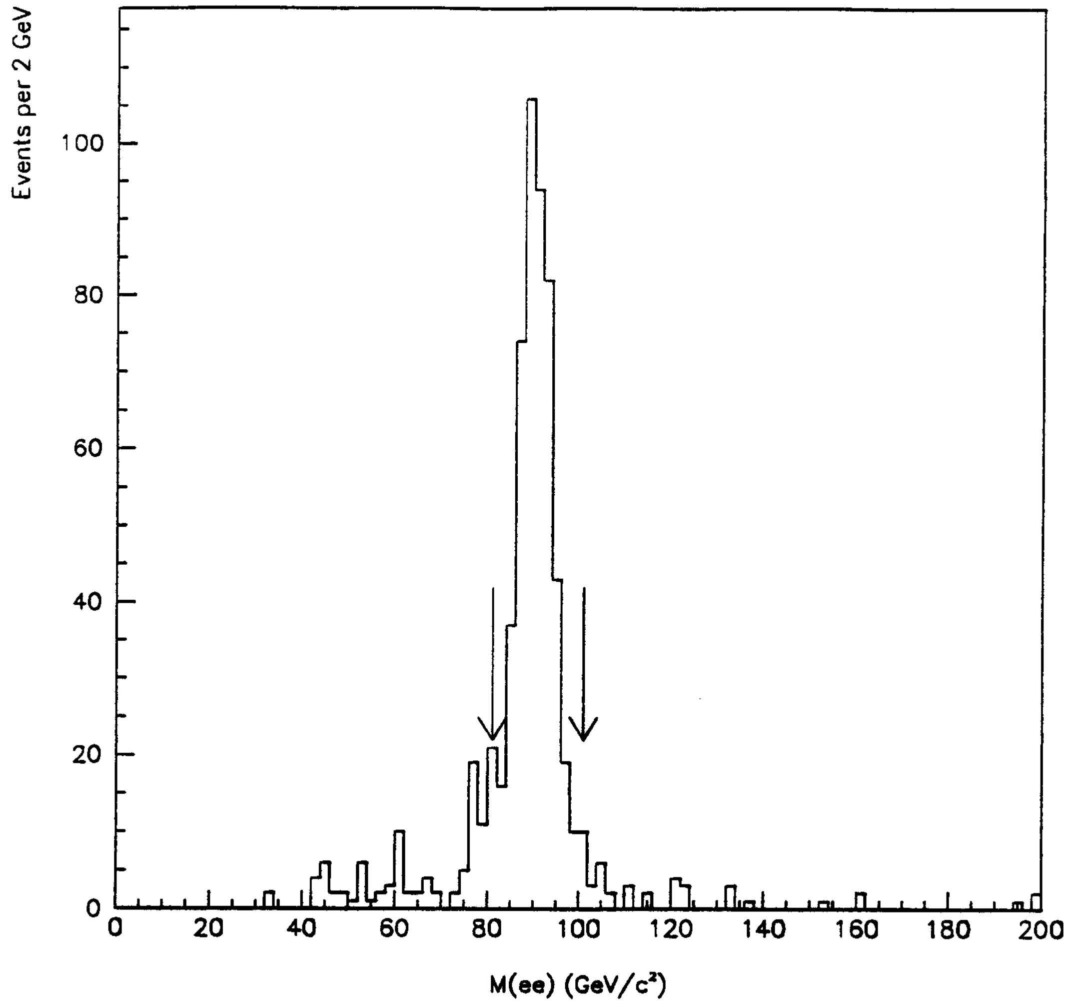

Figure 3.10

The invariant mass of the dielectron sample.

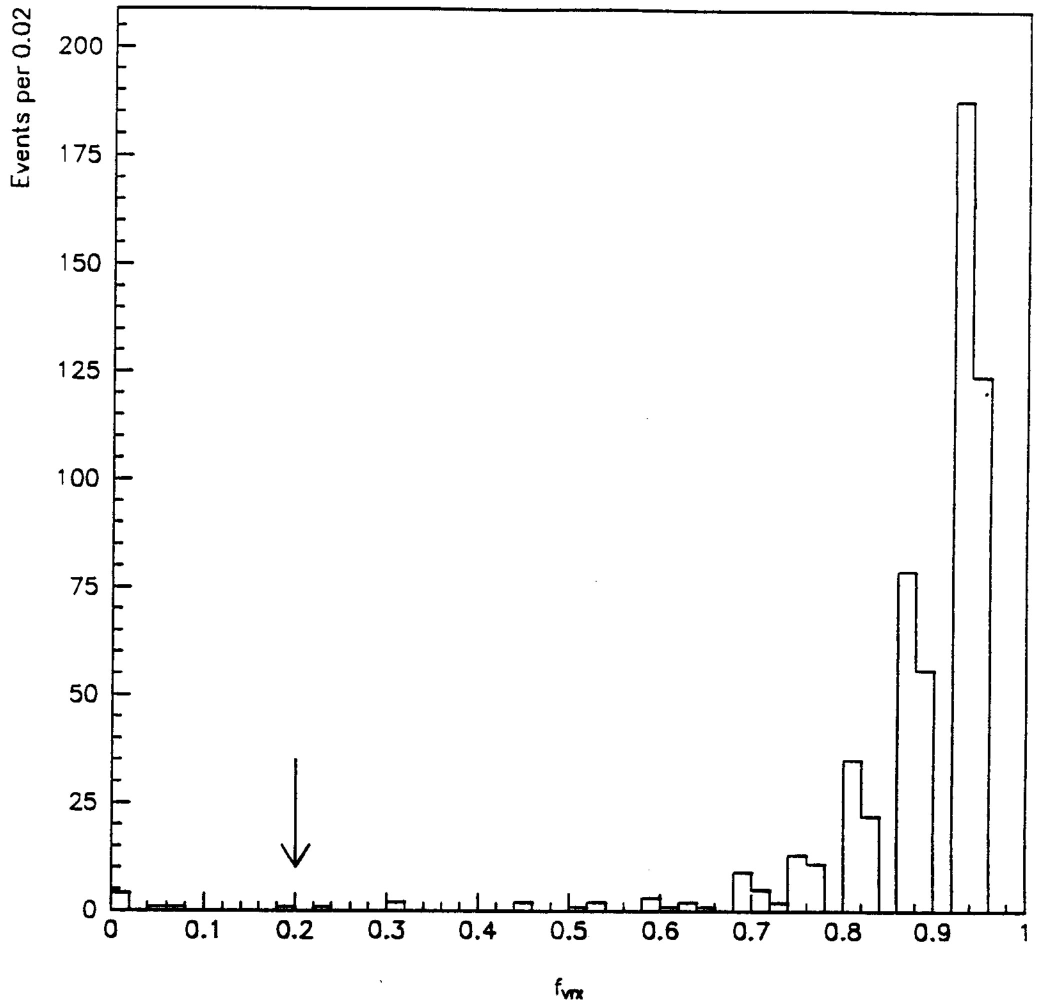

Figure 3.11

The fraction of expected hits observed in the VTX.

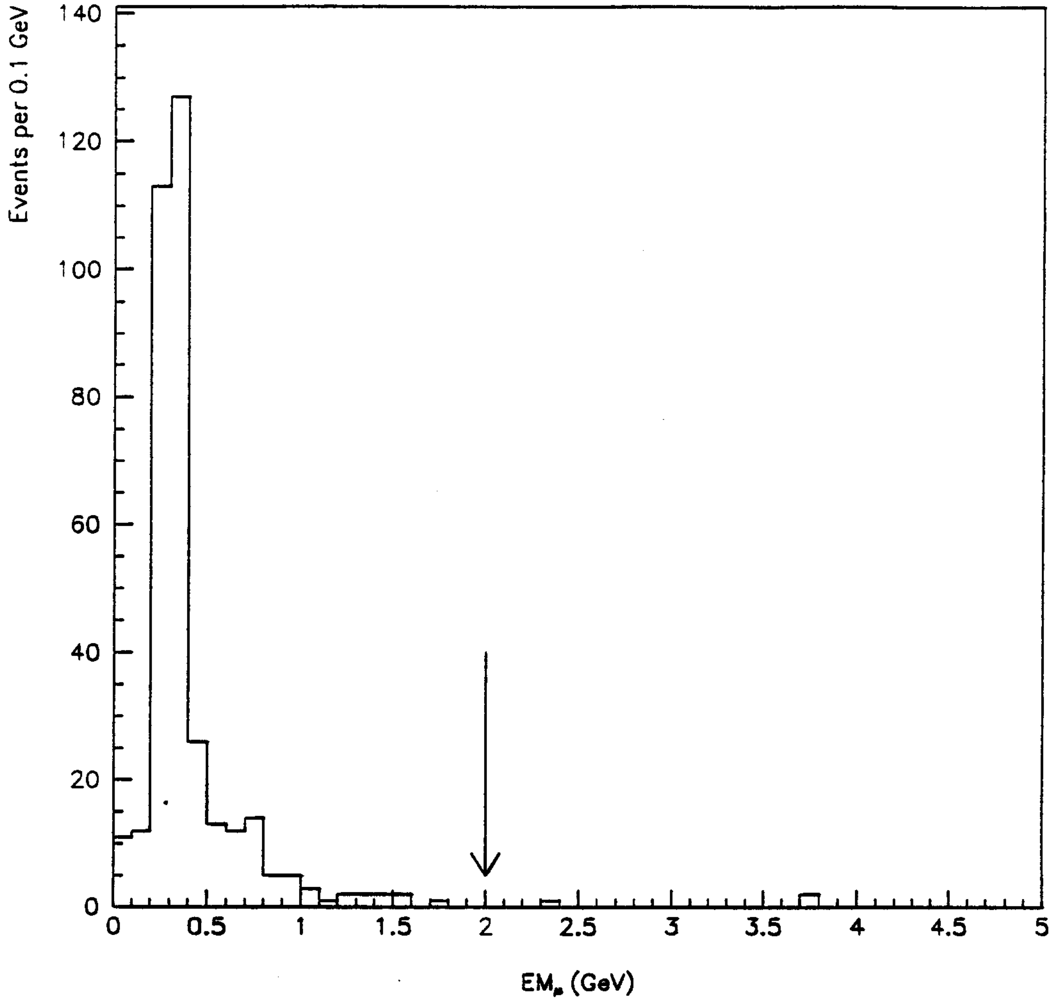

Figure 3.12

The distribution of energy deposited in the CEM by muons from $Z^0 \rightarrow \mu\mu$ events.

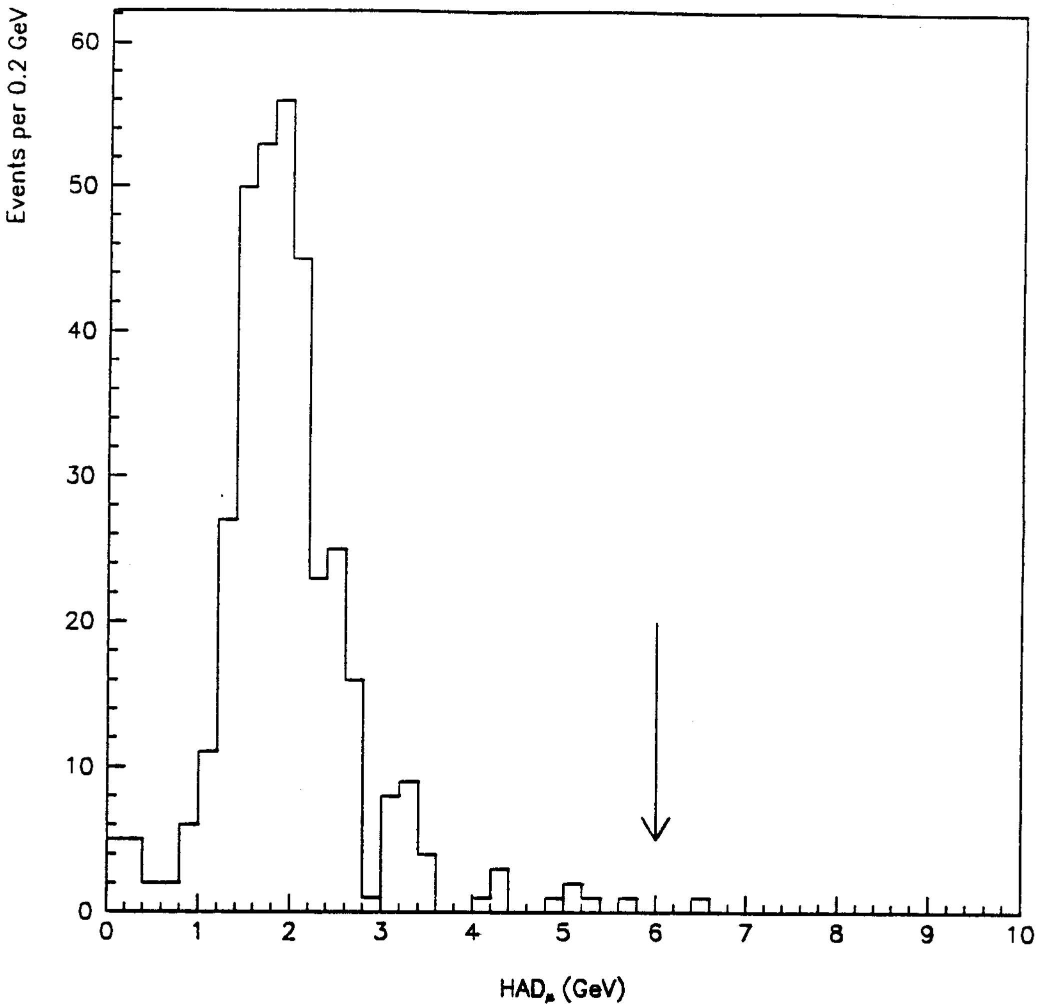

Figure 3.13

The distribution of energy deposited in the CHA by muons. The muons are from $Z^0 \rightarrow \mu\mu$ events.

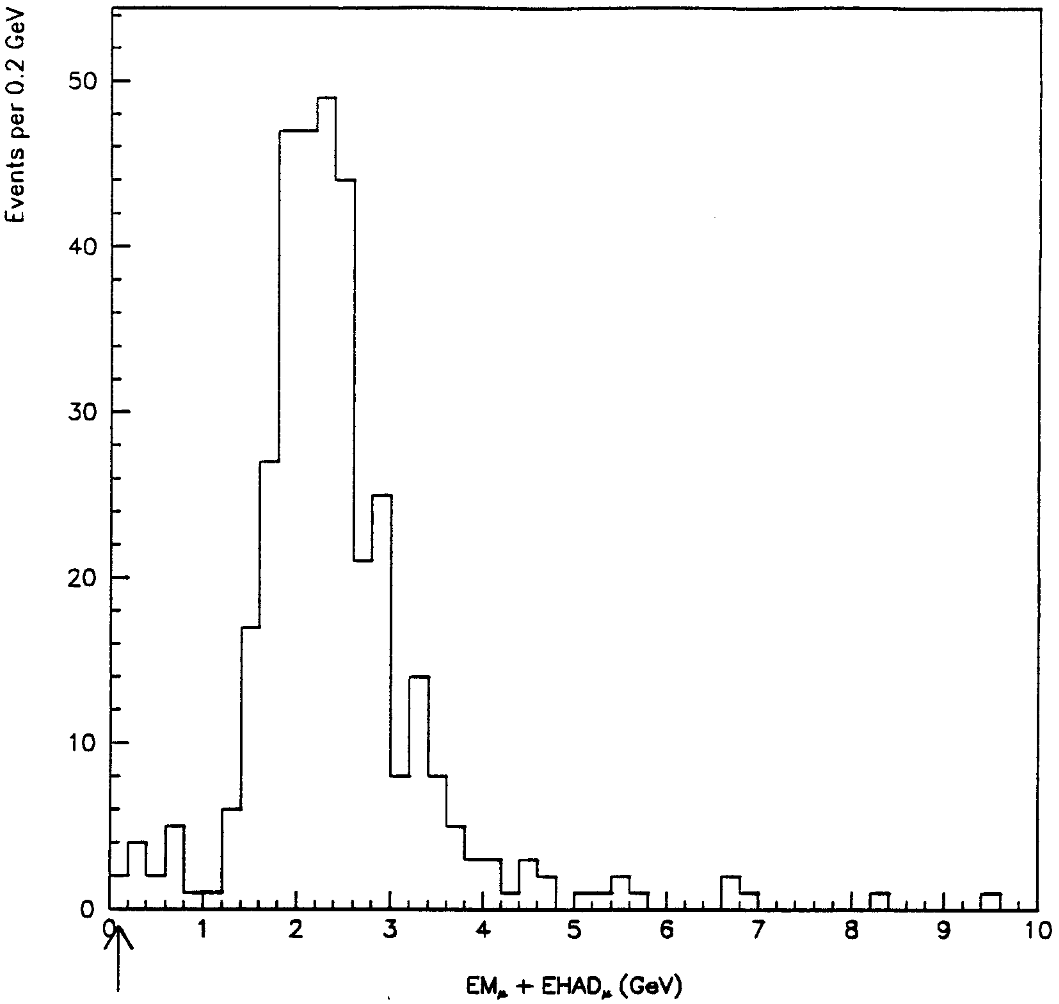

Figure 3.14

The distribution of energy deposited in the CEM and CHA by muons. The muons are from $Z^0 \rightarrow \mu\mu$ events.

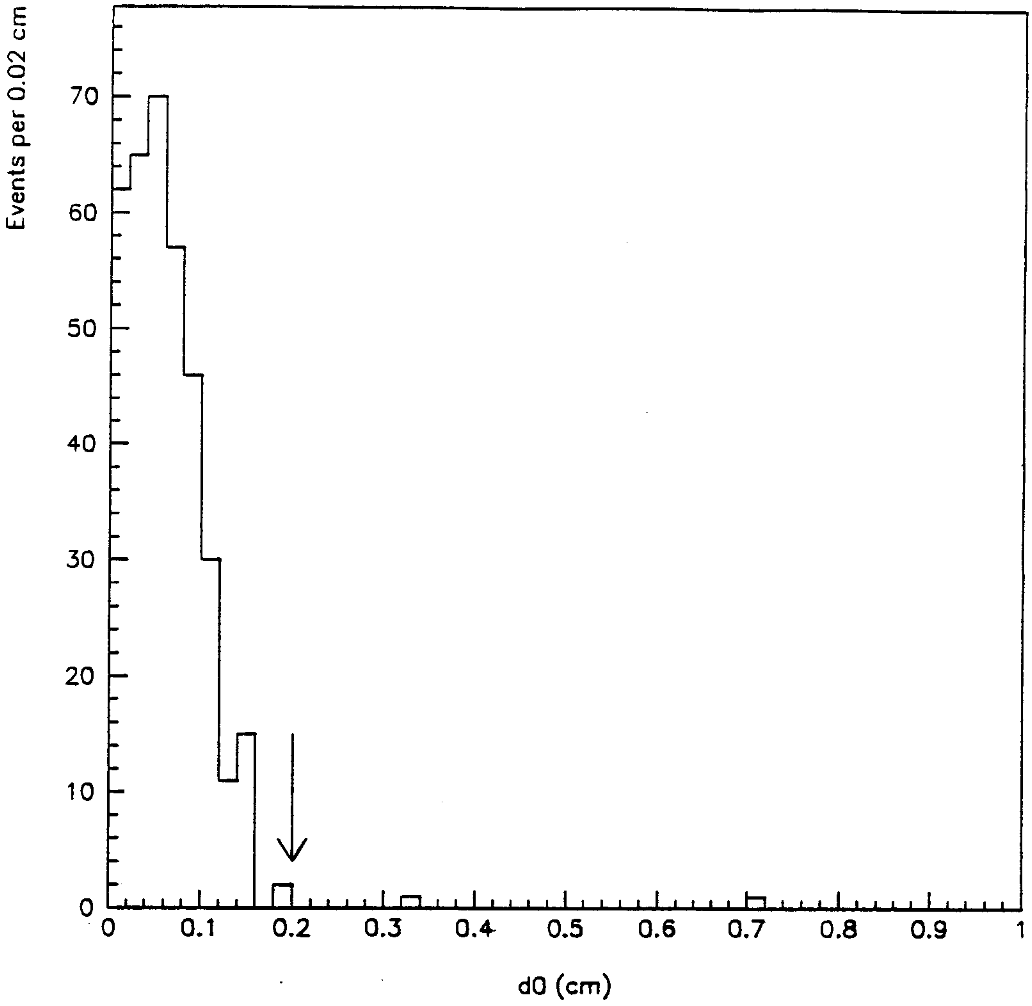

Figure 3.15

Distribution of impact parameter by muons from $Z^0 \rightarrow \mu\mu$ events.

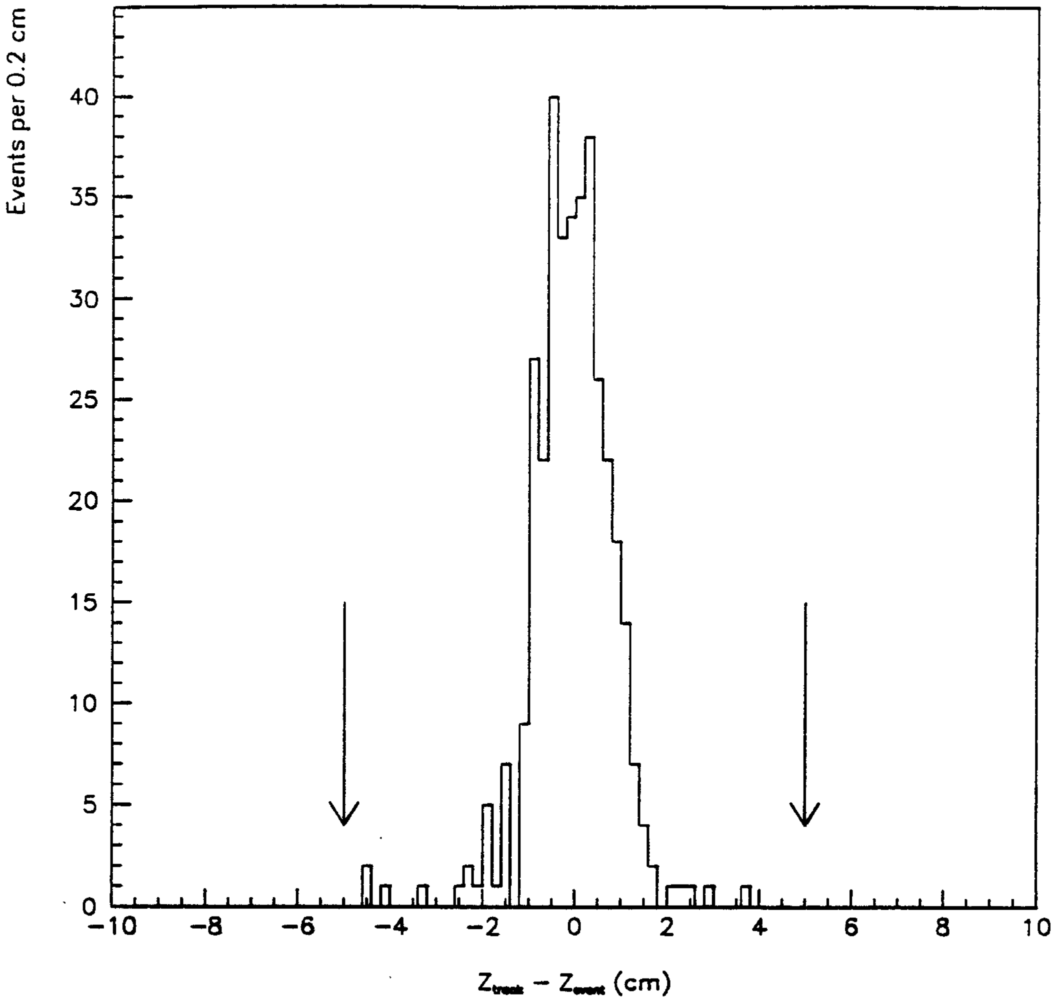

Figure 3.16

The distribution of $Z_{track} - Z_{vertex}$ in $Z^0 \rightarrow \mu\mu$ events.

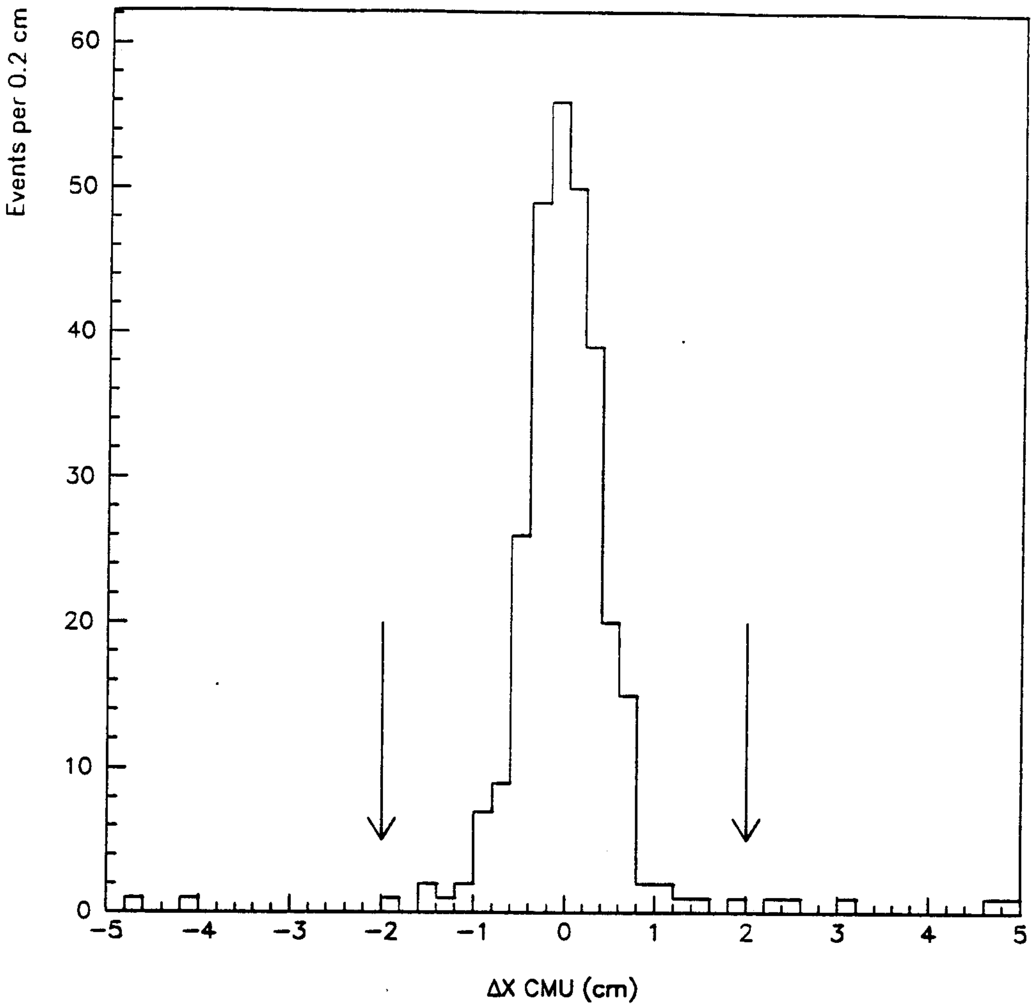

Figure 3.17

Azimuthal matching distribution in the CMU in $Z^0 \rightarrow \mu\mu$ events.

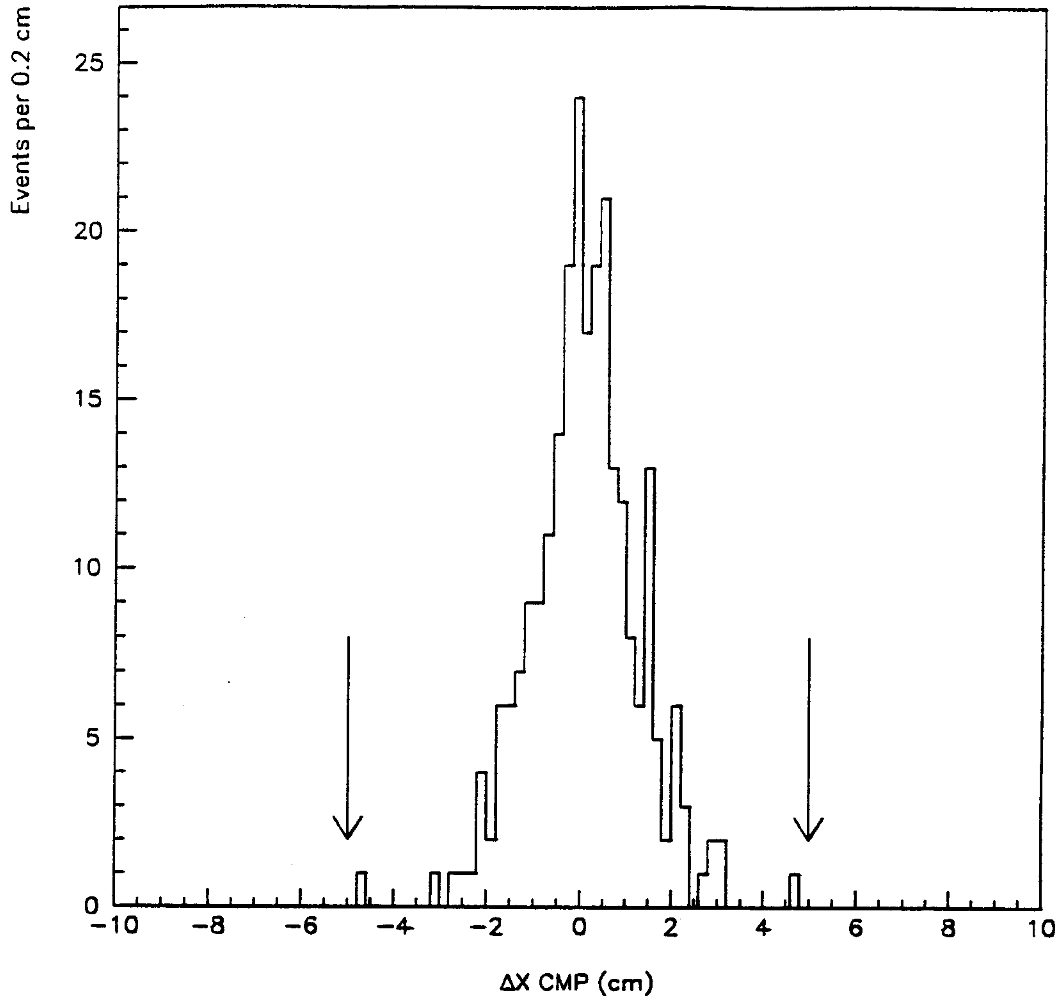

Figure 3.18

Azimuthal matching distribution in the CMP in $Z^0 \rightarrow \mu\mu$ events.

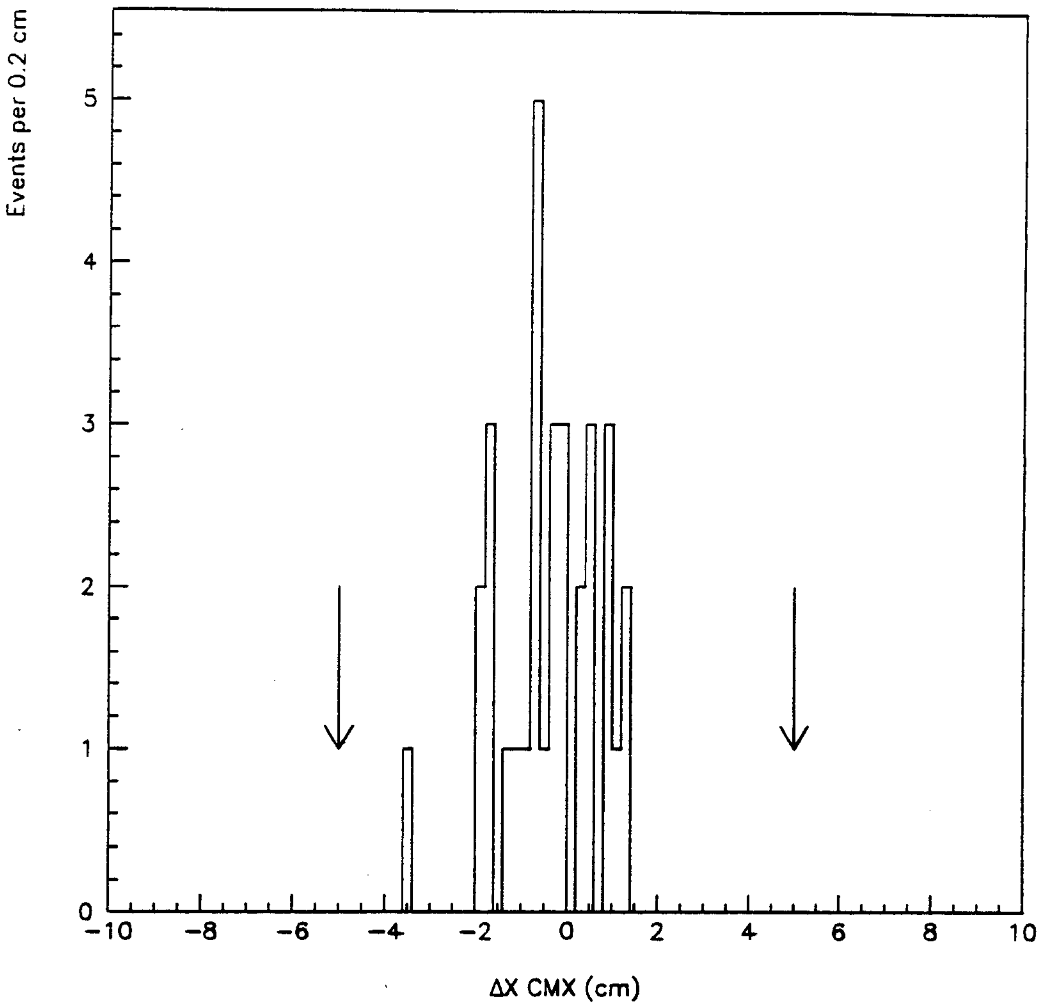

Figure 3.19

Azimuthal matching distribution in the CMX in $Z^0 \rightarrow \mu\mu$ events.

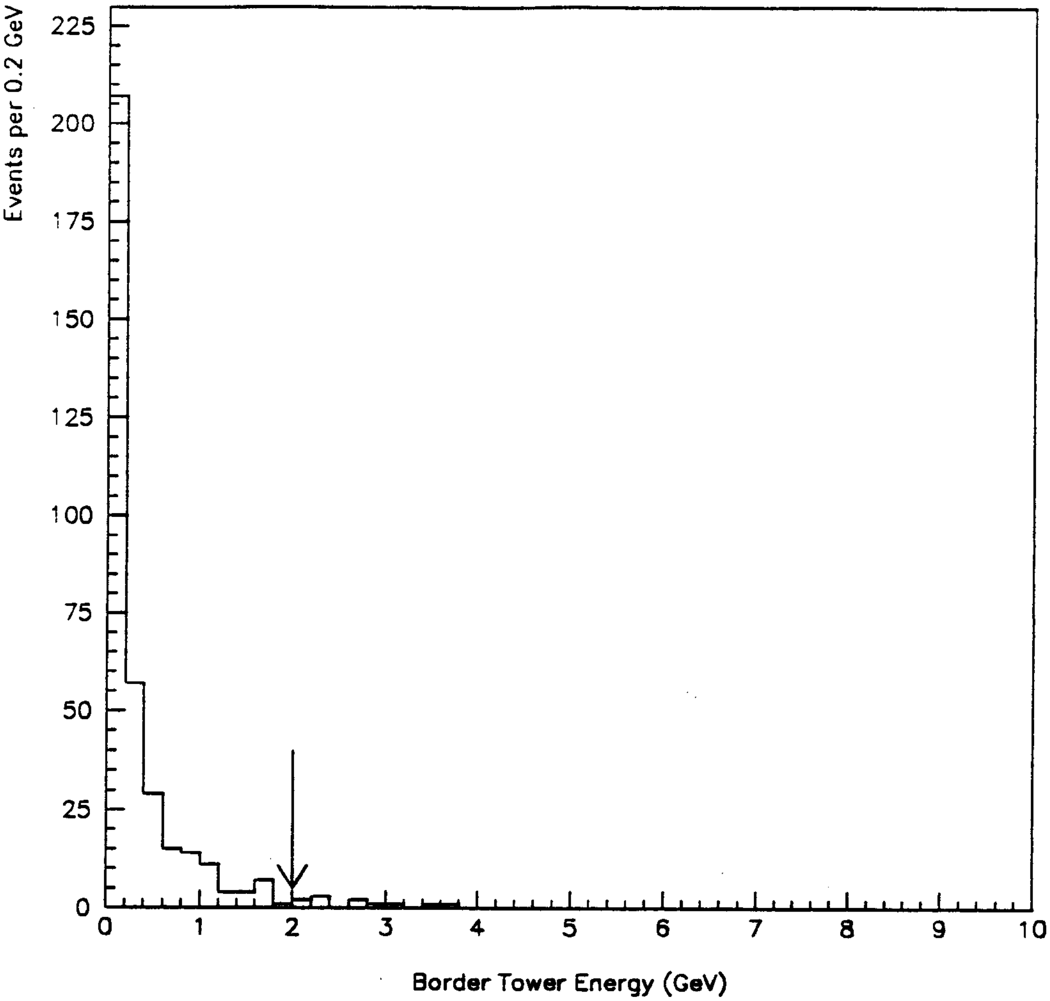

Figure 3.20

Border tower energy for muons from $Z^0 \to \mu\mu$ events.

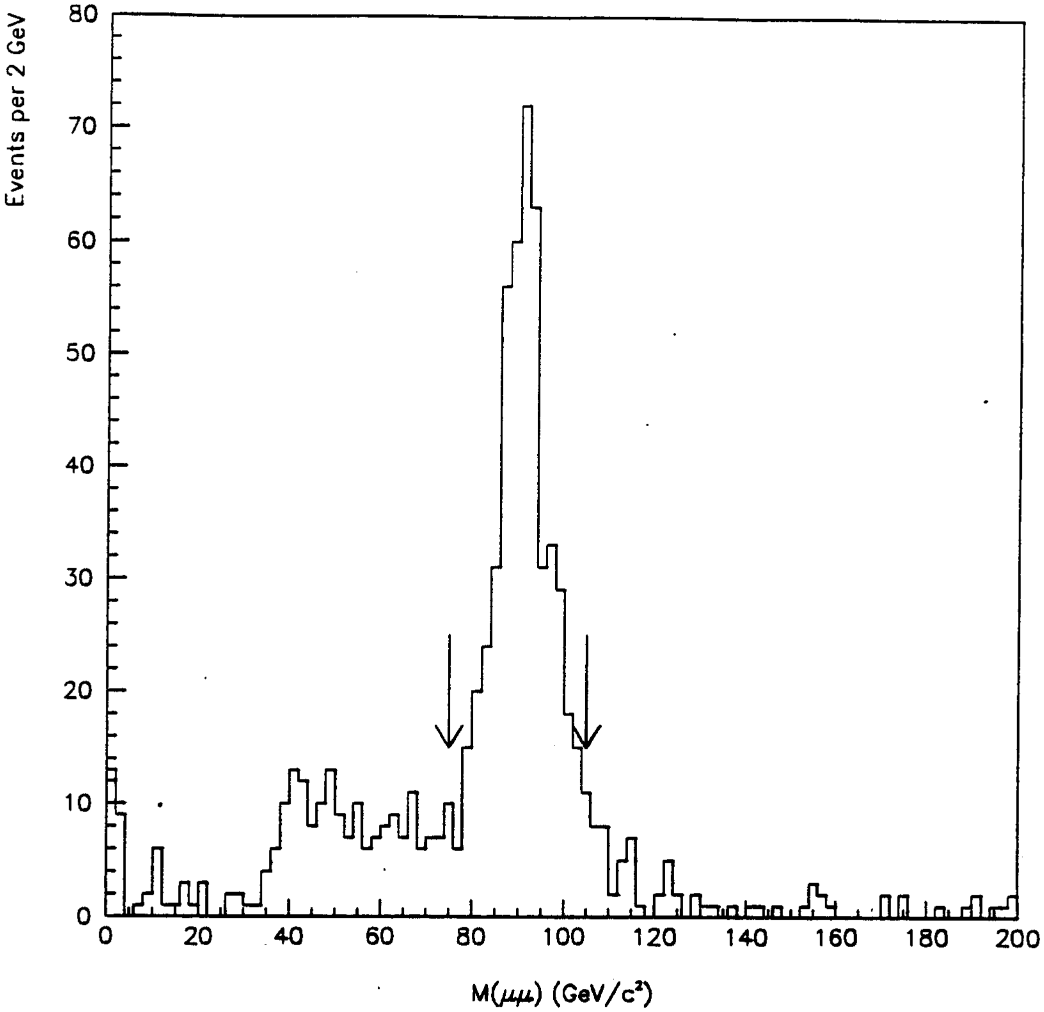

Figure 3.21

Dimuon mass distribution for $Z^0 \rightarrow \mu\mu$ events.

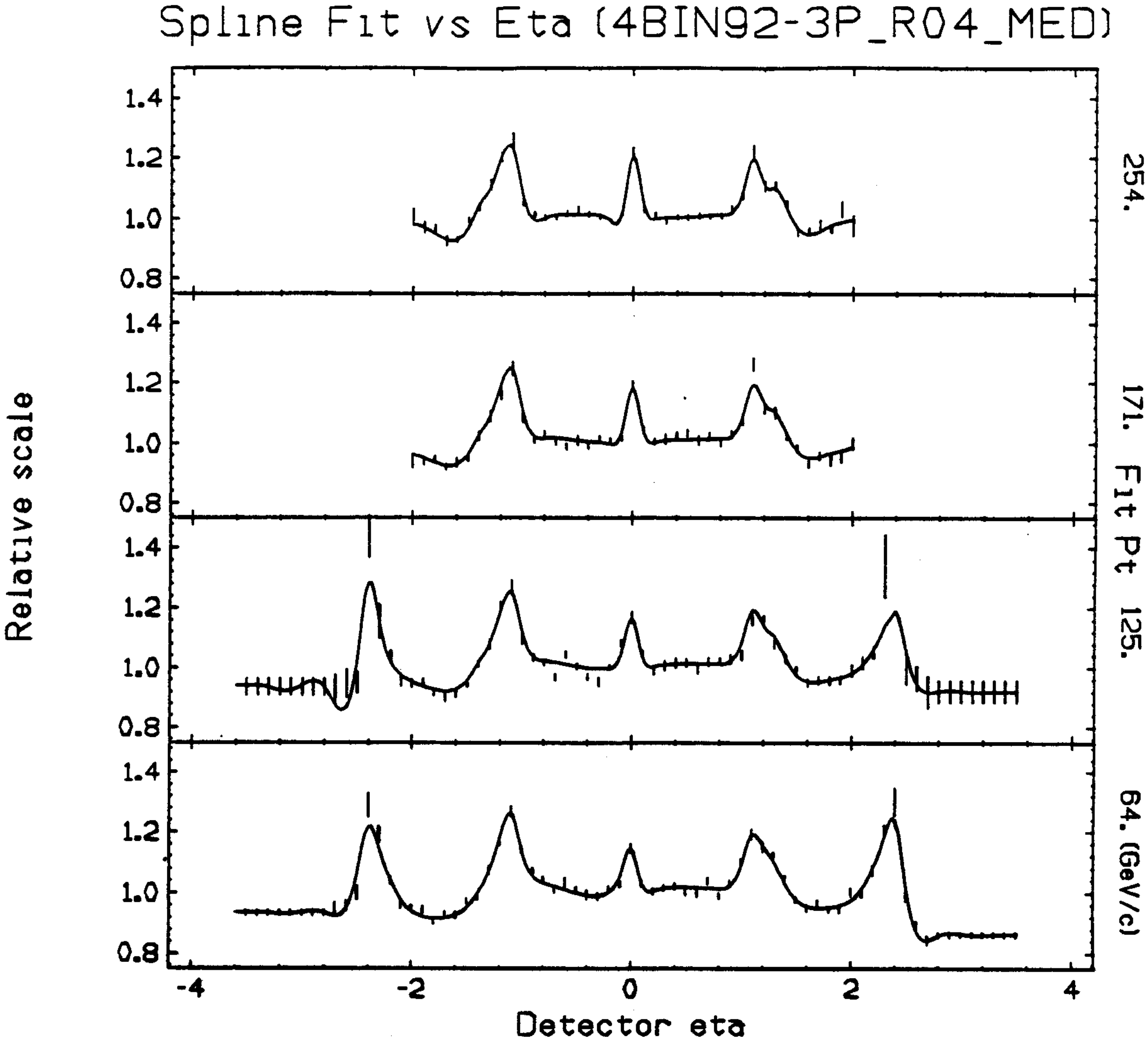

Figure 3.22

Relative jet correction for $\Delta R = 0.4$ for di–jet data.

4. MONTE CARLO DATA SETS

This chapter is devoted to describing the Monte Carlo event samples used in the study of the $t\bar{t}$ signal region as well as the W+jets, di–boson, and $Z \rightarrow \tau\tau$ backgrounds. The simulation packages will be reviewed, as well as MC based jet and missing transverse energy corrections, and how to normalize MC lepton acceptances to the acceptances seen in the data.

4.1 Generation of $t\bar{t}$ Samples

The ISAJET Monte Carlo program [25] was used to generate $p\bar{p}\rightarrow t\bar{t}+X$ events. The fragmentation of the b quark in $t \rightarrow b + W$ was then modeled with the QQ MC package developed at CLEO [26]. Features of these packages are described below:

4.1.1 The ISAJET Package

ISAJET simulates $t\bar{t}$ events in four stages. In the first stage, a parton level hard scattering is generated according to the two jet α_s^2 QCD process. The QCD cross section has the form:

$$\sigma = \hat{\sigma} * F(x_1, Q^2) * F(x_2, Q^2), \tag{4.1}$$

where $\hat{\sigma}$ is the $t\bar{t}$ cross section; $F(x, Q^2)$ is a structure function incorporating QCD scaling violations (the structure functions used are Eichten's); x_1 and x_2 are the parton momentum fractions; and the Q^2 scale is taken to be:

$$Q^2 = \frac{2stu}{s^2 + t^2 + u^2}, \tag{4.2}$$

where s, t, and u are space-, time-, and u–channel Mandelstam invariants. The event is accepted if its QCD cross section is larger than a uniform random number times an envelope for the two jet differential cross section. This procedure produces unweighted events.

The second step in the generation process is to introduce QCD radiative corrections to both the initial and final state partons as they develop into parton cascades. This process is approximated by techniques developed by Fox and Wolfram. The QCD cascade is determined by the probability for going from mass t_0 to mass t_1 emitting no resolvable radiation. The radiation of gluons, photons, W's, and Z's are included.

Step three involves quarks and gluons fragmentating into hadrons using the independent fragmentation scheme of Feynman and Field. Quark–antiquark and meson pairs are also formed at this time. Independent fragmentation correctly describes fast hadrons in a jet, but does not quite conserve energy. Energy conservation is imposed by boosting the hadrons to the appropriate rest frame and rescaling the momenta. Heavy quarks (c,b,t) are fragmented according to the Peterson parameterization [12].

The final step is the addition of "beam jets" to the hard scattering processes outlined above. Beam jets result from spectator parton interactions. These minimum bias reactions are generated with a simplified scheme proposed by Abramovskii, Kanchelli, and Gribov. This model has been tuned to agree with experimental results.

4.1.2 The CLEO Simulation Package

After ISAJET has produced its output, the decay products of the b-quark produced from $t \rightarrow b + W$ are stripped out, and the b-quark fragmentation resimulated with the CLEO MC generator QQ. QQ is based on work done by Isgur, Scora, Grinstein, and Wise [27]. The matrix elements employed in QQ are derived using the quark potential model. The matrix elements for the c-quark are fully computed, while the b-quark elements are tuned to data. The lepton spectra from this MC agrees with data taken at CLEO.

4.1.3 $t\bar{t}$ Data Sets

ISAJET version 6.36 and QQ version 8.01 were run to produce five data sets with m_{top} = 100, 120, 140, 160, and 180 GeV/c^2. Only events with an electron and/or muon with generated $P_T > 12$ GeV/c are kept for later detector simulation. (Events not kept still contribute to the integrated luminosity.) The transverse momentum of the top quark was constrained lie between 1 and 500 GeV/c.

The mass, cross section, and integrated luminosity for these data sets are listed in table 4.1. These data sets were normalized to the theoretical NLO cross section described in section 1.4, not to the LO cross section calculated by ISAJET.

4.2 Generation of Di–Boson Samples

ISAJET was used to generate WW, WZ, and ZZ di–boson data sets. Though the expected cross section for these processes is quite small, they are included so as to make the background calculation as complete as possible.

4.2.1 ISAJET Di–Boson Generator

The general method that ISAJET utilizes to generate events is discussed in section 4.1.1. The difference between $t\bar{t}$ and di–boson generation occurs in step 1 of that section. Production of di–bosons is generated through quark-antiquark annihilation, i.e. $q + \bar{q} \rightarrow W^+W^-$ or Z^0Z^0 or $W^\pm Z^0$. The full matrix element for the $W^\pm$ and Z^0 decays, calculated in the narrow resonance approximation, is included. This calculation is a leading order calculation. Higher order processes, e.g. $q + q \rightarrow q + q + W^- + W^+$, are not included but become important at high enough mass.

Table 4.1

Integrated luminosities of the ISAJET $t\bar{t}$ samples. For each top mass, the cross section and integrated luminosity are given.

m_{top} (GeV/c^2)	$\sigma_{t\bar{t}}$ (pb)	$\int \mathcal{L}dt$ (pb^{-1})
100	$102^{+39.0}_{-15.7}$	$294.1^{+112.5}_{-45.27}$
120	$38.9^{+10.8}_{-5.2}$	$771.2^{+214.1}_{-103.1}$
140	$16.9^{+3.6}_{-1.8}$	$614.9^{+131.0}_{-65.5}$
160	$8.16^{+1.37}_{-0.75}$	$1225^{+205.8}_{-112.6}$
180	$4.21^{+0.57}_{-0.35}$	$1188^{+160.8}_{-98.7}$

Next to leading order calculations have been made by Ohnemus et al. [28], and the following cross sections were obtained for $\sqrt{s} = 1800$ GeV:

$$\sigma(WW) = 9.39 \pm 3.98\text{pb}$$

$$\sigma(WZ) = 2.56 \pm 1.09\text{pb}$$

$$\sigma(ZZ) = 1.08 \pm 0.46\text{pb}$$

The uncertainty on these cross sections is taken to be: 30% for the difference between the ISAJET and NLO cross section, 30% for the ISAJET modeling of the jet multiplicity in these events. All uncertainties are added in quadrature.

4.2.2 Di–Boson Data Sets

Version 6.43 of ISAJET was run to produce WW, WZ, and ZZ di–boson data

Table 4.2

Integrated luminosities of the ISAJET di–boson samples. For each process the cross section and integrated luminosity are given.

Channel	$\sigma_{t\bar{t}}$ (pb)	$\int \mathcal{L}dt$ (pb^{-1})
WW	9.39	1677
WZ	2.56	3906
ZZ	1.08	9259

sets with 10,000 events in each set. Only events with an electron and/or muon with $P_T > 12$ GeV/c were kept in the final sample for later detector simulation. The Eichten Structure Functions were used. The transverse momentum of the bosons was constrained to lie between 0.1 and 200 GeV/c. Table 4.2 lists the cross section and integrated luminosity for the di–boson data sets using the NLO calculations.

4.3 Generation of $Z \rightarrow \tau\tau$ Samples

ISAJET was used to generate a large number of $Z \rightarrow \tau\tau$ events to estimate the tagging rate for this class of events.

4.3.1 ISAJET Z Generator

The generation of Z^0+jets events differs from that of ISAJET $t\bar{t}$ events in step 1 of section 4.1.1. Z^0's are produced with non-zero transverse momentum, and with the full matrix elements of the Z^0 decay. This process yields a $1/P_T^2$ singularity as

$P_T \rightarrow 0$. A reasonable cross section is obtained for small P_T by introducing a cutoff roughly like that used in QCD theory for summing leading double logarithms. This cutoff is then adjusted to give a result consistent with experimental data.

The uncertainty on the cross section is taken to be 30% due to discrepancies between the jet spectra produced by ISAJET and real data.

4.3.2 $Z \rightarrow \tau\tau$ Data Sets

ISAJET version 6.43 was used to generate 100,000 $Z \rightarrow \tau\tau$ events. Only events with an electron and/or muon with $P_T > 15$ GeV/c were kept for later detector simulation. The Eichten structure functions were used. The transverse momentum of the Z^0 was between 0.1 and 200 GeV/c. The integrated luminosity is 484.6 pb^{-1}, and the cross section is 206.7 pb.

4.4 Generation of the W+jets Samples

By far the most important background in the top search is W+jets. The cross section for this process is of same order as $t\bar{t}$ events with $100 < m_{top} < 200$ GeV/c^2. This section describes the VECBOS W+n jet Monte Carlo program [29] as well as the data sets produced.

4.4.1 The VECBOS W+n Jet Generator

The W+n jet Monte Carlo samples were generated with the VECBOS package. This MC employs the full matrix element calculation evaluated at tree level. The evaluated matrix elements can be found in reference [30]. These calculations are carried out at the parton level, which is to say they represent transition probabilities between states containing only quarks and/or gluons. These probabilities generate events by providing four–momenta of the partons and a weight for the event. The calculation of the matrix elements is hideously slow. To speed up the calculation, the Maxwell-Parke approximation [30] is used which cuts execution time by 80%.

At tree–level, the strong coupling constant—derived by perturbative QCD—is given by:

$$\alpha_s(Q^2) = 12\pi/(33 - 2n_f)\log(Q^2/\Lambda^2), \tag{4.3}$$

where Q^2 is the QCD scale, n_f is the number of flavors, and $\Lambda = 0.2$ GeV. The cross section has a strong dependence on α_s. Perturbative QCD provides information on how α_s scales, but not its magnitude. This produces potential trouble, as an error of 10% in $\alpha_s(Q^2)$ can lead to an error of 50% in the cross section for the W+4 jet case. As an example, a $Q^2 =< P_T^{jets} >^2$ yields a cross section of 6.56 pb, while a $Q^2 = M_W^2$ yields a cross section of 1.87 pb for a certain W+4 jet data set [31]. Data sets used in this analysis were generated with $Q^2 =< P_T^{jet} >^2$, the average jet P_T squared. This value of Q^2 was picked so as to produce the most pessimistic (highest) cross section.

As mentioned above, VECBOS produces a weight for each event. One could just keep the weight and make all subsequent calculations by folding in the weight for each event. Unfortunately simulating and then storing such an inordinate number of events is not practical. It then becomes necessary to devise some sort of unweighting procedure to reduce the number of events that need to be simulated. The procedure used starts by locating the maximum weight in a sample. (All samples are large enough to insure that the maximum weight is unlikely to be surpassed by further generation.) Call this weight w_{max}. A probability for event i can then be assigned which is defined as $p_i = w_i/w_{max}$, where w_i is the VECBOS weight for event i. Then a random number between 0 and 1 is generated, and the event is kept if the probability, p_i, is greater than the random number. This procedure has been checked by comparing unweighted distributions (i.e., E_T of jets, η of jets, P_T of the W, etc.) to the weighted distributions [32]. To within statistical error, the unweighted distributions are nearly identical to the weighted distributions.

The final generation phase involves turning the parton four–momentum given by VECBOS into a jet. SETPRT is utilized to do this. SETPRT is a program based on the Feynman–Field independent fragmentation model which results in a one–to–one correspondence between partons and jets. Due to this one–to–one correspondence, each parton should fragment into at most one jet. The fragmentation parameters are tuned to data collected at CDF.

4.4.2 VECBOS W+n Jet Data Sets

VECBOS was run to produce a large set of W+3 and 4 jet events. The structure function used was MSRD0, and the detector simulation package used was QFL. The W was forced to decay in the $e\nu$ channel only. The MC samples were produced with the following cuts imposed at the generation level:

$$\Delta R^{jet-jet} > 0.4$$

$$P_T^{jet} > 8 \text{ GeV}$$

$$|\eta_{jet}| < 2.5$$

$$P_T^{e} > 12 \text{ GeV}$$

$$|\eta_e| < 2.5 \text{ for } W\text{+3 jets, and } |\eta_e| < 1.5 \text{ for } W\text{+4 jets.}$$

Table 4.3 lists the integrated luminosity and cross section for the W+3 and 4 jet data sets generated with VECBOS.

As mentioned, these samples are in the $e\nu$ channel only. Since high P_T muons are also allowed in this top search, some conversion factor must be constructed to take into account this extra acceptance. A study of the inclusive electron and muon data sets was made to determine this conversion factor. Electrons and muons were accepted if they had E_T > 20 GeV, satisfied all the lepton cuts in the previous chapter, border energy < 2 GeV, and $\not{E}_T$ > 20 GeV. A jet is defined as an energy

Table 4.3

The VECBOS W+3 and 4 jet Monte Carlo data sets. Results are for $W \rightarrow e\nu$ only, with MSRD0 structure functions.

NJETS	Q^2 GeV^2	σ pb	Luminosity pb^{-1}
3	$< P_T >^2$	193	105.4
4	$< P_T >^2$	65	74.8

cluster in the calorimeter with corrected $E_T > 20$ GeV in a cone of 0.4 with $|\eta_{det}| < 2.0$. Table 4.4 lists the results of this exercise. A conversion factor of 1.59 ± 0.01 will change the acceptance of VECBOS $e + \nu$+jets to $e + \nu$+jets and $\mu + \nu$+jets.

4.5 Detector Simulation

ISAJET and VECBOS Monte Carlo data must be passed through some sort of simulation program that accurately models what the real detector would register if that MC event occurred at CDF. This section describes the QFL MC package that models the CDF detector.

4.5.1 The QFL Detector Simulation Package

QFL is a "generic" detector simulator originally written for the ill-fated SSC. The calorimeter sections of the detector are assumed to be spherical, and cover the full 4π solid angle except for the conical holes in the forward regions. The radiation lengths of various major components (i.e., EM and Had calorimeters) are set by hand, and the response of the detector to electrons, pions, jets, etc, is tuned to collider and testbeam data. There is high agreement between simulated calorimeter response and the response determined from actual data.

Tracking in QFL is accomplished by propagating tracks through the magnetic field until they reach some sort of major material concentration (i.e., CTC inner barrel, VTX and SVX surfaces, etc), then undergo multiple scattering and possible bremsstrahlung, etc. This continues until a track reaches the face of the calorimeter. There is some tuning of tracking parameters to make them as consistent with real data as possible. The muon chambers are also simulated.

The location of the primary interaction vertex along the z-axis is smeared according to a gaussian distribution centered at $z = 0$ cm, with $\sigma = 30$ cm.

4.5.2 Monte Carlo Acceptance Corrections

QFL is an excellent simulation of the CDF detector, however, there is no reason to expect that the high P_T electron and muon acceptance will match exactly the acceptances seen in the data. Furthermore, QFL does not include Level 1–3 triggers. These trigger effects must be included in any MC acceptance calculation.

4.5.2.1 Normalization of e + Jets Data

To normalize the QFL electron acceptance, single high E_T electrons are shot in random directions into QFL. The same cuts as listed in section 3.1.4 (except for the χ^2_{strip} cut and the conversion removal) are then applied to this QFL simulated data. $(77.4 \pm 0.4)\%$ of these simulated electrons pass. A study of $Z^0 \rightarrow e^+e^-$ events with isolated electrons yields an efficiency of $(82.8 \pm 1.4)\%$ (with the χ^2_{strip} cut, but no conversion removal). The conversion removal efficiency was estimated in section 3.1.6 to be $(95 \pm 3)\%$. The high E_T electron trigger efficiency was found to be $(92.8 \pm 0.3)\%$

for electrons with $E_T > 20$ GeV [21]. Putting this all together, the Monte Carlo acceptance needs to be corrected by: $0.828 \times 0.95 \times 0.928/0.774 = 0.943 \pm 0.034$.

4.5.2.2 Normalization of μ + Jets Data (CMU)

The procedure for normalizing CMU and CMU·CMP high P_T muons is simular to that of the e + jets data. Random high P_T muons are shot into QFL and are used if they propagate into the fiducial region. The matching and impact parameter quality cuts listed in section 3.2.3 are then applied to this QFL simulated data, and to a sample of $Z^0 \rightarrow \mu^+\mu^-$ events. The MC dX matching efficiency was found to be 0.9957 ± 0.0025 and 0.9909 ± 0.0021 for CMU and CMU·CMP muons respectively. For real data, the matching efficiencies are $0.973^{+0.007}_{-0.009}$ [22] and 0.940 ± 0.021. The trigger efficiency for these muons is 0.868 ± 0.019 [33]. Therefore, the QFL muon acceptance is degraded by 0.848 ± 0.029 for CMU muons, and 0.823 ± 0.026 for CMU·CMP muons.

4.5.2.3 Normalization of μ + Jets Data (CMX)

As discussed in section 3.2.1, CMX high P_T muons are required to pass the Level–1 calorimeter trigger, as well as pass through superlayer 8 in the CTC. The Level–2 trigger efficiency is $(54^{+5}_{-6})\%$. Only 76% of the luminosity is usable, since for 24% of the run the Level–2 trigger had as a prerequisite a rate–limited Level–1 trigger. In QFL, $(99.16 \pm 2.3)\%$ of the CMX muons pass the dX cut, while $(98.0^{+1.0}_{-1.6})\%$ [22] of $Z^0 \rightarrow \mu^+\mu^-$ with muons in the CMX pass the dX cut. The QFL CMX acceptance then needs to be multiplied by $(40.6 \pm 6.0)\%$.

4.6 Further Jet Corrections

In section 3.3.3, a relative jet correction was described. However, further corrections are needed to transform the measured E_T to the parton E_T. This section describes three additional jet corrections, and how these corrections are produced using ISAJET $t\bar{t}$ MC samples.

4.6.1 Absolute Jet Correction

The energy measured in the calorimeter after the relative jet correction is not equal to the actual energy present in the cone due to fragmentation effects, clustering, detector response, etc. The absolute jet correction is an attempt to transform the measured E_T back to the true E_T in the cone. This process starts by associating a calorimeter cluster with a jet in a $t\bar{t}$ event originating from either a b-quark or a quark from $W \rightarrow$ jets decay. A match between a cluster and a quark is declared if $\Delta R^{parton-jet} < 0.4$. No overlap between partons in a cluster is allowed. The next step is to vectorially sum up the $\vec{P}_T$'s of all the stable particles that ISAJET produces that propagate through the magnetic field into the cone. Neutrinos are excluded from this sum, and muons are allowed to deposit 2 GeV of E_T into the cone or its entire E_T if $P_T < 2$ GeV/c^2. This quantity is then divided by the jet P_T (after the relative jet correction), and plotted for 13 bins of 10 GeV/c width for P_T from 10 to 140 GeV/c. Figure 4.1 displays this ratio for one P_T bin. Owing to the asymmetric nature of this distribution, the mean and variance are found by fitting the distribution to a truncated gaussian. After the first gaussian fit, only data within $\pm 1.5\sigma$ of the mean are fitted. This is iterated until the mean and sigma stabilize, changing less than 1% and 5% respectively. If a distribution has less than 50 entries, the median is used in lieu of the mean. The mean or median of these distributions is defined as $< \frac{P_T^{parton}}{P_T^{jet}} >$ for a specific P_T^{jet} range. P_T^{parton} can then be inferred from the following equation:

$$P_T^{parton} = \langle \frac{P_T^{parton}}{P_T^{jet}} \rangle \cdot P_T^{jet} \tag{4.4}$$

This distribution can be fitted to a quadratic as a function of P_T^{jet}. This is the absolute jet correction, and is shown in figure 4.2. Jets from both b- and W-quarks in the m_{top} = 100, 120, and 140 GeV/c^2 ISAJET $t\bar{t}$ MC data sets were used to derive the absolute jet correction. Due to a lack of statistics at high jet E_T, this correction is accurate for jets with $E_T < 150$ GeV, but since even high mass $t\bar{t}$ events rarely exceed this E_T, it is good enough.

4.6.2 Out of Cone Correction

Jets are not infinitely narrow, but spread out in (η, ϕ) space. Any fixed cone clustering algorithm is bound to lose some jet energy due to particles impinging on the calorimeter outside the clustering cone, and from particles swept away by the magnetic field. An out of cone correction should be constructed so as to add this energy back. The out of cone energy is defined as:

$$OCC = \sum P_T(\text{All parton particles}) - \sum P_T(\text{Parton particles in cone}). \tag{4.5}$$

Neutrinos and muons are not counted in the sums, and $|Z_{vertex}| < 60$ cm. The median of this asymmetric distribution is determined for 13 bins of 10 GeV/c width for $20 < P_T < 150$ GeV/c. The P_T here is the P_T of the jet after the relative and absolute jet corrections. Figure 4.3 is a histogram of one such out–of–cone P_T bin. The median out–of–cone P_T is displayed in figure 4.4 for b-quarks, W-quarks, and the combination of the two as a function of P_T for a cone size of $\Delta R = 0.4$. The curves displayed are arbitrarily chosen functions which are fitted to the points. It is interesting to note how the out–of–cone energy decreases as the P_T increases. This is attributed to relativistic boosting of particles into narrow cones at high P_T. The out–of–cone correction used in this thesis is the combination of the b- and W-quarks.

4.6.3 Underlying Event Correction

An estimate of the underlying event energy was made using minimum bias data.

The average $\sum E_T$ over the calorimeter was found to be 5.78 GeV in the region $|\eta| < 1.0$ [34]. This translates to 0.37 GeV in a cone of $R = 0.4$. This assumes the underlying event in min-bias events is simular to $t\bar{t}$ events.

4.6.4 Results

Figure 4.5 is a plot of quark E_T (no μs and νs) minus corrected jet E_T for both b- and W-quarks in $t\bar{t} \rightarrow (e, \mu) + \nu$+jets events. The jets have corrected $E_T > 20$ GeV, and $|\eta_{det}| < 2.0$. To insure no overlaps between quarks, $\Delta R^{jet-quark} < 0.2$, and no other quark can be within $\Delta R = 0.4$ of the jet. The corrected jet E_T is on average 0.94 GeV higher than the true E_T. However, additional energy can leak into the cone which accounts for this slight overestimate.

These jet corrections were derived entirely with the ISAJET $t\bar{t}$ MC generator. A sample of $m_{top} = 160$ GeV/c^2 $t\bar{t}$ events was generated with the HERWIG [35] MC package. A plot of quark E_T minus corrected jet E_T was made for the HERWIG data as described in the preceding paragraph. The corrected jet E_T was 0.77 ± 0.27 GeV lower than the true E_T. The small difference between the corrected jet E_T and quark E_T in samples generated by two different $t\bar{t}$ MC's strengthens the claim that this jet correction scheme is producing correct results.

4.7 Further Missing E_T Corrections

Section 3.4 describes how the raw $\not{E}_T$ is formed, and how to correct the $\not{E}_T$ for muons and high E_T electrons. This section provides a prescription for additional corrections using corrected jet energy.

4.7.1 The Method

The $\not{E}_T$ correction is based on ISAJET MC $t\bar{t}$ events, and consists of four parts which correspond to different energy deposits in the calorimeter. The four parts are: electron clusters; muons; jets; and unclustered energy. Each part is corrected separately, and the corrected $\not{E}_T$ formed from these four constituents. There must be no overlap between these components so as to avoid double counting. The electron energy is simply the energy deposited by the electron. The muon energy deposited in the calorimeter is described in section 3.4. Jet clusters are required to have $P_T^{raw} >$ 10 GeV/c. The unclustered energy is what remains and is defined thusly:

$$UCE_i^{raw} = -\left(\sum^{prim\,ele} E_i^{ele,raw} + \sum_{clus}^{P_T^{raw} > 10\,GeV} P_i^{jet,raw} + \sum^{all\,\mu} E_i^{muon} + \not{E}_{T_i}^{raw} \right),\ i = 1,2 \tag{4.6}$$

The symbols follow from above. After all four components have been corrected, the corrected $\not{E}_T$ can is defined as:

$$\not{E}_{T_i}^{cor} = -\left(E_i^{ele,cor} + \sum_{clus}^{P_T^{raw} > 10\,GeV} P_i^{jet,cor} + P_i^{muon,cor} + UCE_i^{cor}\right),\ i = 1,2 \tag{4.7}$$

One note: $P_i^{jet,cor}$ is the jet energy after the relative and absolute jet corrections. The out–of–cone and underlying event corrections are not included as that would double count energy.

The corrected unclustered energy, UCE^{cor}, is determined by passing ISAJET $t\bar{t} \rightarrow e + \not{E}_T +$jets events through QFL to produce a raw UCE. The true unclustered energy is then calculated from ISAJET. (Neutrinos are not included, and muons are allowed to deposit, at most, 2 GeV of unclustered transverse energy.) The raw unclustered energy is calculated according to equation 4.6. Both values are plotted in a scatter plot and parameterized to give a correction factor. The raw and true unclustered energy vectors are broken into two components parallel and perpendicular to the lepton from the semileptonic decay of the W. Scatter plots for various top masses for the two UCE components are plotted in figures 4.6 and 4.7. The correlation between the measured and true UCE in the parallel view is quite high. The scale factor here is taken to be: $UCE_{par}^{cor} = 1.5 \times UCE_{par}^{raw}$. The correlation in the perpendicular view is rather poor, so no correction in made in this view (i.e. $UCE_{perp}^{cor} = UCE_{perp}^{raw}$).

4.7.2 Results

Histograms of the difference between corrected and raw $\not{E}_{\mathrm{T}}$ from $P_T^{\nu, W \rightarrow e\nu}$ for various top masses are shown in figure 4.8.

Table 4.4

Number of W events in the e and μ channels. A jet is defined as a cluster of energy in the calorimeter with corrected $E_T > 20$ GeV in a cone of 0.4 with $|\eta_{det}| < 2.0$. All errors are statistical only.

Number of jets	$e+\not{E}_T$+n-jets	$\mu+\not{E}_T$+n-jets	$R_{e \to e+\mu}$
0	7959	4596	1.58 ± 0.01
1	910	600	1.66 ± 0.03
2	166	94	1.57 ± 0.05
3	31	22	1.71 ± 0.12
≥ 3	39	26	1.67 ± 0.10
all jets	9074	5316	1.59 ± 0.01

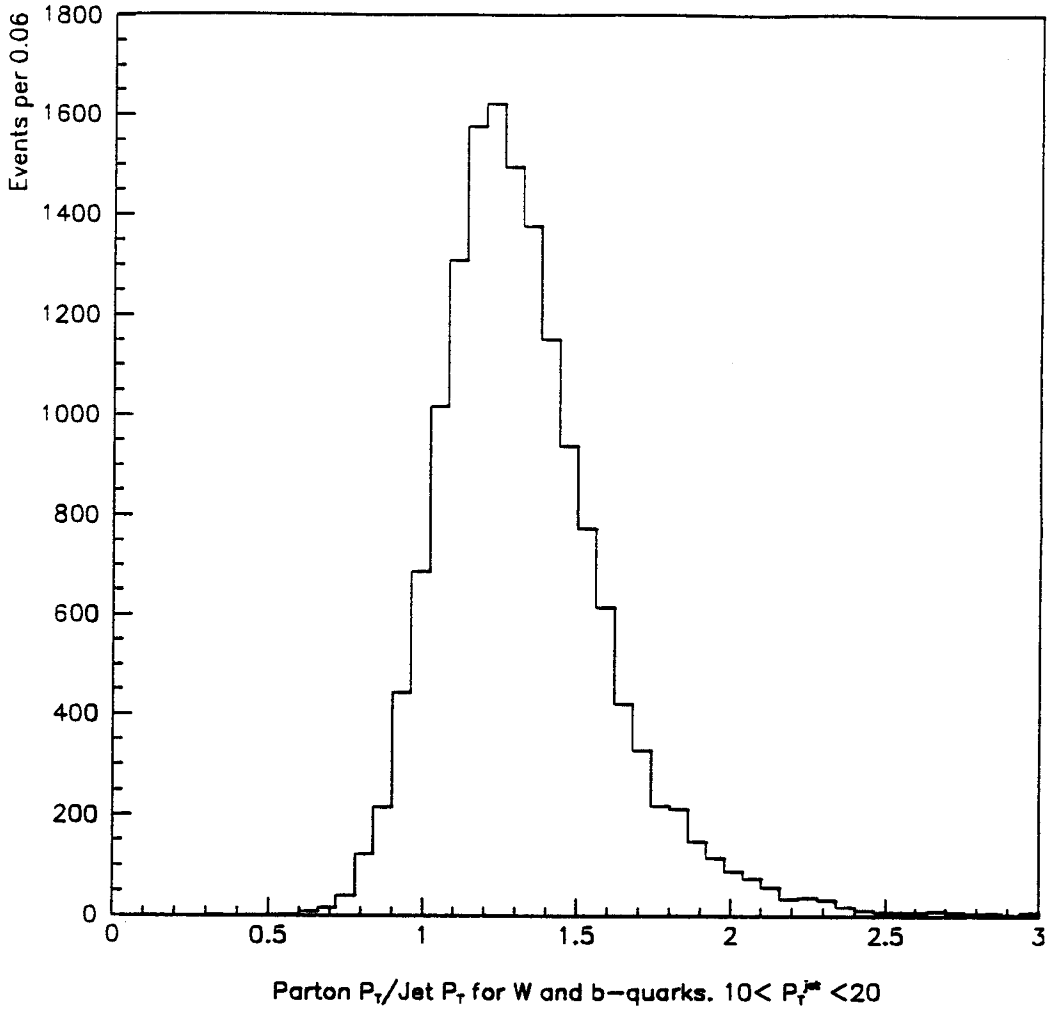

Figure 4.1

Ratio of parton P_T to jet P_T for a cone of 0.4. The partons included are W- and b-quarks with $10 < P_T^{jet} < 20$ GeV. All data is from the $m_{top} = 100, 120,$ and 140 GeV/c^2 samples.

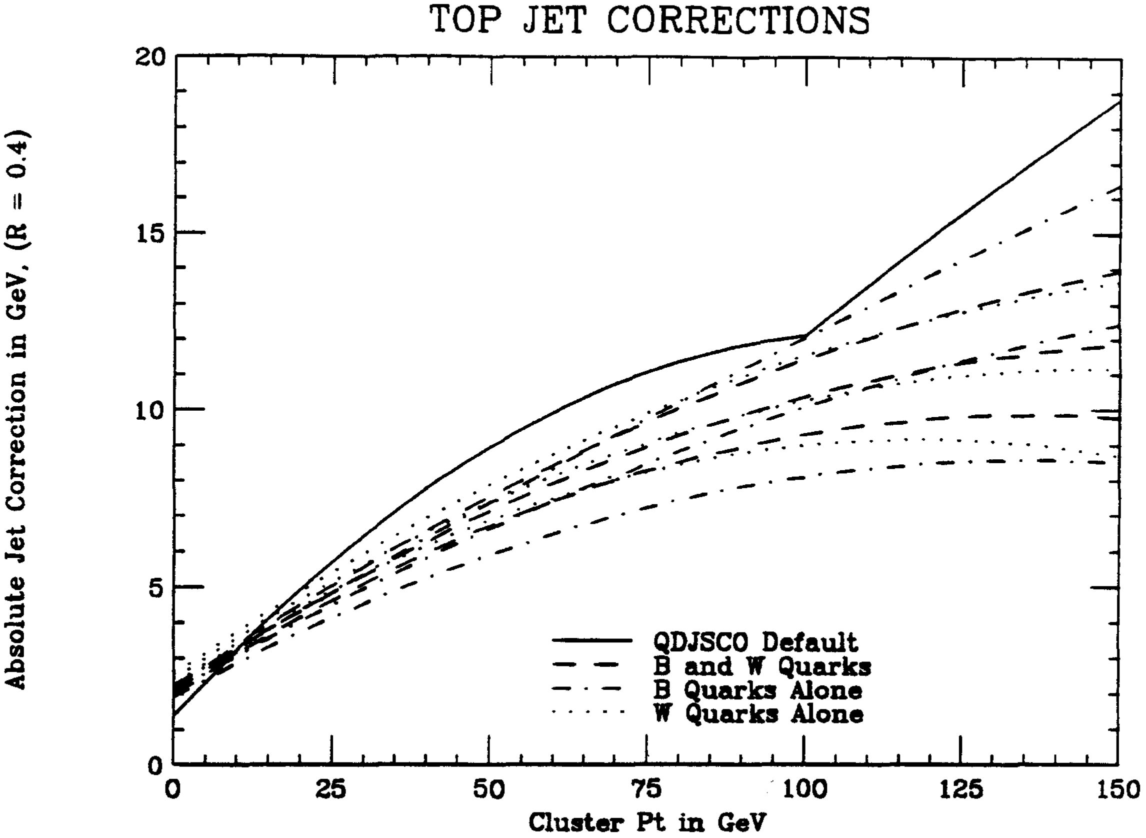

Figure 4.2

Absolute jet correction for $\Delta R = 0.4$. Plotted on the ordinate is the jet absolute correction. The abscissa is the jet P_T after the relative correction. The solid line is the standard correction applied in CDF. The dashed line (B and W Quarks) is used in this analysis. Statistical error bands are also plotted.

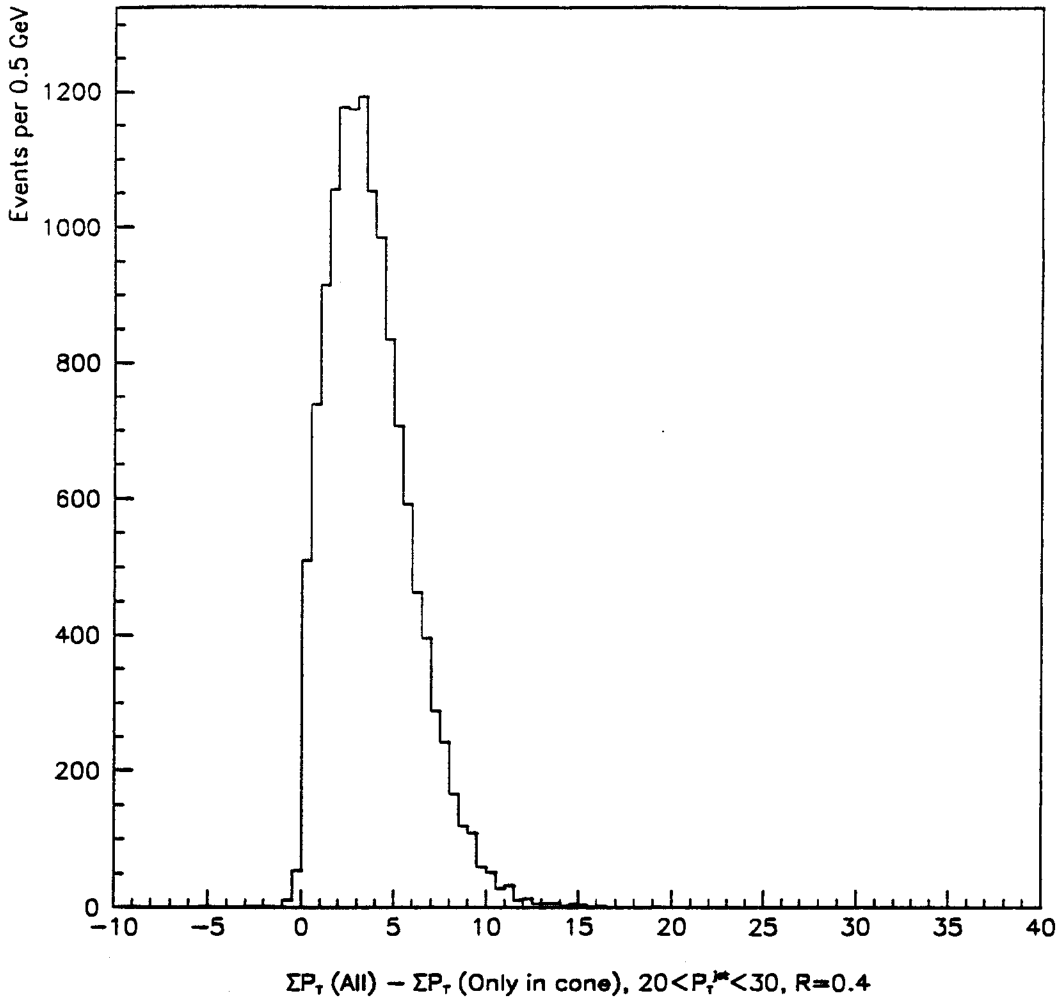

Figure 4.3

Out–of–cone correction for one P_T bin. The P_T range is $20 < P_T < 30$ GeV/c for jets in a cone of $\Delta R = 0.4$.

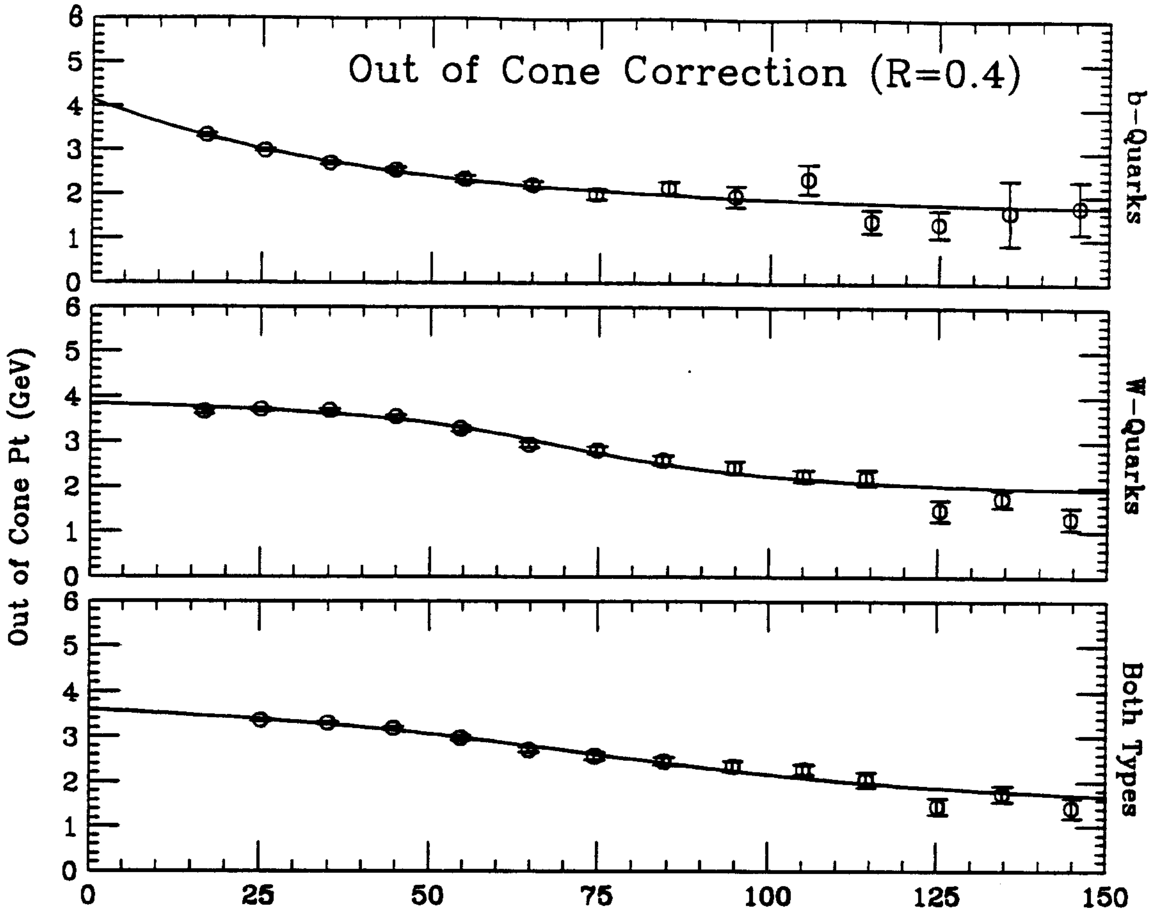

Figure 4.4

Out of cone correction for *b*- and *W*-quarks for $R = 0.4$. The fits are arbitrary. The combination of *b*- and *W*-quarks is the one used in this analysis.

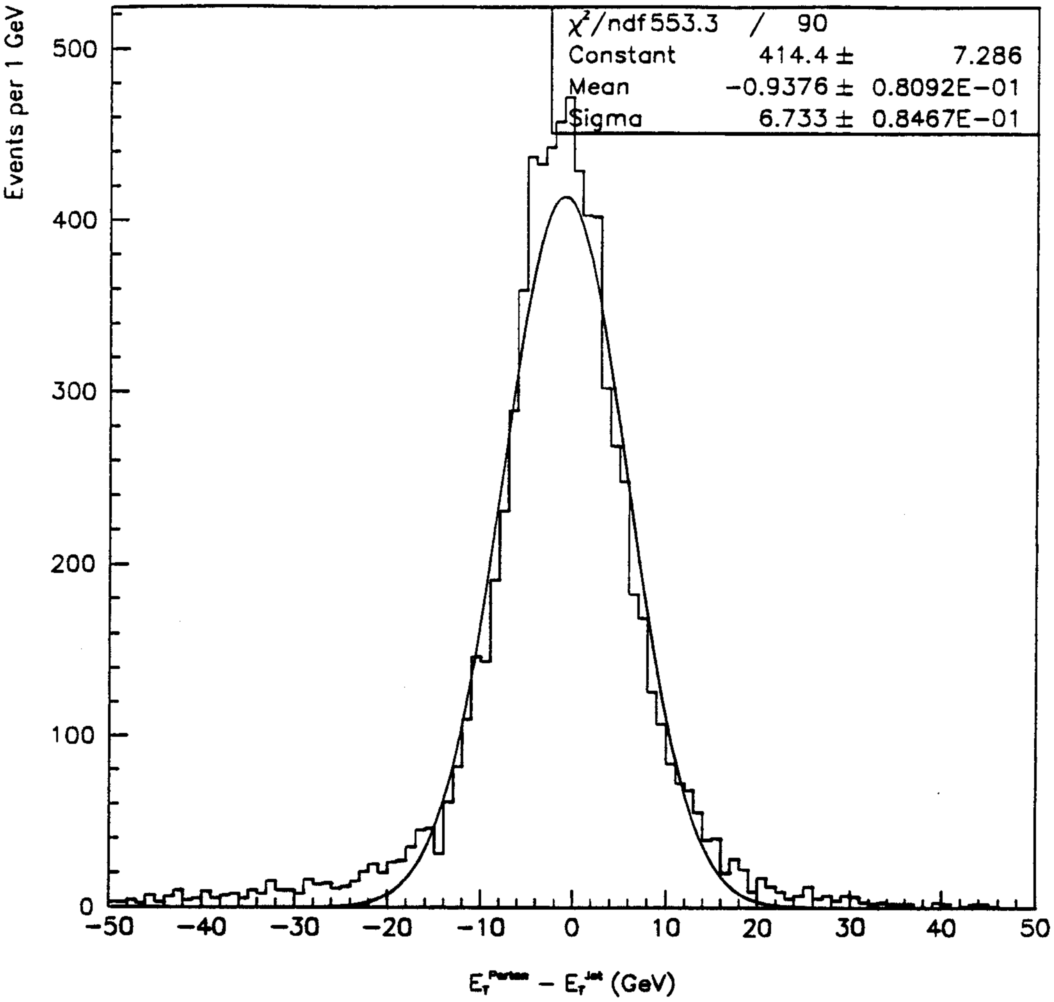

Figure 4.5

b- and W-Quark E_T minus jet E_T^{cor} in $t\bar{t} \rightarrow (e,\mu) + \nu$+jets events.

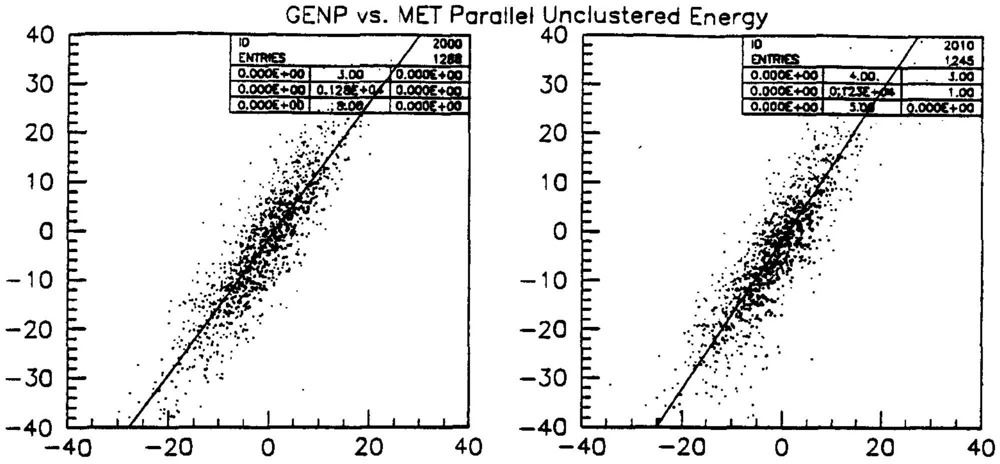
GENP vs. MET Parallel Unclustered Energy

X view, Mtop=100

X view, Mtop=120

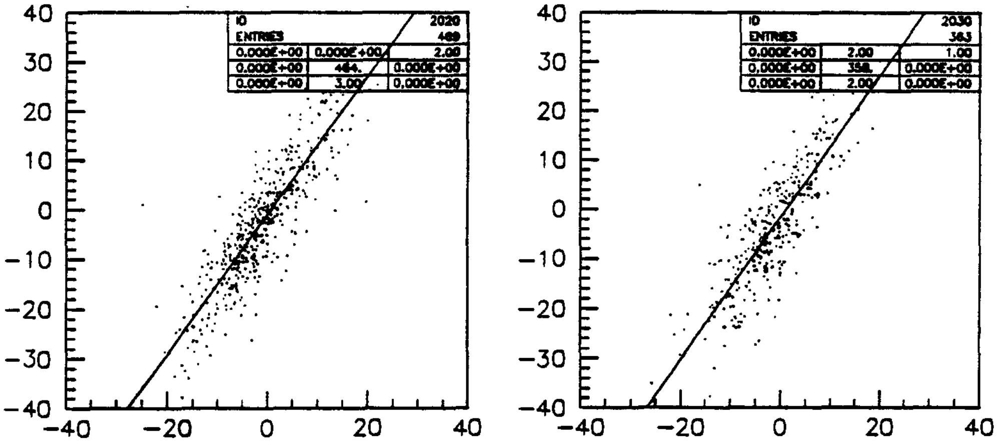

X view, Mtop=140

X view, Mtop=160

Figure 4.6

Unclustered energy, parallel view for various top masses. Plotted on the abscissa is the UCE found after the detector simulation. The ordinate is the actual UCE as determined from ISAJET. The diagonal line is the best fit for each top mass.

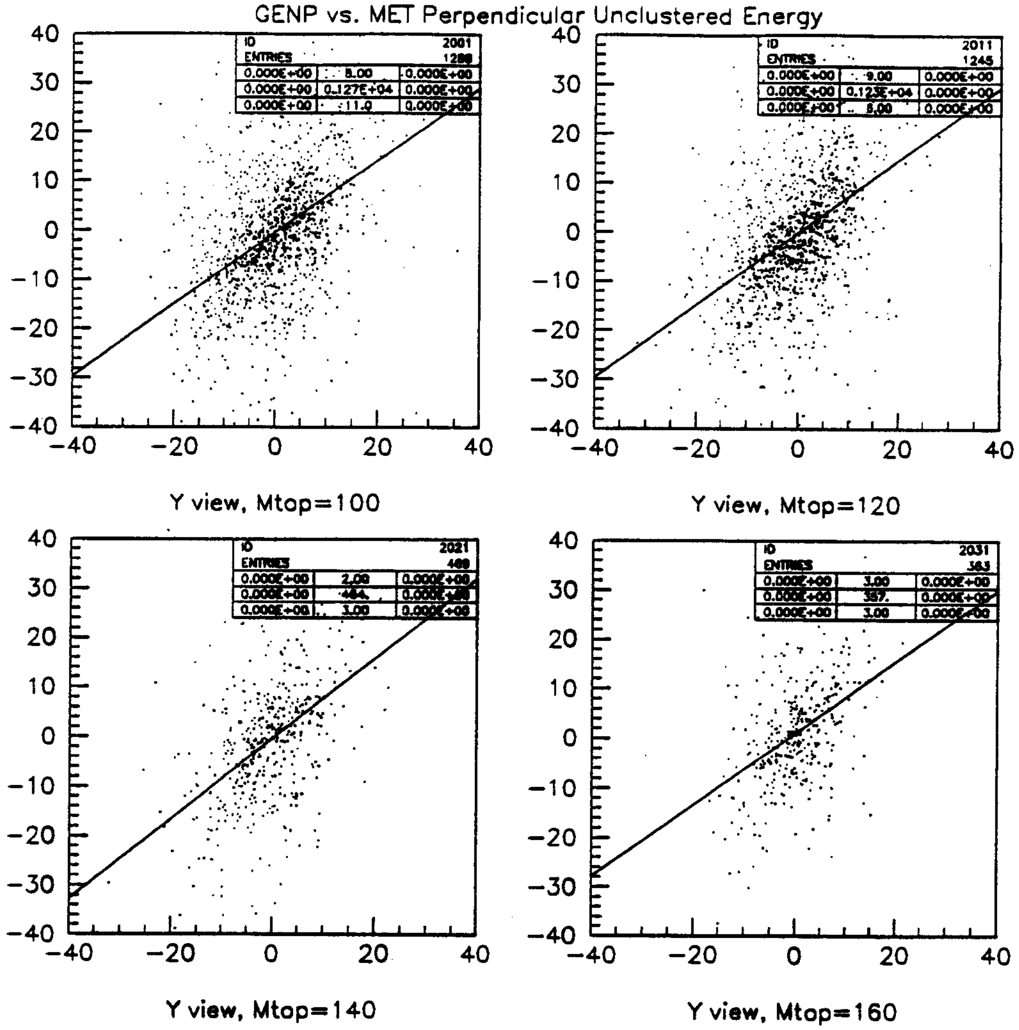

Figure 4.7

Unclustered energy, perpendicular view for various top masses. Plotted along the abscissa is the UCE found after the detector simulation. The ordinate is the actual UCE as determined from ISAJET.The diagonal line is the best fit for each top mass.

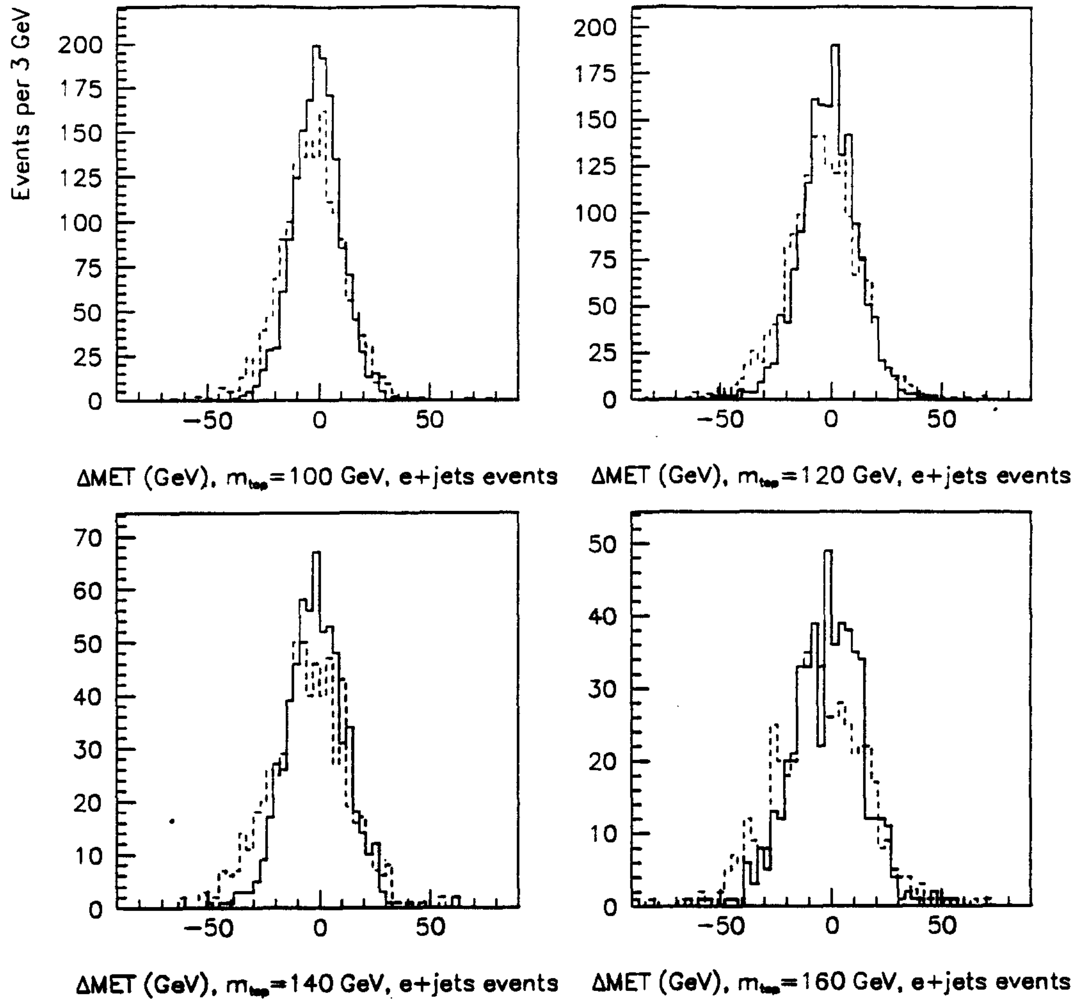

Figure 4.8

Difference between corrected and raw $\not{E}_T$ from $P_T^{\nu, W\to e\nu}$. $\not{E}_T^{cor} - P_T^{\nu, W\to e\nu}$ (solid line) and $\not{E}_T^{raw} - P_T^{\nu, W\to e\nu}$ (dashed line) for $t\bar{t} \to e + \nu$+jets events for four top masses.

5. SOFT LEPTON TAGS

The main background in this top search is W+jets events where the W decays leptonically. This process closely mimics $t\bar{t}$ events, so additional cuts must be made to reduce this background below the expected $t\bar{t}$ rate without significantly reducing the already weak signal process. The best method to reduce W+jets events is to tag b-quarks either by searching for displaced vertexes with the SVX (section 2.3.1) or by searching for additional leptons from the b decay. The later method is used in this analysis, and goes by the title "soft lepton tagging" or SLT. The reason this method is appropriate is that $t\bar{t}$ events always have two b-quarks. Approximately 23% of b-mesons decay directly into an electron or muon. (Additional e's and μ's can be produced from the decay of the two c-mesons (i.e., $b \rightarrow c + X$), and from the W that decays hadronically (i.e., $t \rightarrow Wb$, $W \rightarrow c\bar{s}$). Though these additional leptons are much softer than the leptons produced directly from a b-meson decay, they can still be tagged.) A quick calculation shows that each event should have on average roughly $2 \times 0.23 \approx 0.5$ additional leptons per event. W+jets events rarely have additional leptons. Therefore, tagging additional leptons should subdue this major background process without undue loss of $t\bar{t}$ events. The P_T distribution of leptons from b-quark decay is not excessively soft as can be seen in figure 5.1 for a top with $m_{top} = 160$ GeV/c^2. (The increase at 12 GeV in this plot is due to selecting ISAJET events that have an electron or muon with $P_T > 12$ GeV. See section 4.1.3.)

This chapter outlines the soft electron and muon tagging algorithms, and their associated efficiencies and fake rates.

5.1 Soft Muon Identification

There are four muon detectors at CDF: CMU, CMP, CMX, and FMU. The FMU was not used in this analysis, in part, due to its small acceptance in high mass $t\bar{t}$ events. Tagging muons with the CMU, CMP, CMX poses a minor problem due to the fact that the CMU and CMP overlap in non-trivial ways, and any tagging algorithm must take this into account. (The CMU and CMX have trivial overlaps and can be considered separate systems.) This section describes the fiducial regions, track–quality cuts, muon matching cuts, and the resulting tagging efficiencies and fake rates.

5.1.1 Soft Muon Fiducial Region

The CMU–CMP and CMX fiducial regions will be treated separately, as their overlap is almost nonexistent. Muon candidates in the CMU–CMP region can be of three types: CMU–only, CMP–only, and CMU·CMP muons, depending on P_T and which which stub type(s) the associated track matches too. Tagging muons in the CMU–CMP region begins by determining if the appropriate stubs in the muon chambers are present. If a track has a $P_T < 3$ GeV/c, no stub in the CMP will be required. (Muons with a P_T below $\sim$2.75 GeV/c do not penetrate all the material between the event vertex and the CMP chambers.) Tracks associated with muon stubs are propagated from their origin to the radii of the CMU and CMP chambers. If the track extrapolates to within the larger of 3σ of multiple scattering or 5 cm of the inside chamber edge, a stub will be required. If no stub is present, the muon candidate is rejected. If the muon candidate is a CMU·CMP type and the associated track propagates outside this max(3σ,5 cm) range for either the CMU or CMP chamber edge, the muon matching cuts (section 5.1.3) will be applied only the stub in the muon chamber where the track is inside the max(3σ,5 cm) range.

If muon candidate is in the CMX, a stub must be present if the associated track extrapolates to within within the larger of 3σ of multiple scattering or 5 cm of the inside chamber edge. The CMX muon candidate will be rejected if the P_T of the track is less than 3 GeV/c, as muons with less transverse momentum cannot penetrate all the material between the event vertex and the CMX muon chambers.

5.1.2 Track Requirements

The track associated with the muon stub(s) must be of reasonable quality. Listed below are the quality cuts imposed on all muon tracks:

1. $P_T > 2$ GeV
2. The track must pass through at least two stereo and two axial layers in the CTC to insure good measurement of track parameters.
3. The CTC must report the track as being a fully reconstructed 3D track.
4. Impact parameter < 0.3 cm

In addition to these cuts, muon candidates with CMX stubs must possess at least 0.1 GeV of energy in the hadronic tower the track propagated through. The reason for this minimum energy cut is that the CMX suffers from an inordinate number of bogus hits resulting from a poorly designed flange in the beam pipe. This flange descends too far into the beam pipe and causes a lot of particle spray directed in the forward direction. Demanding a minimal amount of energy in the calorimeter is a partial cure for this problem.

5.1.3 Matching Cuts

The matching cuts were derived from studies of $J/\psi \rightarrow \mu^+\mu^-$ and $Z \rightarrow \mu^+\mu^-$ events. They are tuned to have a high efficiency while also having a low fake rate. The muon candidates must pass the fiducial and track quality cuts given in the above two sections. The selection criteria for soft muons is listed below:

CMU–only stubs

Number of CMU TDC hits ≥ 3	
Number of CMU ASD hits ≥ 3	
CMCLUS < 6	(see below)
$\lvert\Delta Z_{CMU}\rvert <$ Max(3σ,8 cm)	
$\chi^2(X'_{CMU}) < 15$	($P_T < 20$ GeV/c)
$\lvert\Delta X_{CMU}\rvert <$ Max(3σ,2 cm)	($P_T > 20$ GeV/c)

CMU·CMP stubs

Number of CMU TDC hits ≥ 3	
Number of CMU ASD hits ≥ 3	
$\lvert\Delta Z_{CMU}\rvert <$ Max(3σ,8 cm)	
$\lvert\Delta X_{CMU}\rvert <$ Max(3σ,2 cm)	
No requirements on CMP stub	

CMP–only stubs

$\chi^2(X'_{CMP}) < 10$	($P_T < 10$ GeV/c)
$\lvert\Delta X'_{CMP}\rvert < 0.1$	($P_T \geq 10$ GeV/c)
$\chi^2(X_{CMP}) < 10$	($10 < P_T < 20$ GeV/c)
$\lvert\Delta X_{CMP}\rvert <$ Max(3σ,5 cm)	($P_T > 20$ GeV/c)

CMX–only stubs

$\chi^2(X'_{CMX}) < 4$ $(3 < P_T < 4 \text{ GeV/c})$

$\chi^2(X_{CMX}) < 9$ $(3 < P_T < 4 \text{ GeV/c})$

$\chi^2(Z_{CMX}) < 9$ $(3 < P_T < 4 \text{ GeV/c})$

$\chi^2(X'_{CMX}) < 9$ $(4 < P_T < 7 \text{ GeV/c})$

$\chi^2(X_{CMX}) < 9$ $(4 < P_T < 7 \text{ GeV/c})$

$\chi^2(Z_{CMX}) < 9$ $(4 < P_T < 7 \text{ GeV/c})$

$\chi^2(X'_{CMX}) < 9$ $(7 < P_T < 10 \text{ GeV/c})$

$\chi^2(X_{CMX}) < 9$ $(7 < P_T < 10 \text{ GeV/c})$

$|\Delta Z_{CMX}| < 20 \text{ cm}$ $(7 < P_T < 10 \text{ GeV/c})$

$|\Delta X'_{CMX}| < 0.05$ $(P_T > 10 \text{ GeV/c})$

$|\Delta X_{CMX}| < 3 \text{ cm}$ $(P_T > 10 \text{ GeV/c})$

$|\Delta Z_{CMX}| < 15 \text{ cm}$ $(P_T > 10 \text{ GeV/c})$

Here, ≥ 3 TDC and ASD hits is a demand that at least 3 of the 4 muon cells possess a hit for proper stub reconstruction. CMCLUS is a routine that counts the number of hits clustered around the stub including hits used to create the stub. If an interacting hadronic punch through occurs, there usually is a shower of particles emerging from the back of the calorimeter. These particles then impinge on the muon chambers resulting in a reconstructed muon stub surrounded by several other hits.

Cutting on CMCLUS < 6 helps to reject punch through. $|\Delta X|$ and $|\Delta Z|$ are the difference between the extrapolated track position and the muon stub in the x- and z-views respectively. $|\Delta X'|$ is the difference between the extrapolated track slope and the muon stub slope in the x-view. $\chi^2(X)$, $\chi^2(Z)$, and $\chi^2(X')$ are the χ^2's that follow from the above definitions.

In addition to the above cuts, there is a minimum ionizing cut on tracks with $P_T > 6$ GeV/c that requires the difference between the energy in the tower the muon propagated through minus the sum of the momenta of all CTC tracks in a cone of 0.2 around the muon track to be less than 6 GeV. This helps to kill hadronic punch through while leaving the muon signal intact.

5.1.4 Soft Muon Tagging Efficiency

The efficiency of the matching cuts described in the previous section was determined by selecting muons from J/ψ and Z^0 data sets. The efficiency from J/ψ muons was determined by studying opposite sign di-muons with an invariant mass within $\pm 2 \times 0.08$ GeV/c^2 around the J/ψ rest mass. (Di-muons with $|\Delta m| < 0.08$ GeV/c^2 are in the "signal" region, and di-muons with $0.08 < |\Delta m| < 0.16$ GeV/c^2 are in the "sideband" region.) The tagging efficiency for each muon type is then found by the following equation:

$$\epsilon = \frac{N_{pass}^{signal} - N_{pass}^{sideband}}{N_{signal} - N_{sideband}}, \tag{5.1}$$

where N_{pass}^{signal} and $N_{pass}^{sideband}$ are the total number of muon candidates of a particular type that pass all the cuts in the signal and sideband region respectively, and N_{signal} and $N_{sideband}$ are the total number of muon candidates signal and sideband region. This ratio is formed in P_T bins from $3 < P_T < 16$ GeV/c for all four muon types.

The efficiency for high P_T muons is found by searching for $Z \rightarrow \mu^+\mu^-$ candidates with $81 < m_{\mu\mu} < 101$ GeV/c^2. The first leg must be a CMU·CMP muon with $P_T >$

20 GeV/c, and pass all the SLT cuts for CMU·CMP candidates. The second leg can be any muon type with $P_T > 10$ GeV/c, and must propagate into the fiducial region described in section 5.1.1. The high P_T muon efficiency is given by $\epsilon = N^{pass}/N^{total}$. This ratio is formed in three P_T bins in the range $25 < P_T < 60$ GeV/c. Since one muon was required to pass the CMU·CMP cuts, the efficiency is calculated using information from the second leg only, unless both legs pass the CMU·CMP cuts. In this later case, information from both legs is used.

The soft lepton tagging efficiency as a function of P_T for the four muon types is plotted in figures 5.2 and 5.3. (CMU, CMP, and CMU·CMP efficiencies were taken from reference [36].) Plotted on these histograms are simple parameterizations of the muon tagging efficiencies. These parameterizations are used used in MC simulations to correctly model the true soft muon tagging efficiency.

5.1.5 Stub Finding Efficiency

In order for a muon candidate to be found, a stub must be reconstructed in the muon chambers. The stub reconstruction efficiency is used to correct Monte Carlo simulations, since QFL reconstructs muon stubs with a perfect 100% efficiency.

The muon stub reconstruction efficiency was measured from J/ψ and Z^0 decays. The stub reconstruction efficiency was found to be $(96.1 \pm 0.2)\%$ [36] for CMP stubs, $(98 \pm 1)\%$ [36] for CMU stubs, and $(98.9 \pm 1.3)\%$ for CMX stubs.

5.1.6 Fake Rate Calculation

The fake muon rate is defined as the probability that any good quality (section 5.1.2) non–muon track that is extrapolated into a muon fiducial region (section 5.1.1) will match a stub and pass all the soft muon matching cuts (section 5.1.4). The fake rates were measured by running the soft muon tagger on a huge sample of generic jet trigger data. The fake rate is defined as N^{pass}/N^{fid}, where N^{fid} is the number of good quality tracks in a particular muon fiducial region (CMU, CMP, CMU·CMP or CMX), and N^{pass} is the number of tracks linked to a muon stub(s) that pass the muon matching and minimum ionizing cuts. Histograms of the fake rates for each fiducial region in various P_T bins are shown in figures 5.4 and 5.5.

The jet trigger data used to produce the fake muon rate consists mostly of generic QCD events, and as such will contain a dearth of real muons. However, this sample does contain a small fraction of real muons from bottom and charm decays, and decays in flight, so the measured fake rate is an over estimate of the true fake rate.

The fake rate used in all MC calculations is the weighted average of all four detector fake rates. Unlike the muon tagging efficiency, the fake rate is not parameterized as a simple function of P_T, but is taken directly from the bottom plot in figure 5.4. For tracks with $P_T > 20$ GeV/c, the fake rate is take to be a constant $(0.727 \pm 0.056)\%$.

5.2 Soft Electron Identification

The electron reconstruction techniques used at CDF were designed to locate isolated high E_T electrons. Soft electrons from $t\bar{t}$ decays will tend to be non-isolated and of low energy. Hence, a new reconstruction algorithm needs to be devised if soft electrons are to be tagged. This section will describe the scheme used to identify soft electrons.

The soft electron tagging algorithm uses the Central Strip Chambers (CES) to identify showers in the CEM as coming from electrons, and the Central Pre-Radiator (CPR) to reject minimum ionizing particles. CTC tracking information, as well as calorimeter energy are used to further enhance the electron signal.

5.2.1 Soft Electron Fiducial Region

Electron candidates are required to be in the CES and CPR fiducial regions so that their positions and shower profiles will be properly measured. Tracks that propagate into the regions listed below are considered fiducial:

1. $|X_{CES}| < 22$ cm.
2. 6.22 cm $< |Z_{CES}| <$ 237.45 cm
3. Track must not propagate into the "chimney" tower.
4. Track must propagate into the CPR fiducial region as defined by the routine CPRWIR.

X_{CES} and Z_{CES} are the extrapolated track positions at the radius of the CES in the local co-ordinate system of the CES in the x- and z-views respectively.

5.2.2 Soft Electron Cuts

The cuts devised for soft non-isolated fiducial electrons were tuned to have a high tagging efficiency, while also having a low fake rate. Listed below are the cuts employed:

1. Track must have at least two axial and two stereo superlayers in the CTC.
2. Impact parameter < 0.3 cm.
3. Track extrapolates into the fiducial region described in section 5.2.1.
4. $P_T > 2$ GeV/c
5. Require minimum pulse-height in the CES: Sum the energy in five strips, $E_S(5)$, and five wires, $E_W(5)$, around the extrapolated track position. Then apply the following momentum dependent cuts.

$$E_S(5) > 0.24 \times P + 0.03 \times P^2 \quad P \leq 12 \text{ GeV/c}$$

$$E_W(5) > 0.24 \times P + 0.03 \times P^2 \quad P \leq 12 \text{ GeV/c}$$

$$E_S(5) > 0.6 \times P \quad P > 12 \text{ GeV/c}$$

$$E_W(5) > 0.6 \times P \quad P > 12 \text{ GeV/c}$$

6. The track is extrapolated to the radius of the CES, and its position must produce a close match to the position as determined from a three channel CES strip and wire cluster. The matching cuts are momentum dependent (due to shower fluctuations), and are in the x- and z-views.

$$|\Delta X^{CES-track}| < 0.7 \text{ cm for } P > 6 \text{ GeV/c}$$

$$|\Delta X^{CES-track}| < 1.82 - 0.1867 \times P \text{ cm for } P \leq 6 \text{ GeV/c}$$

$$|\Delta Z^{CES-track}| < 2.0 \text{ cm}$$

7. The shower profile must be consistent with that of electrons measured in the test beam. The five channel CES χ^2 must satisfy the following cuts in the strip and wire views:

$$\chi^2(\text{wire})/6 < 16$$

$$\chi^2(\text{strip})/6 < 16$$

8. The charge deposited in the CPR must satisfy a minimum value. Electrons tend to shower in the superconducting coil, while punch through hadrons (i.e. pions) will not. Using this information, the charged summed from three wires around the extrapolated track position, Q_{CPR}, must be greater than 2000 fC.

5.2.3 Soft Electron Tagging Efficiency

The efficiency for tagging soft electrons was determined from a sample of conversion electrons that pass the track and fiducial requirements listed in section 5.2.2, items 1–3. The formula used to derive the efficiency is given by: N^{pass}/N^{fid}, where

N^{fid} is the number of good fiducial tracks associated with conversion electrons, and N^{pass} is the number of tracks that pass the soft electron cuts listed in the above section. The first plot in figure 5.6 is a histogram of the soft electron tagging efficiency. Plotted on this histogram is a simple parameterization of the electron tagging efficiency. This parameterization is used used in MC simulations to correctly model true electron tagging efficiency.

5.2.4 Additional Soft Electron Cuts

In addition to the cuts listed in section 5.2.2, extra cuts are imposed on soft electrons in top candidate events to reduce background rates. Soft electron candidates are flagged as conversion electrons if they pass the following cuts:

$$|\Delta \cot(\theta)| < 0.06$$

$$|\Delta S| < 0.3 \text{ cm}$$

$$m_{e^+e^-} < 500 \text{ MeV/c}^2$$

$$R < 50 \text{ cm}$$

Since photons are massless, the two daughter tracks will appear parallel in the RZ view. The oppositely charged candidate conversion track will be the one that minimizes $|\Delta \cot(\theta)|$ between the candidate soft electron and any other track in the same hemisphere, where θ is the polar angle of a track. $|\Delta S|$ is the minimum separation between the soft electron and the candidate track; $m_{e^+e^-}$ is the invariant mass of the two tracks; and R is the radius at which the conversion occurred.

Along with the conversion removal cuts, the cuts listed below are also imposed:

$$0.7 < E^{EM}/P < 1.5$$

$$E^{HAD}/E^{EM} < 0.1$$

where E^{EM} and E^{HAD} are the respective energies in the EM and hadronic calorimeter tower the electron track propagated through, and P is the momentum of the track.

The E^{EM}/P cuts enforce the hypothesis that the candidate track is from an electron. The same goes for the E^{HAD}/E^{EM} cut. A study of ISAJET $m_{top} = 120$ GeV/c^2 events shows the efficiency of the above two cuts is $(72 \pm 9)\%$ for $b \rightarrow e$ electrons, and $(43 \pm 7)\%$ for $b \rightarrow c \rightarrow e$ electrons [37].

5.2.5 Soft Fake Electron Rate

The fake rate for the soft electron tagging algorithm was obtained in a fashion similar to that used to derive the fake muon tagging rate. The fake rate is defined as N^{pass}/N^{fid}, where N^{fid} is the number of tracks that pass the soft electron track and fiducial requirements listed in section 5.2.2, items 1–3, and N^{pass} is the number of fiducial tracks that pass all the cuts given in sections 5.2.2 and 5.2.4.

Unlike the soft fake muon rate, the fake electron rate is dependent on the isolation of the candidate track. For each candidate track an isolation variable, $\sum P(R = 0.2)$, is defined to be the sum of all track momenta in a cone of radius $\Delta R = 0.2$ centered around the track at the face of the calorimeter. This isolation dependence results primarily from the E^{EM}/P and HAD/EM cuts. The less isolated a track, the more likely it will have additional energy in the hadronic and EM calorimeters, which will cause the candidate to fail one or both of these requirements.

The fake rate as a function of P_T and $\sum P(R = 0.2)$ was calculated by running the electron tagger on a large sample of jet trigger data. Most of the events in this data set are QCD events, with little electron production from c- and b-quark decay or from decays in flight. The assumption is made that these data are free of primary electrons, hence, the resulting fake rates will be an over estimate of the true fake rate. Figure 5.6 displays the fake rates derived from this data sample.

In MC simulations the fake rate used is the fake rate shown in figure 5.6 for a given P_T and $\sum P(R = 0.2)$.

5.3 Stability of Fake Rates

The fake rates were calculated using a large sample of jet trigger data. However, no estimate of the systematic uncertainty on this calculation due to heavy flavor content, isolation, etc. has yet been made. This section will now estimate the systematic uncertainty for the soft electron and muon tagging algorithms.

5.3.1 Stability in Jet Triggers

The jet trigger data samples used to produce the fake lepton tagging rates are the same JET20, JET50, JET70, and JET100 samples described in section 3.3.3. The particle content, heavy flavor content, P_T spectra, isolation pathology, for these four data sets may be different.

The stability of the fake electron tagging rate was demonstrated by comparing the actual number of tags found in each of the four jet samples to the expected number. The expected number of soft electron tags was found by convoluting the track P_T spectra for each jet trigger with the fake tagging rate histograms shown in figure 5.6. The results of this study are shown in table 5.1 [38]. There is about a 10–20% variation between the expected and actual number of electron tags as a function of jet trigger. This is attributed to residual isolation dependence.

The stability of the soft fake muon rate in jet data was demonstrated by calculating a fake rate from each of the four jet triggers separately. Then each of these four fake rates is convoluted with sum of the track P_T spectrum from all four trigger samples. The results of this exercise are shown in table 5.2. The fake rates are normalized so that the fake rate derived in section 5.1.6 is 100. The jet trigger dependence, to within statistical accuracy, is less than 10%.

Table 5.1

Expected and actual number of soft electrons in each jet trigger. Δ is the percent difference between the expected and actual number of tags found. All errors are statistical.

Jet Trigger	Exp. BG tags	Number of tags	Δ (%)
JET20	436	499	14 ± 5
JET50	239	239	0 ± 6
JET70	267	260	-3 ± 6
JET100	242	185	-24 ± 7

5.3.2 Stability in Photon Sample

One of the triggers used in the 1992–3 collider run was a PHOTON16 trigger. The PHOTON16 trigger requires a fiducial CEM cluster with $E_T^{CEM} > 16$ GeV. For the purpose of this study, this sample has been divided into two subsamples: a "γ"–like and "π^0"–like sample. The γ sample is consistent with a γ+jet event event, while the π^0 sample is consistent with a $\pi^0 \rightarrow \gamma\gamma$ event. A π^0 that decays into two photons tends to have larger χ^2 in the CES strip chambers than a single photon. The reason being that the strip profile from two photons will be more diffuse and have a larger χ^2 than a single photon. Using this fact, events are considered "γ"–like if they pass the following cut:

$$(\chi^2_{strip} + \chi^2_{wire})/2 < 4, \tag{5.2}$$

where the χ^2's are described in section 3.1.3.7. If the event fails this cut, it is classified as a "π^0"–like event.

Table 5.2

Fake muon tagging rate for the four jet triggers. All fake rates shown are arbitrary. Errors are statistical only.

Jet Trigger	Fake Rate Arbitrary Units
JET20	103 ± 4
JET50	100 ± 4
JET70	104 ± 4
JET100	95 ± 2
Total	100 ± 2

The results of this exercise are shown in table 5.3. To within statistical error, there appears to be a 10% systematic effect due to event topologies.

5.3.3 SLT Systematic Uncertainty

Based on the above studies, the following systematic and statistical uncertainties are assigned to the SLT algorithms:

soft muon tagging algorithm:	±10%
soft electron tagging algorithm:	±15%

5.4 Heavy Flavor Search with SLT

A search for *b*- and *c*-quarks in the inclusive high E_T electron data set (sec-

Table 5.3

Electron and muon tagging rates in the PHOTON16 trigger sample.

Event Type	Expected BG (μ)	Tags (μ)	Expected BG (e)	Tags (e)
γ	71	78	35	38
π^0	106	88	52	68
$\gamma + \pi^0$	177	166	87	106

tion 3.1.1) was carried out to demonstrate that the SLT could tag leptons from heavy quark decay. To verify that b's are being tagged, events with high quality electrons ("golden" electrons) are selected, and the SLT applied to tracks in the hemisphere opposite that of the golden electron. This should lead to an excess of soft lepton tags over that expected from fake tags alone, since b's are usually produced in back-to-back $b\bar{b}$ pairs. One of these b's decays into the golden electron, and the other b decays some fraction of the time into additional leptons.

To insure the above test is tagging a true excess, the soft lepton tagger was also run on events possessing a high E_T electron associated with a good quality photon conversion ("golden" conversion). There will be a dearth of b's in events with conversions, since it is not likely a high E_T photon and $b\bar{b}$ pair will be present in the same event. The soft lepton search is carried out in the hemisphere opposite to the conversion pair. The result of the soft lepton search in the golden conversion and electron samples are listed in tables 5.4 and 5.5 respectively.

The results of this study clearly show that b- and c-quarks are being tagged. There is no excess of SLT's over the expected number of tags in the golden conversion sample (a control sample), but a large excess of SLT's in the golden electron sample. Moreover, in the golden electron sample there is an excess of events where the charge of the soft lepton is opposite that of the golden electron. This is to be expected in $b\bar{b}$ events.

5.5 Additional Soft Lepton Cuts

In addition to the fiducial and quality cuts applied to soft electrons and muons, there are extra cuts applied in the $t\bar{t}$ search to help kill unwanted Drell–Yan and $b\bar{b}$ events. Drell–Yan events are squelched by rejecting e^+e^- and $\mu^+\mu^-$ pairs where one lepton passes the high E_T lepton cuts, and the other lepton passes the SLT cuts and the following P_T dependent isolation requirements:

E_T (in cone of ΔR=0.4)	< 3 GeV	$P_T <$20 GeV/c
E_T (in cone of ΔR=0.4)$/P_T^{lepton}$	< 0.1	$P_T \geq$20 GeV/c

$b\bar{b}$ events are partially removed by rejecting l^+l^- events with an invariant mass less than 5 GeV/c^2, where one lepton passes the high E_T lepton cuts and the other lepton passes the soft lepton requirements. The leptons can be different species since this cut is designed to eliminate sequential decays of b-quarks.

5.6 SLT in Monte Carlo Data

Unlike real data where a track is either tagged as a soft lepton or not, a track in a MC event is assigned a probability of being a real and/or fake tag. To obtain the true tagging probability for a track associated, say, with a lepton from a b-quark in a $t\bar{t}$ event, follow the steps below. If the track fails any of these requirements, the true tagging probability for that track is zero:

1. The track must pass the track quality cuts given in section 5.2.2 for electrons or section 5.1.2 for muons.
2. The track must extrapolate to a fiducial area listed in section 5.2.1 for electrons or section 5.1.1 for muons. (In the case of muons, the fiducial area is determined by the stub(s) associated with the muon track. If the muon track is not associated with a stub, the tagging probability is zero.)
3. The track must pass all soft lepton calorimeter requirements (i.e., isolation, E/P, HAD/EM, etc).
4. Assign a tagging probability to the track using the tagging efficiency parameterizations described for electrons in section 5.2.3 or for muons in section 5.1.4.
5. QFL reconstructs tracks with a 100% efficiency. This is not the case for real tracks. A study of the CTC tracking efficiency was done, and it was found to be $(96 \pm 1.7)\%$ efficient for tracks embedded in jets [39]. To account for QFL's track reconstruction over efficiency, the probability found in the previous step is multiplied by 0.96.
6. If the candidate is a muon, multiply the above probability by the appropriate stub finding efficiency given in section 5.1.5. If the candidate is an electron, multiply the above probability by 0.98 to account for the conversion electron removal over efficiency.
7. The track must not fail the Drell–Yan or $b\bar{b}$ cuts given in section 5.5.

To assign a fake tagging probability to a track, follow the steps below. If a track fails any of these cuts, the fake tagging probability for that track is zero:

1. The track must pass the electron or muon track quality cuts.
2. The track must extrapolate to an electron or muon fiducial area.
3. Assign a probability to the track using the fake electron or muon probability

derived in sections 5.2.5 and 5.1.6 respectively.

4. Multiply the above probability by 0.96 to account for QFL's tracking over efficiency.
5. If the track is a fake electron candidate, multiply the above probability by 0.98 to account for the conversion electron removal over efficiency.
6. The track must not fail the Drell–Yan or $b\bar{b}$ cuts given in section 5.5.

The above recipes yield tagging probabilities for individual tracks. The probability the event will have at least one tag, fake or real, is given by:

$$P^{tag} = 1 - \prod_i (1 - p_i^{true}) \times \prod_i (1 - p_i^{fake}), \tag{5.3}$$

where p^{true} and p^{fake} are the real and fake tagging probabilities as for each track, and P^{tag} is the probability the event will have at least one tag.

In $t\bar{t}$ events, leptons produced directly from top quarks ($t \rightarrow 1$), taus ($t \rightarrow \tau \rightarrow l$), quarks from W's ($W \rightarrow q\bar{q} \rightarrow l$), and b-quarks ($t \rightarrow b \rightarrow \ldots \rightarrow l$) are considered real soft leptons, and assigned a real lepton tagging probability. All other tracks are assigned both fake electron and muon tagging probabilities.

The tagging efficiencies for MC background processes (i.e., W+jets) are calculated using a combination of real and fake tagging rates as described above for $t\bar{t}$ events. Which tracks are assigned a real or fake tagging probability in a particular MC background process will be divulged in the background calculation chapter.

Table 5.4

Expected and actual number of SLT's in the golden conversion sample. All uncertainties are systematic uncertainties estimated in section 5.3.3

Lepton Type	Estimated BG	Tags
e	27 ± 4	29
μ	53 ± 5	53

Table 5.5

Expected and actual number of SLT's in the golden electron sample. All uncertainties are systematic uncertainties estimated in section 5.3.3. OS refers to events where the charge of the soft lepton is opposite the golden electron, SS are events where the charge of the soft lepton is the same as that of the golden electron.

Lepton Type	Estimated BG	SS Tags	OS Tags	Total Tags	Excess
e	33 ± 5	19	41	60	27
μ	65 ± 7	52	65	117	52

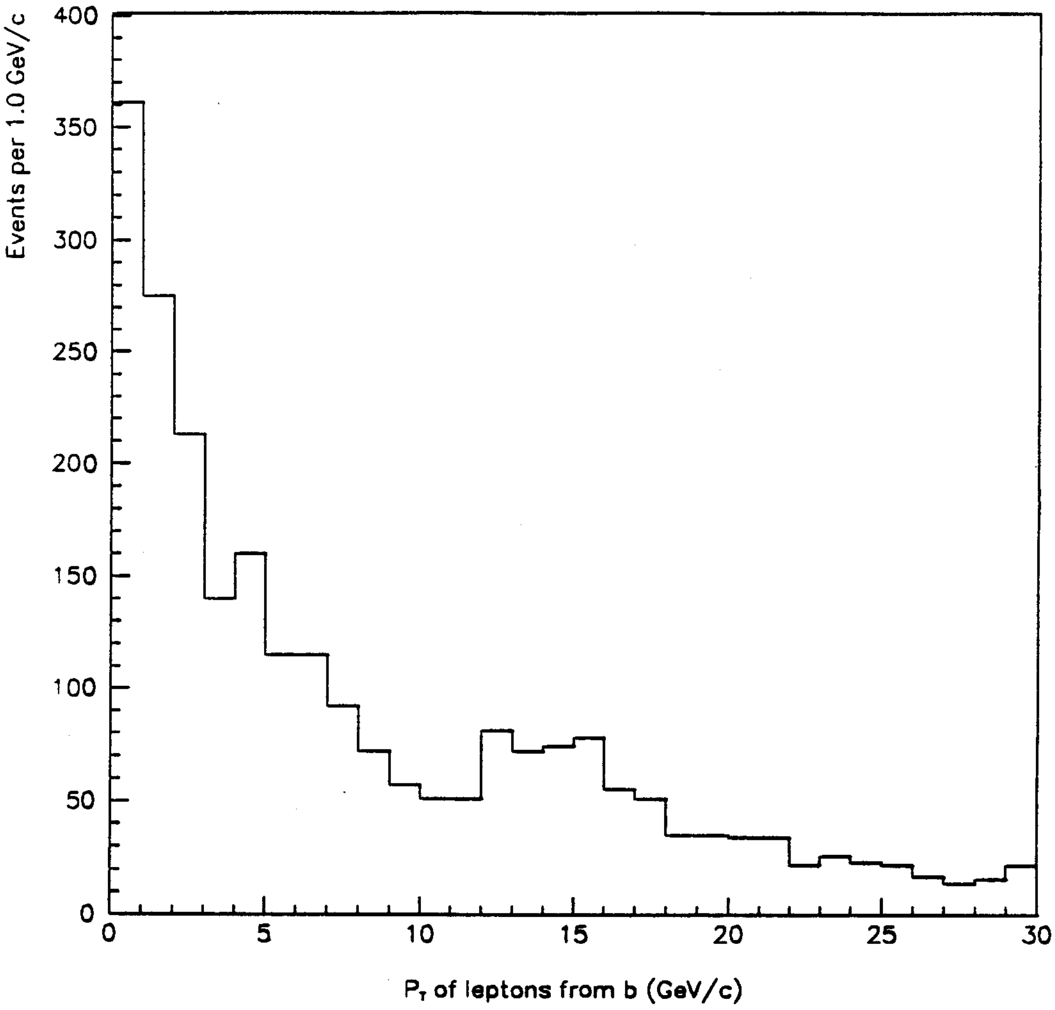

Figure 5.1

Lepton P_T spectra from b-quark decay in $t\bar{t}$ events with $m_{top} = 160$ GeV.

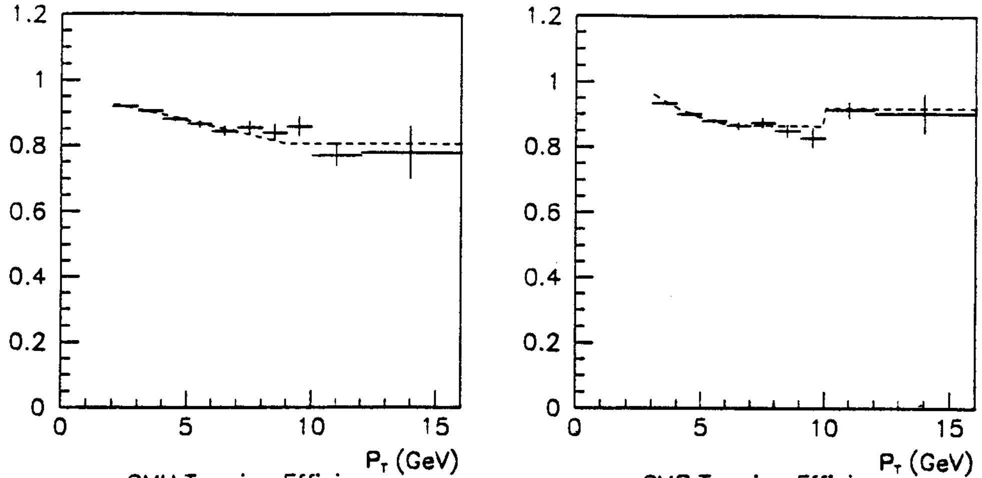

CMU Tagging Efficiency

CMP Tagging Efficiency

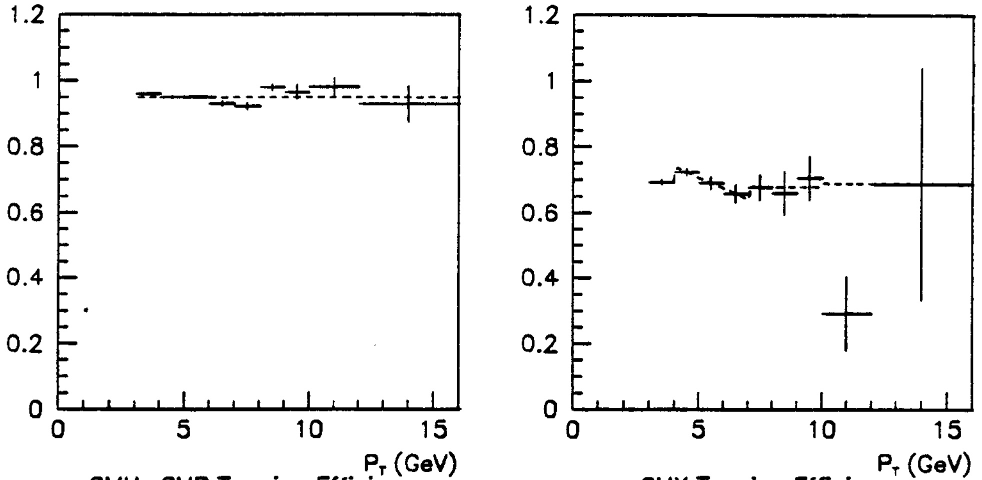

CMU–CMP Tagging Efficiency

CMX Tagging Efficiency

Figure 5.2

Soft muon tagging efficiencies measured with J/ψ's. The dotted curves are simple parameterizations of the muon tagging efficiencies.

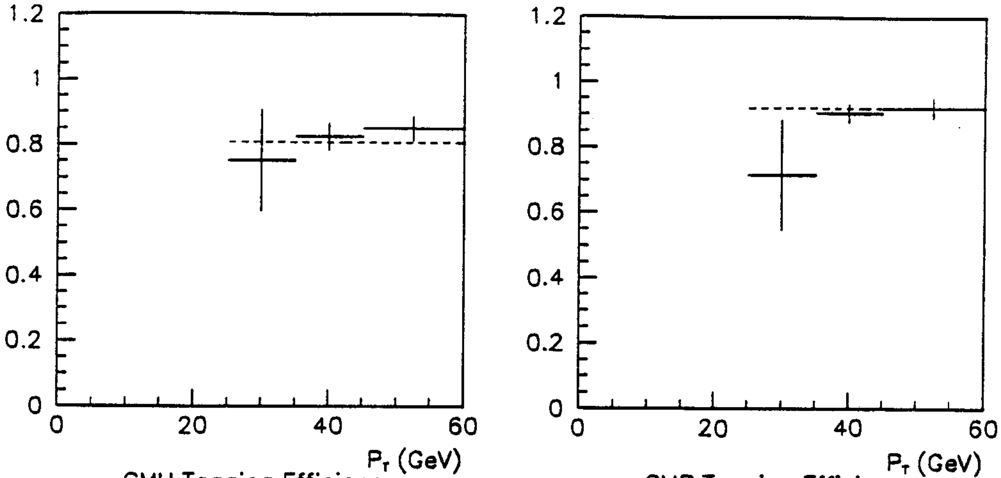

CMU Tagging Efficiency

CMP Tagging Efficiency

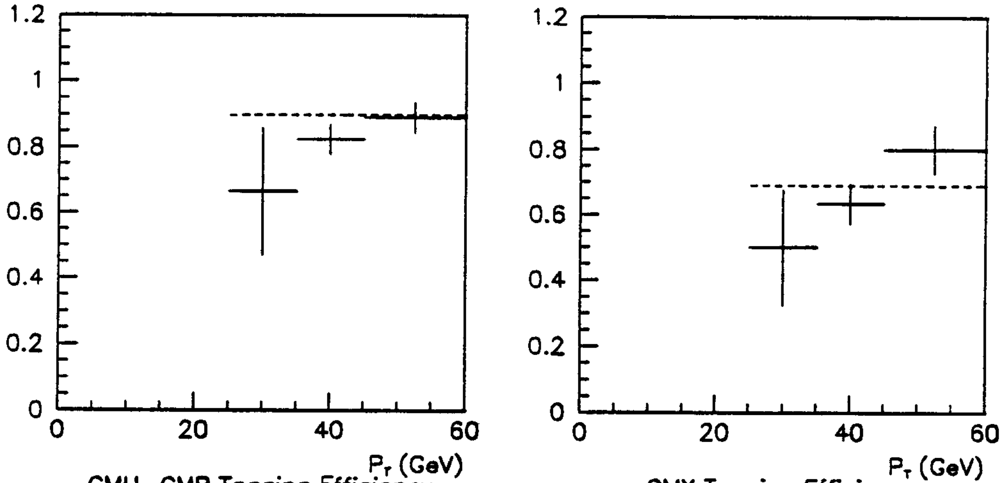

CMU–CMP Tagging Efficiency

CMX Tagging Efficiency

Figure 5.3

Soft muon tagging efficiencies measured with Z's. The dotted curves are simple parameterizations of the muon tagging efficiencies.

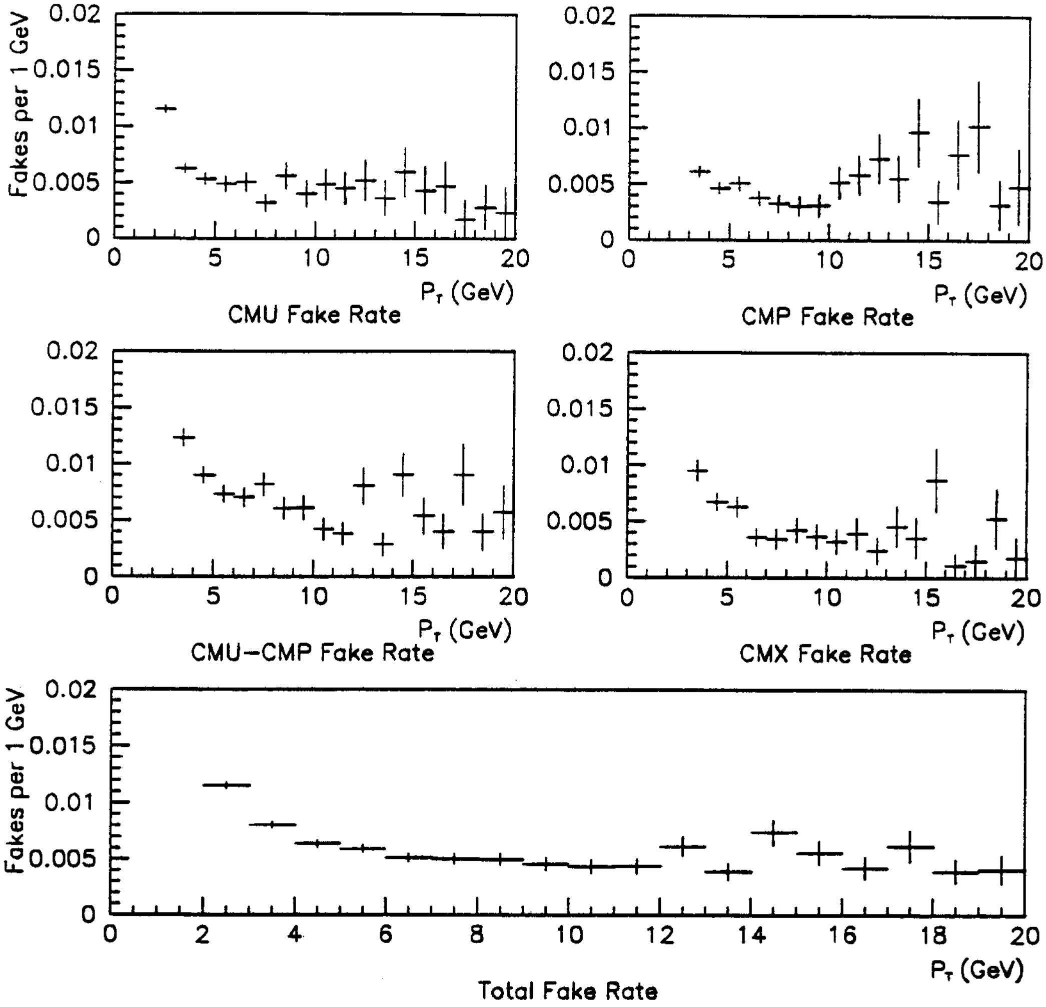

Figure 5.4

Soft fake muon tagging rate, low P_T range.

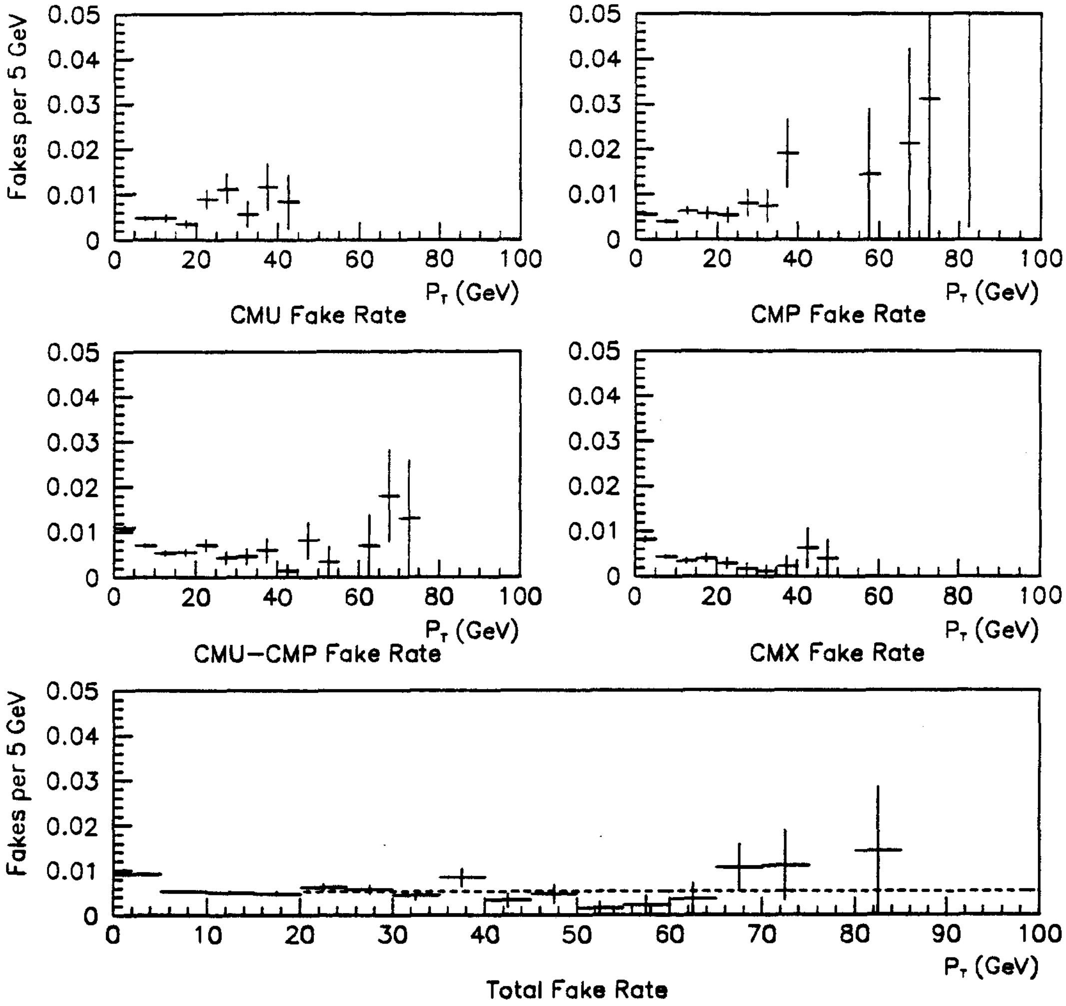

Figure 5.5

Soft fake muon tagging rate, high P_T range.

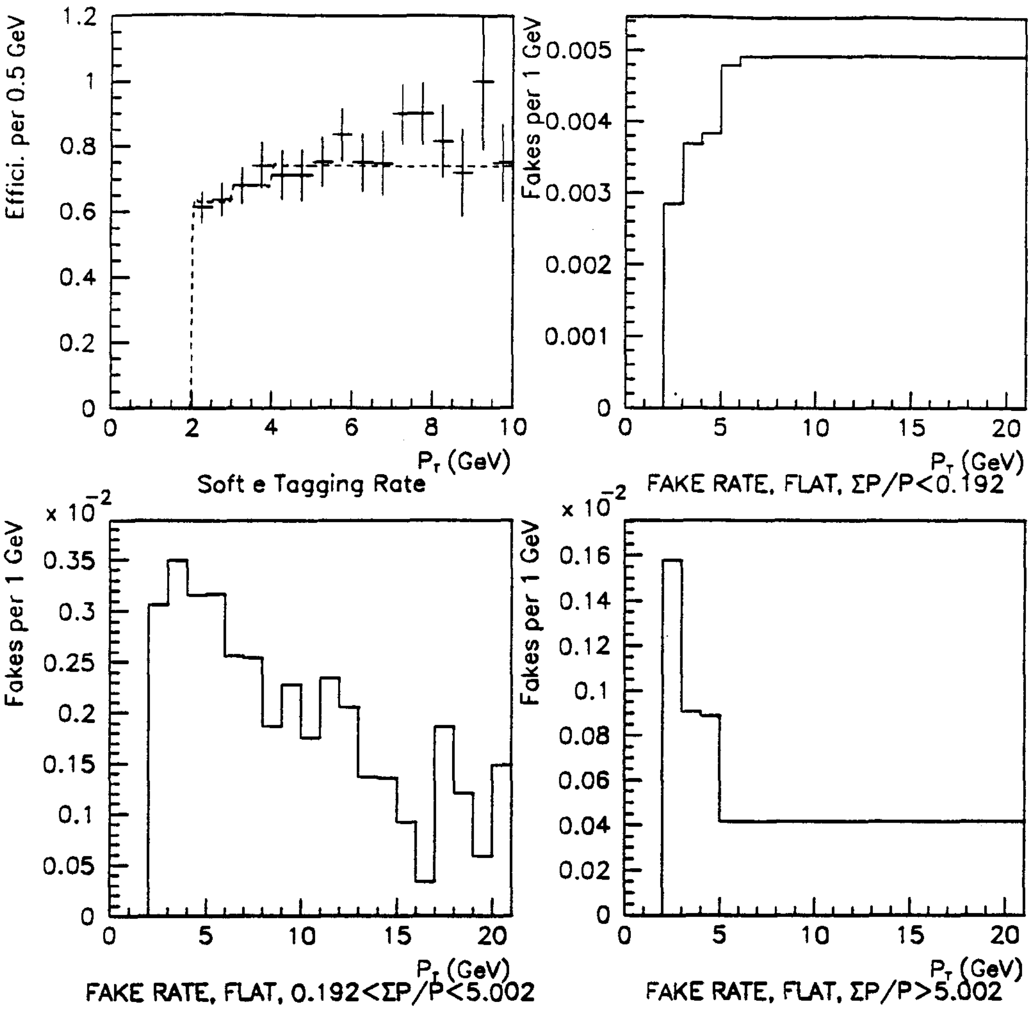

Figure 5.6

Soft electron tagging and fake rates. The upper right plot is a histogram of the electron tagging efficiency. The dashed line is a parameterization of the tagging efficiency. The remaining three histograms are plots of the soft electron tagging rate as a function of P_T for three different $\sum P/P^e$ ranges.

6. KINEMATIC SELECTION

In chapter 3, the cuts applied to select good quality high E_T leptons were given. And in chapter 5, algorithms for selecting additional soft leptons in $t\bar{t}$ events were described. This chapter will deal with the last major event selection criteria used to reject background processes: kinematical cuts. There are three kinematical cuts applied to data to enhance the top signal to background ratio: $\not{E}_T$ cut, jet energy cuts, and a cut on the total E_T of the event (aka $\sum E_T$). These cuts will be reviewed, as well as the gain in the signal to background ratio when corrected variables (i.e., jet E_T, $\not{E}_T$, etc) are used over their raw values.

6.1 $\not{E}_T$ Cut

The method for calculating the corrected missing E_T was described in section 4.7. The motivation behind the $\not{E}_T$ cut is to select events that have a significant transverse energy imbalance due to high E_T neutrinos. Since this top search is carried out in the lepton+jets channel, where one W decays leptonically into a high E_T lepton–neutrino pair, a cut on $\not{E}_T$ is appropriate as it will greatly reduce non–neutrino containing background processes. Figure 6.1 is a plot of $\sum P_T^{\nu}$ in ISAJET $m_{top} = 160$ GeV/c^2 $t\bar{t} \rightarrow l\nu$ + jets events. The P_T distribution in this plot suggests that events should have $\not{E}_T > 20$ GeV to be considered as $t\bar{t}$ candidates.

6.2 Jet E_T Cuts

A distinctive feature of $t\bar{t}$ events where one W decays leptonically and the other decays hadronically is the presence of a high P_T lepton and four jets. Two jets are from the decay of the b-quarks, and two from the W that decays hadronically. Selecting candidate $t\bar{t}$ events with three or more jets is an extremely powerful method used to reduce the background rate without undue loss of $t\bar{t}$ events.

The jet energy cuts should be picked to reduce the W+jets background as much as possible without significantly attenuating the top signal. The jet energies used are corrected jet energies described in section 4.6. Figure 6.2 displays the four highest jet E_T's with $|\eta_{det}| < 2.0$ in a cone of $\Delta R = 0.4$ for the m_{top}=160 GeV/c^2 ISAJET MC data set and for the VECBOS W+jets data sets. (The VECBOS W+jets data sets were described in section 4.4.2.) All events in this plot were required to pass the high E_T lepton cuts and the $\not{E}_{\rm T} > 20$ GeV cut. The third jet in W+jets events is strongly peaked below approximately 25 GeV, while the the third jet in $t\bar{t}$ events is rather flat from 20–50 GeV. Therefore, the minimum E_T requirement for the third jet is set at 25 GeV. There is no such striking feature in the first and second highest E_T jets, so the minimum E_T's for the first and second highest E_T jet with $|\eta_{det}| < 2.0$ are set at 30 and 25 GeV respectively. An event is classified as having more than three jets if there are additional jets with $E_T > 20$ GeV and $|\eta_{det}| < 2.0$. (There is no requirement on a fourth jet as this cut reduces the $t\bar{t}$ acceptance by approximately 25% for m_{top} = 160 GeV/c^2.)

6.3 $\sum E_T$ Cut

As revealed in the introduction of this chapter, a variable called $\sum E_T$ is constructed to reduce the W+jets background rate even further. $\sum E_T$ is defined below:

$$\sum E_T \stackrel{\rm def}{=} \sum^{n_{jets}} E^{cone}_{T_i} + \not{E}_{\rm T}{}^{cor} + \sum^{prime} E^{e}_{T_i} + \sum^{n_\mu}(P^{\mu}_{T_i} - E^{\mu}_{T_i}) + UCE \qquad (6.1)$$

Here E^{cone}_T is the corrected jet E_T in the cone (i.e., no out–of–cone correction is made). E^{cone}_T summed over all corrected jets at all η. $\not{E}_{\rm T}{}^{cor}$ is the corrected $\not{E}_{\rm T}$ described in section 4.7. $\sum^{prime\,e} E^{e}_{T_i}$ is the sum of corrected E_T from all primary isolated electrons with $E_T > 20$ GeV. $\sum^{n_\mu}(P^{\mu}_{T_i} - E^{\mu}_{T_i})$ is the sum of beam–constrained P_T minus the E_T deposited in the tower the muon propagated through for all primary and SLT muons. (See section 3.4 for the definition of E^{μ}_{T}.) UCE is the scalar sum of unclustered E_T.

Acceptance as a function of $\sum E_T$ for the VECBOS W+jets and ISAJET $m_{top} =$ 140, 160, and 180 GeV/c^2 MC data after the high P_T lepton cut, $\not{E}_T$>20 GeV cut, (30,25,25) GeV jet E_T cut, and SLT cut is shown in figure 6.3. In this analysis, a minimum $\sum E_T$ of 250 GeV is imposed. This cut reduces the $t\bar{t}$ acceptance by less than 3%, while the W+jets rate is reduced by 28%.

6.4 Acceptance Gain Using Corrected Variables

The variables E_T^{jet} and $\not{E}_T$ (and indirectly $\sum E_T$) have been tuned on $t\bar{t}$ MC data. $t\bar{t}$ candidate events are selected by cutting on these corrected variables, not their raw values. It is not obvious that this extra effort will provide any added background rejection. In order to determine the change in the signal to background ratio using uncorrected vs. corrected variables, a Monte Carlo simulation was performed where the uncorrected jet E_T and $\sum E_T$ cuts were chosen so as to have approximately the same $t\bar{t}$ acceptance as the corrected variables. If there is any added background rejection when using corrected energies, the W+jets rate will be smaller than with the uncorrected values.

The minimum corrected jet E_T's listed in section 6.2 are 30, 25, and 25 GeV for the three highest E_T jets with $|\eta_{det}| < 2.0$. The corresponding minimum uncorrected E_T cuts are approximately 22.5, 17.5 and 17.5 GeV (Jets with uncorrected $E_T \approx 20$ GeV have ~7.5 GeV added to them.) The corrected and uncorrected $\not{E}_T$ cut are both set to 20 GeV, as this is the standard cut value.

Table 6.1 lists the number of $t\bar{t}$ and W+jets events with a soft lepton tag expected

Table 6.1

Difference in significance using corrected vs. raw variables. Significance is defined as $(\frac{n_{top}}{\sqrt{n_{W+jets}}})$. The number of tags listed are the number expected in 19.3 pb^{-1}

$\sum E_T$ (GeV) COR (RAW)	m_{top} = 160 GeV tags COR (RAW)	W+3 and 4 jet tags COR (RAW)	Significance COR (RAW)
0 (0)	2.26 (2.19)	2.08 (2.20)	1.57 (1.48)
250 (220)	2.19 (2.15)	1.49 (1.70)	1.79 (1.65)
300 (270)	1.82 (1.78)	0.81 (0.87)	2.02 (1.91)

in the 1992–3 data using the ISAJET m_{top} = 160 GeV/c^2 and VECBOS W+3 and 4 jet MC data sets respectively. 'Significance' in this table is defined as $\frac{n_{top}}{\sqrt{n_{W+jets}}}$. This table shows that there is an advantage in using corrected energies over their raw values. Therefore, the corrected $\not{E}_T$ and E_T^{jet} values will be used in selecting $t\bar{t}$ candidate events.

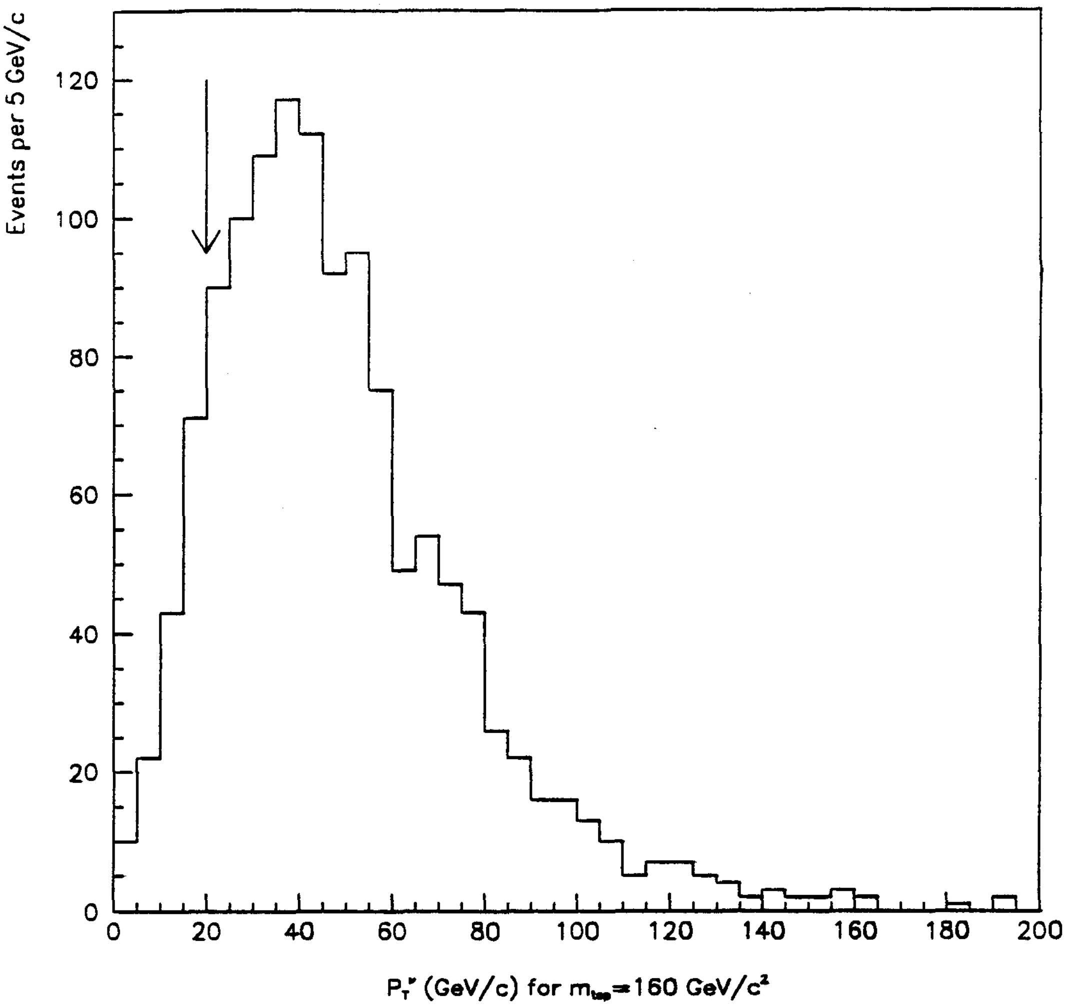

Figure 6.1

Neutrino P_T in $t\bar{t} \rightarrow l\nu$ + jets events with m_{top} = 160 GeV/c^2. P_T is the P_T of all neutrinos in an event.

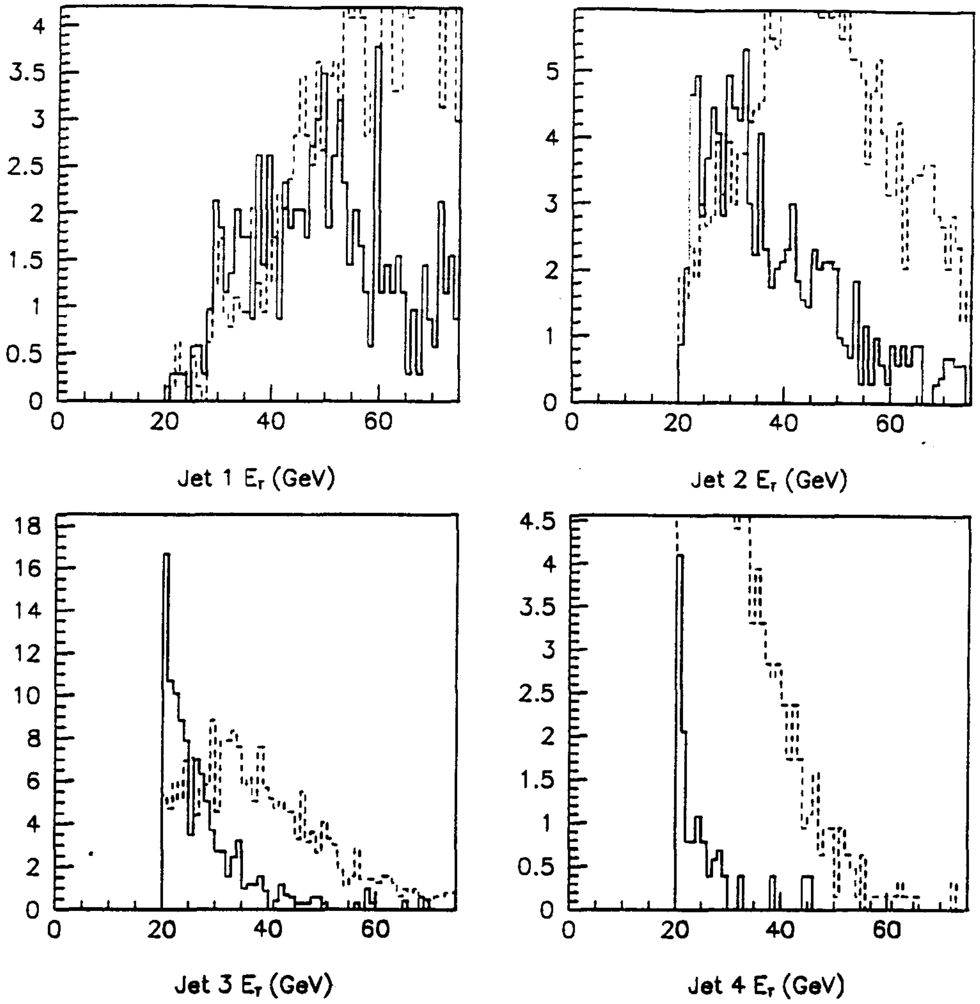

Figure 6.2

Jet E_T's for W+jets and $t\bar{t}$ events. The corrected jet E_T's for the four highest E_T jets with $|\eta_{det}| < 2.0$ in a cone of $\Delta R = 0.4$. W+3 and 4 VECBOS MC samples are the solid lines, and M_{top}=160 GeV/c^2 is shown as a dashed line. The VECBOS sample has been normalized to 19.3 pb^{-1}, the $t\bar{t}$ sample is normalized to 193.0 pb^{-1}.

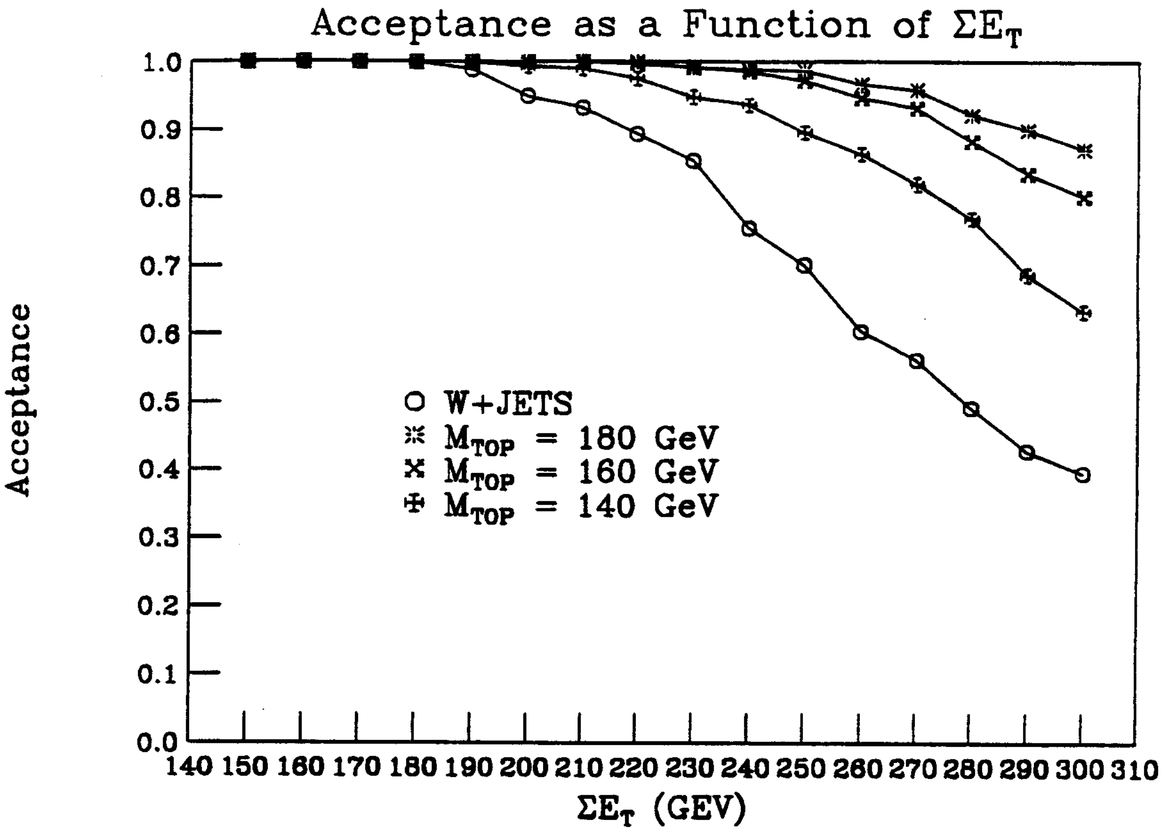

Figure 6.3

Acceptance as a function of $\sum E_T$ for various processes. All events must pass the lepton, $\not{E}_T$, jet E_T, and SLT cuts.

7. SIGNAL AND BACKGROUND ESTIMATES

Several background (BG) processes (and possibly $t\bar{t}$) contribute to the observed signal after all cuts have been applied. The purpose of this chapter is to calculate the expected BG rate from all processes that could mimic $t\bar{t} \rightarrow l + \nu$+jets decay. The main BG in this top search is W+jets events, but di-bosons, $b\bar{b}$ and $c\bar{c}$, Drell–Yan, $Z \rightarrow \tau\tau$, and $W + c$ events also contribute to the BG rate. This chapter will explain how the expected background and signal rates are estimated, and what those estimated rates are in 19.3 pb^{-1}. Unless otherwise noted, the probability that an event will have a soft lepton tag is determined as outlined in section 5.6.

7.1 Background Estimates

7.1.1 Di-Boson Backgrounds

Di-bosons—WW, WZ, and ZZ—are a small background in the top search, but they should be taken into account. These backgrounds were generated with ISAJET and simulated with QFL, and were described in section 4.2. The cross section used was the NLO σ calculated by Ohnemus et al. [28]. The cross section, integrated luminosity, and expected number of tags in 19.3 pb^{-1} for each process are shown in table 7.1. The uncertainties on the cross section are 30% for the difference between the LO and NLO calculation, 30% for the ISAJET modeling of jet multiplicity, and 3.5% for the luminosity. These uncertainties are added in quadrature. The tagging probability used for electrons and muons produced via W or Z decay is the real e and μ tagging probability. All other particles are tagged using the lepton fake probability.

Table 7.1

The number of di–boson events expected in 19.3 pb^{-1}. The systematic uncertainties are described in section 7.1.1.

Process	σ (pb)	$\int \mathcal{L}\, dt$ (pb^{-1})	Expected tags in 19.3 pb^{-1}
WW	9.39	1065	0.069 ± 0.029
WZ	2.56	3906	0.025 ± 0.011
ZZ	1.08	9259	0.011 ± 0.005
Total	-	-	0.105 ± 0.031

7.1.2 $Z \rightarrow \tau\tau$ Background

ISAJET was run to produce 486.6 pb^{-1} of $Z \rightarrow \tau\tau$ events which were then simulated with QFL. The expected background rate in 19.3 pb^{-1} from this process is 0.023 ± 0.007 events. The uncertainty is 30% for the ISAJET modeling of the jet multiplicity, and 3.5% for the luminosity. The tagging probability used for electrons and muons produced from Z decay is the real e and μ tagging probability. All other particles are tagged using the lepton fake probability as described in section 5.6.

7.1.3 Drell–Yan Background

Drell–Yan events are flagged as outlined in section 5.5. The Drell–Yan background rate in the 1992-3 collider run was estimated in to be < 0.12 events at the 90% confidence level in 19.3 pb^{-1} [33]. This rate was estimated for events with ≥ 3 jets with uncorrected jet $E_T > 15$ GeV. However, with the higher jet energy cuts and $\sum E_T$ cut used in this analysis, the estimated Drell–Yan background rate will be lower. The Drell–Yan background rate is estimated to be half the above value or 0.06 ± 0.06 events.

7.1.4 $b\bar{b}$ and QCD Backgrounds

The fraction of $b\bar{b}$ and QCD events in the W sample can be estimated directly from the inclusive electron and muon data [40]. A plot of $\not{E}_T$ vs. border energy (sections 3.1.3.12 and 3.2.2.7) from the above data sets is split into four regions as shown in the following figure:

Region 1: BE <2 GeV and $\not{E}_T$ <10 GeV

Region 2: BE >5 GeV and $\not{E}_T$ <10 GeV

Region 3: BE <5 GeV and $\not{E}_T$ >20 GeV

Region 4: BE <2 GeV and $\not{E}_T$ >20 GeV

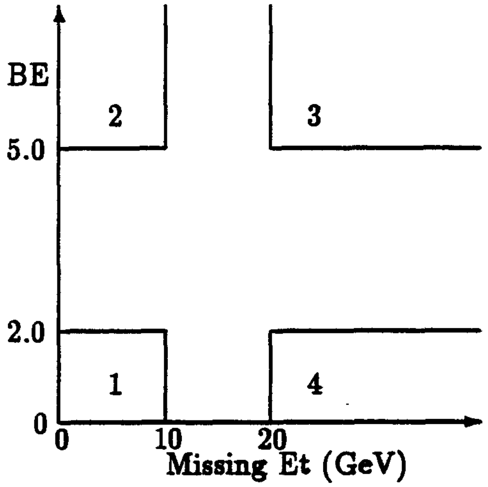

Regions 1, 2, and 3 contain mostly background, while Region 4 is the W signal region. Using the assumption that $\not{E}_T$ and border energy are uncorrelated, the following relation can be formed:

$$\frac{B_4}{B_1} = \frac{B_3}{B_2}, \tag{7.1}$$

where B_i is the number of $b\bar{b}$ and QCD background events in Region i. (The assumption that $\not{E}_T$ and border energy are uncorrelated has been demonstrated [4, 40]. This is a consequence of the fact that the parts of a BG event that contribute BE and $\not{E}_T$ are independent.) Under the assumption that the number of background events is the same as the actual number of events in these regions, the following equation for the estimated number of $b\bar{b}$ and QCD events in Region 4, the W region, is:

$$N_{BG} = \frac{N_1 N_3}{N_2}, \tag{7.2}$$

where N_{BG} is the estimated number of background events in Region 4, and N_i is the number of events in Region i. The estimated fraction of $b\bar{b}$ and QCD events in the W sample is then $f_{BG} = N_{BG}/N_4$. Table 7.2 lists the estimated fraction of $b\bar{b}$ and QCD events for six different jet requirements. There is not much variation in f_{BG} as the jet requirements change, so f_{BG} is taken to be $(20 \pm 5)\%$. Next, the estimated number of tagged $b\bar{b}$ and QCD events in Region 4 needs to be estimated. This is done with the five step process listed below:

1. Sum the number of events with one or more soft lepton tags in Region 1. Call this L_{tot}. (Reject all events in Region 1 that are flagged as Drell–Yan events.)
2. The expected number of fake soft lepton tags in Region 1 is calculated as described in sections 5.1.6 and 5.2.5. Call this L_{exp}.
3. The real number of leptons in Region 1 is then $L_1 = L_{tot} - L_{exp}$.
4. The tagging rate in Region 1 is $R_{tag} = L_1/N_1$.
5. The estimated number of $b\bar{b}$ and QCD events in Region 4 is $L_b = N_4 f_{BG} R_{tag}$.

R_{tag} has been estimated for three jet requirements, and the results listed in table 7.3. From this table, R_{tag} is taken conservatively to be $(1.0 \pm 0.7)\%$,

Finally, the expected number of $b\bar{b}$ and QCD events expected in this analysis is: $L_b = 24 \times 0.20 \times 0.01 = 0.05 \pm 0.04$, where $N_4 = 24$ events pass all $t\bar{t}$ selection cuts, except the soft lepton cuts. (See section 8.1.)

7.1.5 $W + c$ Background

The calculation of this background follows closely the method devised by the SVX group, and is described in detail in [41]. $W + c$ is produced by the flavor excitation processes $g + d \rightarrow W + c + X$ and $g + s \rightarrow W + c + X$ [42]. This background calculation begins by finding the fraction of W events containing a c-quark, F_{wc}. Reference [41] used HERWIG [35] and VECBOS MC generators to determine the expected fraction of W + jets events produced by this process. The result of this exercise is $F_{wc} = (8.0 \pm 1.5)\%$ in $W+ \geq 3$ jet events. The uncertainty on F_{wc} is derived by varying the input structure functions. Next, the efficiency for tagging a soft lepton from the c-quark decay, ϵ_c, is found by running ISAJET $W + c$ events through QFL and searching for tags. This efficiency is $(1.52 \pm 0.22)\%$, where the uncertainty is statistical only. Finally, the expected number of $W + c$ tags in the 1992–3 run is:

$$N_{wc} = 0.80 \times N_4 \times F_{wc} \times \epsilon_c \times (1.11 \pm 0.03). \tag{7.3}$$

N_{wc} is the expected number of $W+c$ events, 0.80 reflects the fact that about $(80 \pm 5)\%$ of "W" events are really $b\bar{b}$ and QCD events. (See section 7.1.4.) The factor 1.11 is a correction to account for the fact that F_{wc} was calculated at the parton level. $N_4 = 24$ is the number of W+jets events that survive all $t\bar{t}$ cuts without a SLT listed in chapter 8.

The result of this calculation is $N_{wc} = 0.026 \pm 0.005 \pm 0.004$. The errors are the systematic (structure functions) and statistical errors.

7.1.6 W+Jets Background

The W+jets background is the largest and most important background in the top search and is calculated directly from the data, not from the VECBOS MC data (section 4.4.2). The W+jets background rate is estimated by calculating how many tagged events would be expected in the 24 events that pass pass all the $t\bar{t}$ selection cuts (except the soft lepton cuts) enumerated in section 8.1. The expected number of tagged events not only contains a contribution from fakes, but a contribution from real leptons from non-$t\bar{t}$ heavy-quark decay. The assumption is made that the heavy-flavor content in W+jets events is less than or equal to that in the generic jet trigger sample. (This is a valid assumption. In the generic jet trigger data—from which the SLT fake rate was derived—heavy quarks can be produced in three different processes: (1) direct production (i.e., $gg \rightarrow b\bar{b}$); (2) gluon–splitting processes, where a final state gluon branches into a heavy quark pair; (3) flavor excitation (initial state gluon–splitting). In the generic jet sample, the gluon–splitting process accounts for 65% (75%) of the produced $b\bar{b}$ ($c\bar{c}$) pairs. In W+jets events, $b\bar{b}$ and $c\bar{c}$ are only produced via gluon–splitting [43]. In addition, VECBOS predicts a fraction of gluon jets in W+jets events that is smaller than generic jet trigger events by a factor of 1.5 to 2. Therefore, the tagging rate calculated from the generic jet sample will provide an overestimate of the W+jets background.)

The expected number of tagged W+jets events estimated from the data is 1.54 ± 0.15, where the error due to the systematic uncertainty of the fake tagging rate. This tagging rate will be an even more conservative estimate if $t\bar{t}$ is present in the data as there is no a priori procedure to remove this "background" from the expected W+jets tagging rate.

This calculation has also been performed using the VECBOS W+3 and 4 jet data sets listed in section 4.4.2. The expected number of tagged events in 19.3 pb^{-1} is $1.49 \pm 0.19^{+0.59}_{-0.36} \pm 0.05 \pm 0.12$, where the first uncertainty is statistical, the second is from the energy scale, the third is from the luminosity, and the fourth is due to the systematic uncertainty of the fake tagging rate.

The QCD scale, Q^2, used in generating the VECBOS data sets was picked to be

$Q^2 = < P_T^{jets} >^2$ so as to produce the most pessimistic (highest) cross section expected for this background. That fact that the expected number of tagged W+jets events as calculated from the data is higher than the pessimistic number expected from VECBOS lends credence to the claim that this calculation is not an underestimate.

7.1.7 Summary of Backgrounds

Table 7.4 lists the expected number of background events in the 1992-3 collider run.

7.2 $t\bar{t}$ Rate in the 1992-3 Collider Run

ISAJET $t\bar{t}$ events were simulated with QFL and required to pass the same cuts as the real data. Only leptons from t- and b-quarks, W's, and τ's can be tagged as primary leptons. Electrons and muons from t- and b-quarks, W's, and τ's, are tagged using the real soft lepton tagging probability derived in chapter 5. All other tracks not coming from the above particles are not counted as potential fake tags. The reason for omitting the fake tag contribution in MC $t\bar{t}$ samples is that this background has been computed directly from the event sample itself in section 7.1.6. If there is any $t\bar{t}$ in the final sample, it will contribute to the W+jets background calculation. Studies on ISAJET $t\bar{t}$ MC data show that approximately 25–30% of the $t\bar{t}$ tagging rate is due to fake tags.

Table 7.5 lists the expected number of $t\bar{t}$ events in the 1992-3 run.

7.2.1 Systematic Uncertainty in Top Acceptance

The large size of the ISAJET $t\bar{t}$ samples ensures a small statistical uncertainty for the MC data sets. However, there are systematic uncertainties in the top acceptance that need to be estimated. The sources of the systematic uncertainties are listed below:

1. Lepton efficiencies: The uncertainty on the primary high P_T lepton efficiency as measured with leptons from Z^0's was found to be ~5%. The systematic uncertainty for reconstructing soft muons in lepton+jets events is taken to be 5%, and is based on efficiency measurements. The soft electron efficiencies can be broken down into two components: (i) the instrumental efficiency of the CES–CPR–dE/dx cuts; (ii) the efficiency of the implicit isolation requirements (E/P and Had/EM). The systematic uncertainty for these two components were estimated to be on the order of 5% and 10% respectively [33].
2. Energy scale: The systematic uncertainty in the top acceptance due to the uncertainty in the jet energy was modeled by varying the jet energies by ±10%. ($\sigma(E_T^{jet}) = 0.1 \times E_T^{jet}$.) The results are presented in table 7.6.
3. Initial state radiation: ISAJET produces initial state (IS) gluon radiation in $t\bar{t}$ events. The sensitivity of the top acceptance to IS radiation was modeled using MC data produced by ISAJET with IS radiation turned off. The $t\bar{t}$ acceptance decreased by ~15%. The systematic uncertainty is taken to be 7% or half the change in acceptance.
4. b- and c- semileptonic branching ratios: The branching ratios for semileptonic decays of b- and c-quarks are known to within 10% [44]. Therefore a systematic uncertainty of 10% in the $t\bar{t}$ acceptance due to heavy-quark branching ratios is assumed.
5. B decay modeling: ISAJET+QQ+QFL is used to model the $t\bar{t}$ acceptance, where QQ is used to fragment the b-quark. The acceptance for m_{top} = 120 GeV/c^2 has also been determined by allowing ISAJET to fragment the b-quarks. (i.e., no QQ.) The b- and c-quark semileptonic branching ratios used by ISAJET are the same as used by QQ. The difference in acceptance between

the ISAJET and QQ modeling of the b decay was found to be ~10%.

Table 7.7 summarizes the systematic uncertainties in the $t\bar{t}$ acceptance. The systematic uncertainty in $t\bar{t}$ events is taken to be 23%.

Table 7.2

Fraction of $b\bar{b}$ and QCD events in the W region. Errors are statistical only. Jets are defined as calorimeter clusters in a cone of $\Delta R = 0.4$ and $|\eta_{det}| < 2.0$. All E_T's have been corrected. '+' implies more jets may be present.

Jet Requirement	f_{BG} (%)
20+	21.1 ± 1.1
30+	21.7 ± 1.4
20,20+	18.3 ± 1.8
30,30+	23.0 ± 3.8
20,20,20+	20.5 ± 4.4
30,25,25+	19.7 ± 6.7

Table 7.3

R_{tag} for various jet requirements. Errors are statistical only. The jet requirements are exclusive; only one and two jet events with the minimum jet E_T's listed are used.

Jet Requirement	R_{tag} (%)
20	0.11 ± 0.07
20,20	1.09 ± 0.74
25,25	1.04 ± 1.00

Table 7.4

Expected number of background events in the 1992-3 collider run.

Process	Expected rate
Drell–Yan	0.06 ± 0.06
$b\bar{b}$	0.05 ± 0.04
Di-Boson	0.11 ± 0.03
$Z \rightarrow \tau\tau$	0.02 ± 0.01
$W + c$	0.03 ± 0.01
W+jets	1.54 ± 0.15
Total	1.80 ± 0.17

Table 7.5

Expected number of top events in the 1992-3 collider run. Uncertainties are those calculated in section 7.2.1

m_t=100 GeV	m_t=120 GeV	m_t=140 GeV	m_t=160 GeV	m_t=180 GeV
4.37 ± 1.02	4.35 ± 1.02	2.88 ± 0.67	1.52 ± 0.36	1.04 ± 0.24

Table 7.6

Change in $t\bar{t}$ acceptance due to jet energy variations.

Jet E_T scale variation (%)	Acceptance change (%) as a function of top mass (GeV)				
	m_{top}=100	m_{top}=120	m_{top}=140	m_{top}=160	m_{top}=180
+10	+40	+24	+20	+11	+10
-10	-22	-17	-16	-10	-7

Table 7.7

Systematic uncertainties on the top acceptance. All uncertainties are added in quadrature.

Source		Comments
High P_T lepton effici.	5%	
Soft μ effici.	2.5%	5%, but soft μ contributes ~1/2 to acc.
CES–CPR–dE/dx effici.	2.5%	5%, but soft e contributes ~1/2 to acc.
Had/EM for soft e	5%	10%, but soft e contributes ~1/2 to acc.
Gluon radiation	7%	half difference between off and on
Energy scale	15%	average variation from 120-180 GeV/c^2
b and c-quark BR	10%	
B fragmentation	10%	
Luminosity	3.5%	
Total	23%	

8. RESULTS

This chapter reviews the cuts devised in previous chapters used to tag $t\bar{t}$ events. The results of applying these cuts to the inclusive electron and muon data sets are given. The probability for the expected background fluctuating up to the number of events seen in the data is calculated.

8.1 Cuts Applied to Data

The inclusive electron and muon data sets were searched for events that passed the top cuts listed below:

1. All electron and muon detectors flagged as good. (BADRUN returns 15 for a given run.)
2. $|Z_{vertex}| < 60$ cm.
3. Event has at least one lepton passing all the cuts listed in chapter 3.
4. Border Energy less than 2 GeV for the high E_T lepton.
5. Event is not flagged as $Z \rightarrow ll$.
6. Events with high E_T primary electrons must pass the level 2 CEM9* or CEM_9* trigger.
7. Events with high P_T CMU and CMU·CMP muons must pass the level 2 CMU_CMP_CFT_9_2*, CMUNP_CFT_9_2*, CMUP_CFT_9_2*, or CMUP_CFT_6* trigger. High P_T CMX muons must pass the level 2 CMX_CFT_9_2_ET, CMX_CFT_9_2_ET_V1, CMX_CFT_9_2_ET_V2, CMX_CFT_9_2_ET_V3, CMX_CFT_9_2_V5 or CMX_CFT_9_2_ET_V4 trigger [23].

8. $\not\!\!E_T > 20$ GeV.
9. At least three jets with $|\eta_{det}| < 2.0$ with E_T greater than 30, 25, 25 GeV for the first, second and third highest E_T jet.
10. $\sum E_T > 250$ GeV.
11. Event has at least one soft lepton tag.
12. SLT is not tagged as a Drell-Yan or sequential *b*-decay. (See section 5.5.)

(BADRUN is a routine that reports problems with electron and muon detectors in any given run. A return value of 15 indicates that there were no problems with any detector during a particular run.)

24 events pass without a SLT tag, 7 with. Figure 8.1 plots the expected number of events as a function of top mass. The errors are those derived in chapter 7. The error bars on the "TOP + B.G." points are the systematic uncertainties on the top and background rates added in quadrature. (The theoretical uncertainty on the NLO $t\bar{t}$ cross section is not included.) Listed in table 8.1 are the run and event numbers for the events that pass all the cuts enumerated above. Figures 8.2 and 8.3 show a CTC and calorimeter display for top candidate 45879/123158.

8.1.1 Level 2 Trigger Effects

The level 2 electron and muon triggers are required in the real data so as to allow it to be normalized to MC data. (This is also why BADRUN must not report any problems; all components in QFL work, therefore all components in the data must as well.) If no trigger requirement is made, two additional μ+jets events pass. They are 45178/382599 and 46818/221912. 45178/382599 has a $P_T = 2.563$ GeV/c soft electron, and passes the level 2 PEM_20 and TAU_10_2JETS_SUMET_65_V2 triggers. 45178/382599 has a $P_T = 10.39$ GeV/c CMP muon, and passes the level 2 MET_35_TEX_2_NOT_FWD and MET_35_NOT_GAS triggers.

8.1.2 Analysis Repeated with a Higher $\sum E_T$ Cut

This analysis was repeated with the $\sum E_T$ cut raised to 300 GeV. The expected background is now 1.34 ± 0.13 events. 5 data events pass. Figure 8.4 plots the expected number of events as a function of top mass with this higher $\sum E_T$ cut.

8.1.3 Effect of Min-Bias Events on $\sum E_T$

The variable $\sum E_T$ was derived without accounting for the possibility that minimum bias interactions can occur in the same crossing. A typical min–bias event deposits roughly 10–40 GeV in the calorimeter. The seven final candidate events were scanned for evidence of min–bias interactions in addition to the primary interaction. Event 42517/44047 has $\sum E_T = 255.99$ GeV. This event is very clean with no evidence of additional vertexes. Event 43351/53868 has $\sum E_T = 297.41$ GeV, and contains a distinct min–bias interaction. The sum of all track P_T originating from the min–bias vertex is 12.4 GeV/c, which is rather small. It is not likely that this min–bias event would have a $\sum E_T > 47.41$ GeV, so this event is kept. The other five events have high enough $\sum E_T$ that they would safely pass the $\sum E_T > 250$ GeV cut even after subtracting E_T for a beefy min–bias interaction.

8.1.4 Significance of Results

The probability of $n_{BG}{}^{+\alpha}_{-\beta}$ fluctuating up to n_{Sig} events is given by poisson statistics where the mean, n_{BG}, is smeared by two gaussians with the positive gaussian having a sigma of α and the negative gaussian having a sigma of β. Therefore, the probability for a background of 1.80 ± 0.17 events fluctuating to ≥ 7 events is 0.29%. Likewise, the probability for a background of 1.34 ± 0.13 events fluctuating to ≥ 5 events is 1.25%. In terms of standard deviations, the significance is 2.76σ (2.24σ) for the $\sum E_T > 250(300)$ GeV cut.

Table 8.1

Events passing all top cuts.

Run/Event	Type	Tag Info. (GeV/c)	$\sum E_T$ (GeV)
45705/54765	e+3 jets	$P_T^e = 11.2$	380.85
45880/31838	e+4 jets	$P_T^e = 2.6$	388.72
42517/44047	μ+3 jets	$P_T^e = 4.2$	255.99
43351/53868	μ+3 jets	$P_T^{CMP\,\mu} = 19.4$	297.41
43351/266423	μ+3 jets	$P_T^{CMU\,\mu} = 2.1$	452.23
45047/104393	μ+3 jets	$P_T^e = 22.6$	320.21
45879/123158	μ+4 jets	$P_T^{CMU\cdot CMP\,\mu} = 13.5$	367.65

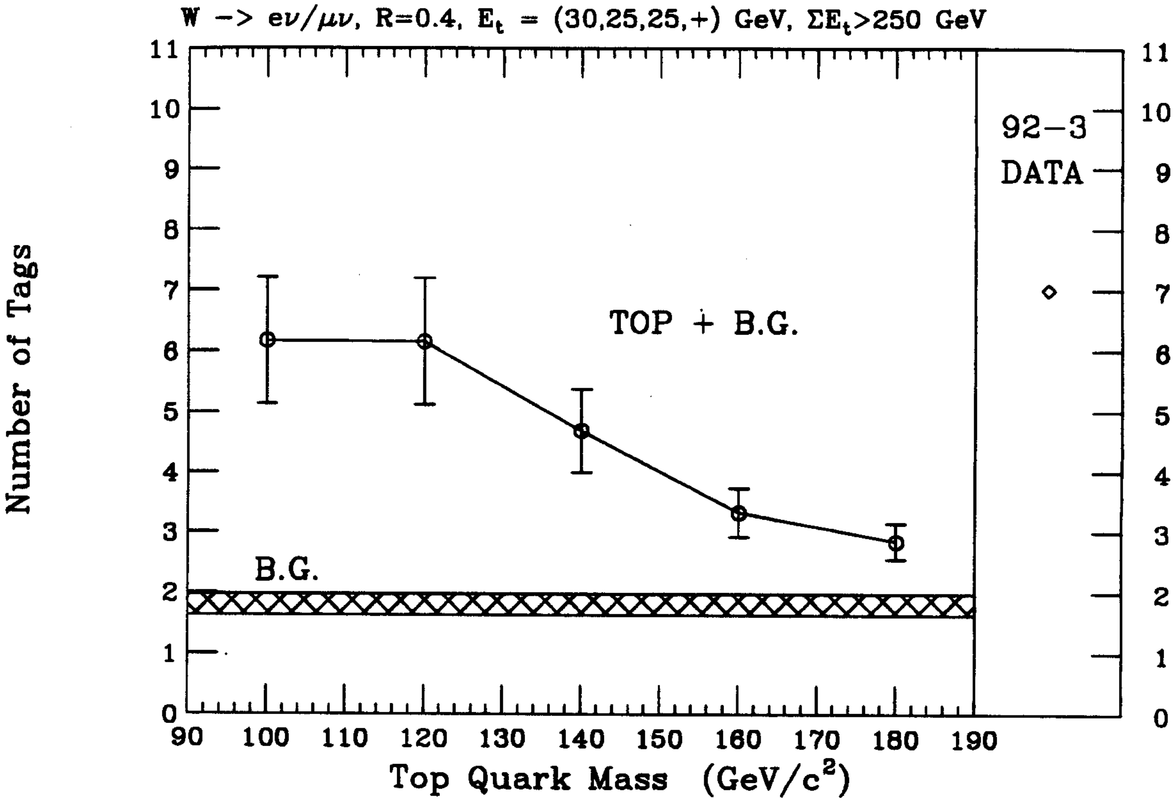

Figure 8.1

Expected number of tagged events as a function of top mass. The actual number of tags is shown as well. Errors are those derived in chapter 7. All events have $\sum E_T > 250$ GeV.

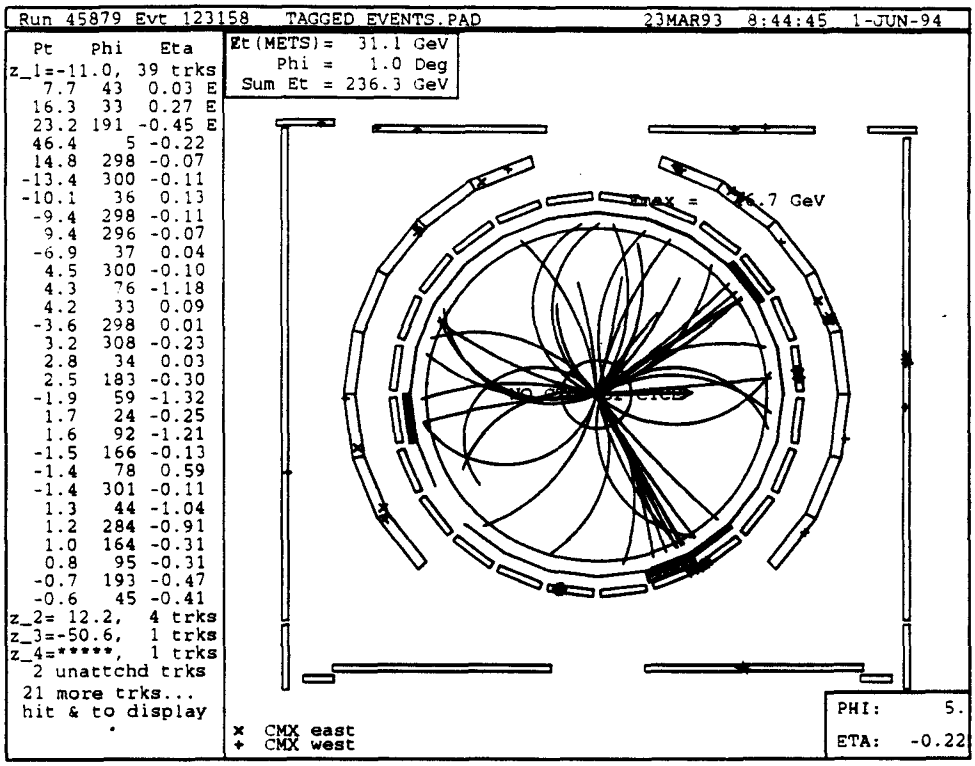

```
Run 45879 Evt 123158    TAGGED EVENTS.PAD               23MAR93   8:44:45   1-JUN-94
  Pt    Phi    Eta
z_1=-11.0, 39 trks
  7.7    43   0.03 E
 16.3    33   0.27 E
 23.2   191  -0.45 E
 46.4     5  -0.22
 14.8   298  -0.07
-13.4   300  -0.11
-10.1    36   0.13
 -9.4   298  -0.11
  9.4   296  -0.07
 -6.9    37   0.04
  4.5   300  -0.10
  4.3    76  -1.18
  4.2    33   0.09
 -3.6   298   0.01
  3.2   308  -0.23
  2.8    34   0.03
  2.5   183  -0.30
 -1.9    59  -1.32
  1.7    24  -0.25
  1.6    92  -1.21
 -1.5   166  -0.13
 -1.4    78   0.59
 -1.4   301  -0.11
  1.3    44  -1.04
  1.2   284  -0.91
  1.0   164  -0.31
  0.8    95  -0.31
 -0.7   193  -0.47
 -0.6    45  -0.41
z_2= 12.2,  4 trks
z_3=-50.6,  1 trks
z_4=*****,  1 trks
 2 unattchd trks
 21 more trks...
 hit & to display
```

```
Et(METS)=   31.1 GeV
    Phi =    1.0 Deg
 Sum Et = 236.3 GeV
```

```
× CMX east
+ CMX west
```

```
PHI:      5.
ETA:   -0.22
```

Figure 8.2

A CTC display for top candidate 45879/123158

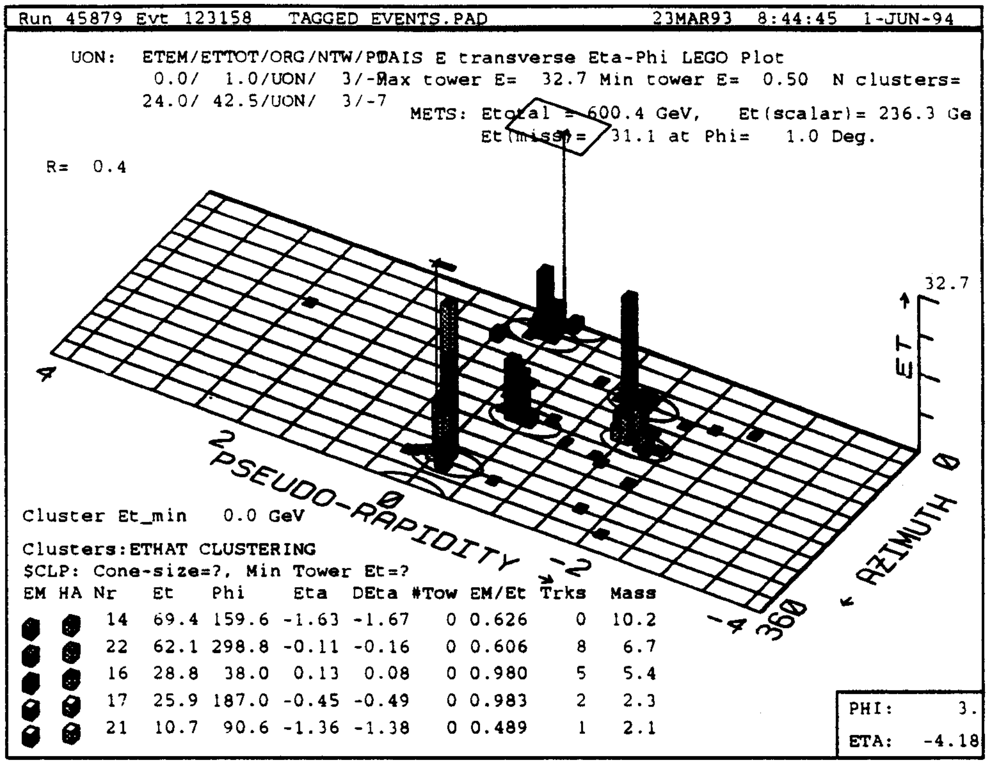

```
Run 45879 Evt 123158    TAGGED EVENTS.PAD                23MAR93   8:44:45   1-JUN-94
     UON:   ETEM/ETTOT/ORG/NTW/PDAIS E transverse Eta-Phi LEGO Plot
             0.0/  1.0/UON/  3/-Max tower E=  32.7 Min tower E=  0.50  N clusters=
            24.0/ 42.5/UON/  3/-7
                                  METS: Etotal = 600.4 GeV,    Et(scalar)= 236.3 Ge
                                             Et(miss)=  31.1 at Phi=   1.0 Deg.
   R=  0.4

 Cluster Et_min    0.0 GeV

 Clusters:ETHAT CLUSTERING
 $CLP: Cone-size=?, Min Tower Et=?
 EM HA Nr   Et    Phi     Eta   DEta #Tow EM/Et Trks  Mass
 ●  ●   14  69.4 159.6 -1.63 -1.67    0 0.626    0  10.2
 ●  ●   22  62.1 298.8 -0.11 -0.16    0 0.606    8   6.7
 ●  ●   16  28.8  38.0  0.13  0.08    0 0.980    5   5.4
 ●  ●   17  25.9 187.0 -0.45 -0.49    0 0.983    2   2.3
 ●  ●   21  10.7  90.6 -1.36 -1.38    0 0.489    1   2.1

                                                              PHI:       3.
                                                              ETA:   -4.18
```

Figure 8.3

A calorimeter display for top candidate 45879/123158

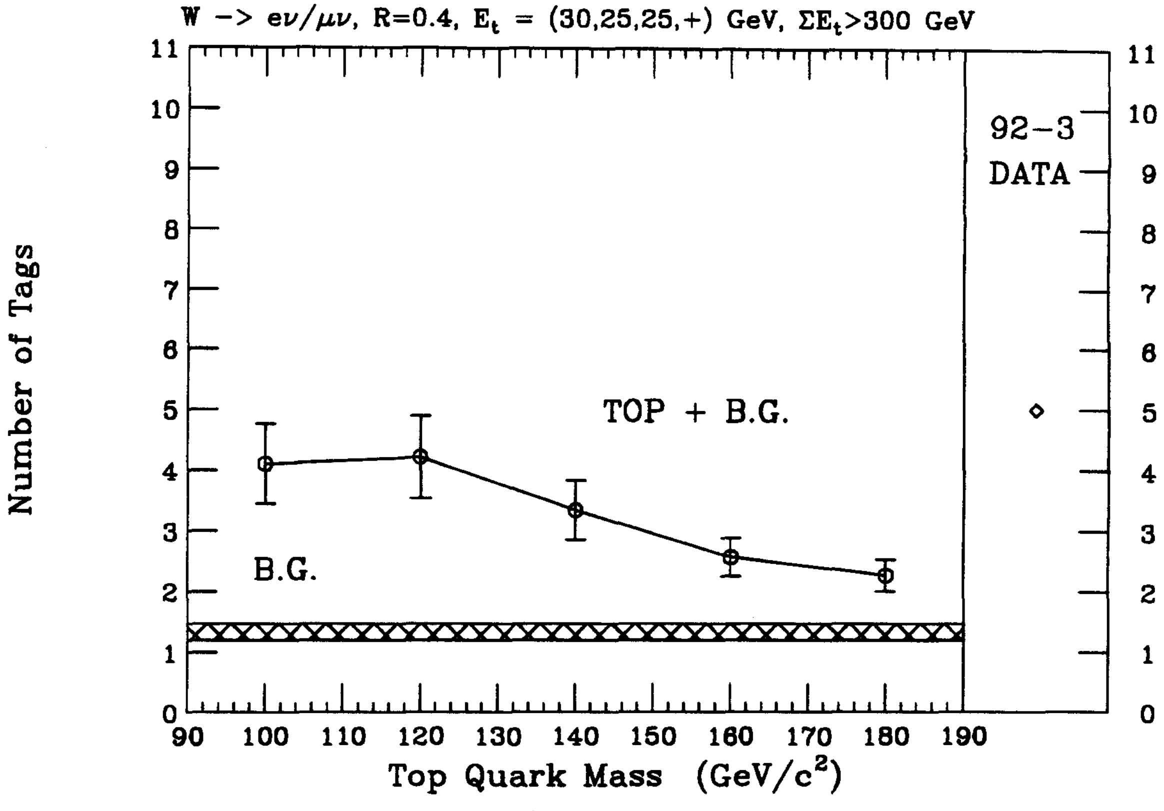

Figure 8.4

Expected number of tagged events as a function of top mass. The actual number of tags is shown as well. Errors are those derived in chapter 7. All events have $\sum E_T > 300$ GeV.

9. CONCLUSION

This thesis was devoted to searching for the top quark in the lepton plus jets channel as shown below below:

$$p\bar{p} \rightarrow t\bar{t} \rightarrow e\nu_e bq\bar{q}\bar{b} \tag{9.1}$$

$$p\bar{p} \rightarrow t\bar{t} \rightarrow \mu\nu_\mu bq\bar{q}\bar{b} \tag{9.2}$$

Candidate events were selected by requiring the presence of at least one isolated high P_T lepton, large missing E_T, ≥ 3 high E_T jets, and a significant $\sum E_T$. To further reduce background processes in the final event sample, at least one non-isolated lepton was required to act as a tag for the b-quarks.

Estimates of the W+jet, $b\bar{b}$ and QCD, Drell–Yan, di–boson, $W + c$, and $Z \rightarrow \tau\tau$ background rates in 19.3 pb^{-1} of data collected during the 1992–3 collider run were made. The expected number of $t\bar{t}$ events as a function of top mass was also calculated. Systematic uncertainties for the above processes were computed as well.

On the order of 10^{12} collisions occurred during the 1992–3 collider run. Out of this, 7(5) events passed all cuts with $\sum E_T > 250(300)$ GeV. 1.80±0.17(1.34±0.13) events due to background processes were expected. The probability for the background fluctuating up to 7(5) events is 0.29(1.25)%. Though this is not clear evidence for top, the natural interpretation for this excess is $t\bar{t}$ production. Assuming the excess events are from top, the $t\bar{t}$ cross section can be calculated using the following formula:

$$\sigma(t\bar{t}) = \frac{n^{Sig} - n^{BG}}{\epsilon \int \mathcal{L} dt}, \tag{9.3}$$

where $\sigma(t\bar{t})$ is the top cross section, n^{Sig} is the number of events that pass all cuts, n^{BG} is the expected number of background events, ϵ is the $t\bar{t}$ efficiency (which is dependent on m_{top}), and $\int \mathcal{L}dt$ is the integrated luminosity. All these quantities are known except ϵ, since it dependant on the top mass. Table 9.1 lists the top acceptance, including fake tags—after all cuts in chapter 8 have been applied—as a function of top mass. There is no a priori way to estimate m_{top} (or ϵ) from this analysis. However, CDF has published a top quark mass estimate of $174 \pm 10^{+13}_{-12}$ GeV/c^2 derived through kinematic reconstruction and under the assumption that the excess yield seen in several analyses is the result of $t\bar{t}$ production [45]. (This result is consistent with $m_{top} = 174^{+11+17}_{-12-19}$ GeV/c^2 derived from global fits to electroweak measurements [6].) Taking m_{top} to be in the range determined by CDF, ϵ is taken to be $1.55 \pm 0.36^{+0.33}_{-0.28}\%$, where the first uncertainty is due to the uncertainty on the top acceptance (section 7.2.1), and the second is due to the uncertainty on top mass. Taking all this together, the top cross section is estimated to be $17.4^{+5.5}_{-5.2}$ pb. This is rather high since the theoretical cross section for a top with $m_{top} = 174$ GeV/c^2 is ~ 5.1 pb. However, owing to the low statistics, such a result is not surprising.

The CDF top analysis [45] reported the results of three different top searches: soft lepton tagging (a variant of this SLT analysis), SVX (using the SVX to tag b-decays), and a search using opposite sign dileptons (DIL) to tag $t\bar{t} \rightarrow l^+\nu_l b l^- \bar{\nu}_l \bar{b}$ events. This article calculated the probability, $\mathcal{P}_{combined} = 0.26\%$, that all three results combined were due only to an upward fluctuation of the background to greater than or equal to the total number of tags seen. This analysis can be naively repeated by substituting the results from the SLT search described in this thesis for the results reported by CDF.

The dilepton analysis found 2 events with an expected background of $0.56^{+0.25}_{-0.13}$. The SVX analysis tagged 6 events with an expected background of 2.3 ± 0.3. The

SLT analysis performed in this thesis found 7 events with an expected background of 1.80 ± 0.17. Of the 7 events found by the SLT analysis, 3 are tagged in the SVX analysis. The DIL analysis shares no events with the SLT or SVX. If the SLT, SVX, and DIL analyses were uncorrelated, which they are not, the total background would be the sum of all three analyses or $4.66^{+0.43}_{-0.37}$ events, and the number of tags would be 15. One conservative method to eliminate correlations between analyses is to ignore overlapping events, and to scale down the expected background rate accordingly. The tags to dismiss are the three SVX tags in events that are also tagged in the SLT analysis. The estimated SLT background remains the same, and all 7 SLT events are kept. The number of SVX events is reduced to $6 - 3 = 3$, and the expected SVX BG reduces to $\frac{3}{6} \times (2.3 \pm 0.3) = 1.15 \pm 0.15$. The combined BG rate is $(1.80 \pm 0.17) + (1.15 \pm 0.15) + (0.56^{+0.25}_{-0.13}) = 3.51^{+0.34}_{-0.26}$, with 12 tags. This signal and expected background rate produces $\mathcal{P}_{combined} = 0.040\%$. This corresponds to a 3.37σ excess for a gaussian probability function.

Though this analysis did not find clear evidence for $t\bar{t}$ production, the results are quite tantalizing. As this thesis is being written, CDF is in the process of collecting an estimated 75 pb^{-1} of additional $p\bar{p}$ collision data. If the top exists, it will yield to discovery in the following months.

Table 9.1

Top tagging efficiency as a function of m_{top} for $\sum E_T = 250$ GeV. The error quoted is the 23% systematic uncertainty derived in section 7.2.1.

Top Mass (GeV/c^2)	Top acceptance (%)
100	0.29 ± 0.07
120	0.74 ± 0.17
140	1.14 ± 0.26
160	1.28 ± 0.30
180	1.67 ± 0.39

BIBLIOGRAPHY

BIBLIOGRAPHY

1. J. Marriner S. Belforte, P. Derwent and C. Grosso-Pilcher. σ_{BBC} Updates. CDF/PHYS/CDF/CDFR/2535, April 1994.

2. H. Sagawa et al. Measurement of $e^+e^- \rightarrow b\bar{b}$ Forward-Backward Assymetry between $\sqrt{s}$=52 and 57 GeV. *Physical Review Letters*, 63(21), November 1989.

3. A. Boras and J.M. Gerard. *Physics Letters B*, 203, 1988.

4. F. Abe et al. (The CDF Collaboration). Measurement of $\sigma \cdot B(W \rightarrow e\nu)$ and $\sigma \cdot B(Z^0 \rightarrow e^+e^-)$ in $p\bar{p}$ Collisions at $\sqrt{s} = 1800$ GeV. *Physical Review D*, 44(29), 1991.

5. J. Rosner. Electroweak Measurements and the Top Quark. EFI 92-19, May 1992.

6. B. Pietrzyk for the LEP collaborations and the LEP Electroweak Working Group; XXIXth Rencontres de Moriond, Méribel, Savoie, France, March 12-19, 1994.

7. F. Abe et al. (The CDF Collaboration). Fermilab Preprint Fermilab-Conf-93/210-E. 1993.

8. Gordon Kane. *Modern Elementary Particle Physics*, pages 208–9. Addison-Wesley, Redwood City, Ca, 1987.

9. W.J. Stirling A.D. Martin, R.G. Roberts. Benchmark cross sections for $p\bar{p}$ Collisions at 1.8 tev. *Z.Phys.*, C42(277), 1989.

10. V. Barger and R. J. N. Phillips. *Collider Physics*, pages 375,377. Frontiers in Physics Lecture Note Series. Addison-Wesley Publishing Co., 1987.

11. R. K. Ellis. The Theory of Heavy Flavor Production. FERMILAB-CONF-89/168-T, August 1989. pg. 6.

12. C. Peterson, D. Schlatter, I. Schmitt, and P. M. Zerwas. *Physical Review D*, 27:105, 1983.

13. V. Barger and R. J. N. Phillips. *Collider Physics*, page 179. Frontiers in Physics

Lecture Note Series. Addison-Wesley Publishing Co., 1987.

14. V. Barger and R. J. N. Phillips. *Collider Physics*, page 180. Frontiers in Physics Lecture Note Series. Addison-Wesley Publishing Co., 1987.

15. V. Barger and R. J. N. Phillips. *Collider Physics*, page 104. Frontiers in Physics Lecture Note Series. Addison-Wesley Publishing Co., 1987.

16. F. Abe et al. (The CDF Collaboration). *Physical Review Letters*, 68, 1992.

17. F. Bedeschi. Operation if the CDF Silicon Vertex Detector with Colliding Beams at Fermilab. FERMILAB-Conf-92/263-E, October 1992.

18. F. Abe et al. (The CDF Collaboration). *Physical Review Letters*, 62, 1989.

19. L. Balka et al. *Nuclear Instruments and Methods in Physics Research*, A267, 1988.

20. F. Abe et al. (The CDF Collaboration). Top Quark Search in the Electron + Jets Channel in Proton-Anti-Proton Collisions as $\sqrt{s} = 1.8$ TeV. CDF/PUB/HEAVYFLAVOR/PUBLIC/1188, July 1990.

21. S. E. Kopp et al. Preliminary Measurement of the Ratio $R = \sigma \cdot B(p\bar{p} \to W^{\pm} \to e^{\pm}\nu)/\sigma \cdot B(p\bar{p} \to Z^0 \to e^+e^-)$ in Proton-Antiproton Collisions at $\sqrt{s} = 1800$ GeV. CDF/ANAL/ELECTROWEAK/CDFR/1942, March 1993.

22. M. Vondracek. High Pt Muon Cut Efficiencies for 1992-3 Run. CDF/DOC/MUON/CDFR/2033, July 1993.

23. P. Schlabach. Searching for Top Decay to Muon + Jets in CMX. CDF/DOC/TOP/CDFR/2169, August 1993.

24. A. Galtieri. Search for the Top Quark in Electron-Muon Events with CDF. CDF/DOC/HEAVYFLAVOR/PUBLIC/1134, September 1990.

25. F. Paige and S. D. Protopopescu. Bnl Report No. 38034, 1986.

26. G. Trahern P. Avery, K. Read. Cornell Internal Note CSN-212. Unpublished, March 1985.

27. N. Isgur et al. Semileptonic B and D decays in the quark model. *Physical Review D*, 39(3), 1989.

28. J. Ohnemus and J.F. Owens. *Physical Review D*, 43, 1991.

29. H.Kuijf F.A. Berends, W.T. Giele and B. Tausk. *Nucl. Phys.*, B357, 1991.

30. F. A. Berends et al. On the production of a W and jets at hadron colliders. FERMILAB-Pub-90/213-T, October 1990.

31. J. Benlloch, A. Caner, and T. Rodrigo. A Measurement of the W Cross Section as a Ffunction of the Jet Multiplicity in W → $l\nu$ Events. CDF/PHYS/CDFR/1873, October 1992.

32. Talk presented by D. Gerdes in April 1992.

33. C. Campagnari, B. Farhat, P. Sphicas, and A. Yagil. Update on the search for the top in the lepton + jets channel with a lepton tag, Volume 3. CDF/ANAL/TOP/CDFR/2245, October 1993.

34. H. Frish A. Byon, S. Eno and R. Snider. The W and Z Underlying Event Analysis. CDF/ANAL/ELECTROWEAK/CDFR/1416, April 1991.

35. G. Marchesini and B.R. Webber. *Nucl. Phys.*, B310, 1988.

36. C. Campagnari, B. Farhat, P. Sphicas, and A. Yagil. Muon identification in the lepton + jets + muon tag analysis. CDF/ANAL/TOP/CDFR/2098, July 1993.

37. C. Campagnari, B. Farhat, P. Sphicas, and A. Yagil. Low P_T Electron Identification. CDF/ANAL/TOP/CDFR/2161, July 1993.

38. Talk presented by C. Campagnari in Oct 1993.

39. A. Caner, A. Mukherjee, and A. Yagil. Tracking eefficiency for Soft Lepton Tagging. CDF/ANAL/TOP/CDFR/2363, December 1993.

40. N. Shaw R. Hughes, P.Koehn et al. Non-W Backgrounds in W Plus Jets. CDF/ANAL/HEAVYFLAVOR/CDFR/2027, April 1993.

41. H.H. Williams N.M. Shaw, G. Unal. Update on Backgrounds to Top Searches Using SVX b-Tagging. CDF/ANAL/TOP/CDFR/2206, September 1993.

42. U. Baur et al. *Phys. Lett.*, B318, 1993.

43. M.L. Mangano. *Nucl. Phys.*, B405, 1993.

44. Opal collaboration. CERN-PPE-93-106.

45. F. Abe et al. (The CDF Collaboration). Evidence for Top Quark Production in $p\bar{p}$ Collisions at $\sqrt{s} = 1.8$ tev. FERMILAB-Pub-94/097-E (submitted to PRD), April 1994.

VITA

VITA

James Ian Tonnison [redacted] He attended school in [redacted]. He then went to college for two years at the University of Pittsburgh. He then finished his Bachelors degree at Rutgers College in New Brunswick, New Jersey in 1987. In 1987 he went to graduate school at Purdue University in West Lafayette, Indiana, and earned a Masters Degree in 1989. Next he joined the CDF collaboration at Fermilab National Accelerator Laboratory in Batavia, Illinois as Virgil Barnes' graduate student. He graduated from Purdue in July, 1994 with a Ph.D.